THE UNIVERSITY OF CHICAGO

TWO-DIMENSIONAL SEMICONDUCTORS FOR CHIRAL NANOPHOTONICS

A DISSERTATION SUBMITTED TO
THE FACULTY OF THE DIVISION OF THE PHYSICAL SCIENCES
IN CANDIDACY FOR THE DEGREE OF
DOCTOR OF PHILOSOPHY

DEPARTMENT OF PHYSICS

BY
ROBERT TODD SHREINER

CHICAGO, ILLINOIS
JUNE 2023

To my family and friends,

especially my parents and Alanna,

for their company and care.

TABLE OF CONTENTS

LIST OF FIGURES

LIST OF TABLES

ACKNOWLEDGMENTS

I am deeply indebted to the excellent researchers, teachers, and friends who have animated my years here. Without their support, this dissertation would not have been possible.

My advisor, Alex High, has been a constant source of encouragement. From my earliest time in the group, his unflinching optimism, reliable reassurance, and sure vision have guided my work. I have appreciated his thoughtful insights into the scientific craft and have greatly enjoyed our conversations about life inside and out of the lab. The group's flourishing is a testament to his leadership, which has prioritized a welcoming environment for rigorous, collaborative study. I am as excited today about the lab's future as I was when we first chatted nearly six years ago in Alex's then newly minted office.

I am thankful for the considerate advice from my committee members: David Schuster, Michael Levin, and David Schmitz. Beyond their committee roles, they have served also as knowledgeable instructors and inspiring researchers.

I want to express my earnest appreciation for all of my colleagues in the High Lab. I am continually impressed by their hard work and dedication – not only to their own projects, but to assisting each other also. Lab work can get tedious and solitary, but never for too long here, with so many friendly lab mates, generous with their time and ideas.

I want to acknowledge a few people in particular: Kai Hao and Andrew Kindseth, who have worked closely with me on the results presented in this dissertation, and Amy Butcher and Xinghan Guo, who have journeyed with me since the beginning. Kai has been an incredible mentor, his fruitful creativity, calm patience, and dependable cheerfulness abiding supports over the years. I will miss our trips for lunch and coffee. Andrew has joined the team more recently with an unmatched enthusiasm. I am hopeful he can tie up my loose ends and push our efforts in exciting new directions. Amy and Xinghan are my fellow founding students. I carry fond memories of our early days building everything from scratch, and their companionship and help throughout have been gifts.

The University of Chicago is renowned for its collaborative research community, and I have benefited from the assistance of many individuals across campus. The fine people of the Pritzker Nanofabrication Facility, led by the indomitable Peter Duda, have been unsparing in their support and guidance. Justin Jureller runs a tight ship at the Materials Research Center, and his scrupulous training and maintenance have been appreciated. I am thankful to Kan-Heng Lee for his kindly instruction in the cleanroom. Bracing discussions with Jiwoong Park, Alan Dibos, and Peter Littlewood have strengthened the following results.

Lastly, I must acknowledge my friends and family for their love and support. My parents have always encouraged me in my academic pursuits, for which I am sincerely grateful. Moreover, their charitable diligence and attentive care for others and each other have remained heartening examples. I have found many dear buddies here, beginning with Mike van der Naald at visitation weekend, who have graced my days with loud laughs and good cheer. Alanna has been a steadfast partner, ever ready to offer comfort and to share in celebration.

Thank you all!

ABSTRACT

The interplay of light and matter at the nanoscale has spurred recent advancements across a broad swath of diverse disciplines, from biosensing and energy harvesting to quantum information science and optical engineering. Confined to these small length scales – somewhere between the extent of a few atoms and the wavelength of visible light – materials and photons begin to look strikingly different than in their "bulk" counterparts. This dissertation builds on and bridges the promising research on two such systems: atomically thin semiconductors and chiral nanophotonics. Two-dimensional transition metal dichalcogenides – van der Waals semiconductors only three atoms thick – host tightly bound, optically bright excitons and strongly interacting electrons with spin and valley degrees of freedom addressable via circularly polarized light. Chiral nanophotonics exhibit guided modes with circularly polarized evanescent waves, wherein the electric field ellipticity is strictly locked to the propagation direction. Leveraging these properties, an integrated TMDC-nanophotonic interface is demonstrated for on-chip, active routing of excitonic emission into a waveguide. Additionally, long-range spin polarization of itinerant electrons, which arises from interaction-driven magnetic ordering, is generated by microwatt optical pumping. Together, these results establish a novel route for low-power, integrated non-reciprocal photonics and provide new tools for optoelectronic, valleytronic, and spintronic technologies.

PUBLICATIONS

The main findings of this dissertation have been reported in the following manuscripts:

- **Robert Shreiner**†, Kai Hao†, Amy Butcher, and Alexander A. High. Electrically controllable chirality in a nanophotonic interface with a two-dimensional semiconductor. *Nature Photonics* **16**, 330-336 (2022).
- Kai Hao†, **Robert Shreiner**†, Andrew Kindseth, and Alexander A. High. Optically controllable magnetism in atomically thin semiconductors. *Science Advances* **8**, eabq765 (2022).

Supporting results have been incorporated into the following manuscripts:

- Amy Butcher, Xinghan Guo, **Robert Shreiner**, Nazar Delegan, Kai Hao, Peter J. Duda III, David D. Awschalom, F. Joseph Heremans, and Alexander A. High. High-Q Nanophotonic Resonators on Diamond Membranes using Templated Atomic Layer Deposition of TiO_2. *Nano Letters* **20**(6), 4603-4609 (2020).
- Xinghan Guo, Nazar Delegan, Jonathan C. Karsch, Zixi Li, Tianle Liu, **Robert Shreiner**, Amy Butcher, David D. Awschalom, F. Joseph Heremans, and Alexander A. High. Tunable and Transferable Diamond Membranes for Integrated Quantum Technologies. *Nano Letters* **21**(24), 10392-10399 (2021).
- Andrew J. Mannix†, Andrew Ye†, Suk Hyun Sung, Ariana Ray, Fauzia Mujid, Chibeom Park, Myungjae Lee, Jong-Hoon Kang, **Robert Shreiner**, Alexander A. High, David A. Muller, Robert Hovden, and Jiwoong Park. Robotic four-dimensional pixel assembly of van der Waals solids. *Nature Nanotechnology* **17**, 361-366 (2022).

†. These authors contributed equally to this work.

CHAPTER 1

INTRODUCTION

Since the turn of the century, the photonics community has pioneered on-chip, light-based alternatives to today's widespread integrated electronic circuitry in an effort to meet the growing demands for faster, more efficient information processing. Particular attention has been given to device miniaturization, with the hope for compact architectures requiring only low power operation. Essential to this pursuit, tailoring the flow of light is achieved through the careful engineering of light-matter interactions at the nanoscale. However, as system sizes pass below the wavelength of light and approach the atomic limit, the properties of both light and matter begin to vary significantly, posing not only challenges to scalable implementation but also opportunities for novel device designs.

Two-dimensional semiconductors have emerged over the last decade as model optical materials for next-generation photonics. Atomically thin sheets, isolated transition metal dichalcogenide (TMDC) monolayers are optically active semiconductors with direct band gaps in the visible and near-infrared spectral domains. Due to reduced dielectric screening, quantum confinement, and large carrier masses, strong Coulomb interactions lead to the formation of tightly bound excitons, which show enhanced coupling to light compared to excitons in conventional semiconductors. TMDC monolayers also can be readily fabricated into heterostructure devices with little concern for growth chemistry or lattice matching and are highly tunable with electric, magnetic, and optical fields. Uniquely, the broken inversion symmetry of the monolayer crystal distinguishes the valley degree of freedom, which results in chiral optical selection rules (*i.e.*, left-handed and right-handed photons selectively address excitonic resonances in separate valleys).

In parallel, chiral optical interfaces have been developed based on plasmonic and nanophotonic waveguide structures, in which tightly confined light displays unusual circular polarization. Unlike the common picture of helical light where the electric field rotates about the

propagation axis, here the electric field tumbles along the propagation direction – the spokes of a bicycle wheel rather than the propeller blades of an airplane. Importantly, the field ellipticity is locked to the propagation direction and the off-axis position, an effect termed optical spin-orbit coupling.

When placed in proximity to these chiral interfaces, circular dipoles selectively interact with guided modes according to their propagation direction. To much success, the quantum optics community has utilized such techniques for unidirectional routing of single photons and non-reciprocal scattering off single emitters. From the perspective of integrated photonics, TMDC monolayers, due to their valley-dependent optical response, are appealing materials for realizing chiral optical interfaces. A handful of promising demonstrations have been reported in recent years. This thesis presents our efforts towards advancing TMDC-based chiral nanophotonics.

1.1 Outline

Chapter 2 introduces the extensive literature on TMDC monolayers, highlighting their electronic, optical, and spin/valley properties. Notably, the large Coulomb interaction between carriers enhances excitonic effects, which govern emission and absorption, and drives correlated phases, such as itinerant ferromagnetism.

Chapter 3 overviews the essential physics and formative studies of transverse spin in nanoscale optical structures. Although the classical theory of electromagnetism was laid down by Maxwell over a century and a half ago, the last few decades have brought new discoveries of exotic polarization properties of light, which form the basis of chiral nanophotonic interfaces.

Chapter 4 details the experimental techniques utilized for the fabrication and characterization of TMDC heterostructures and titania photonic structures. Inheriting the techniques for exfoliation and assembly of layered materials, high quality encapsulated TMDC mono-

layers are made with integrated gate control for electrostatic tuning of well resolved excitonic resonances. Smooth nanophotonic devices are created through conformal atomic layer deposition of high-index titania (TiO_2), a gentle technique developed for interfacing photonic structures with delicate substrates. The resulting TMDC and nanophotonic samples are studied with the help of confocal scanning microscopy.

Chapter 5 presents a new integrated chiral TMDC-photonic interface built from these platforms, which advances the current state-of-the-art. First, the interface chirality is electrically tunable, based on the doping-dependent exciton valley polarization, enabling active switching between directionally biased and balanced optical coupling of waveguide modes to the TMDC monolayer. This result opens entirely new photonic logic and control schemes that use 2D materials. Additionally, near-field excitation through the photonic waveguide generates directionally reconfigurable, valley(spin)-polarized exciton fluxes. This finding creates a new approach for utilizing integrated photonics to locally manipulate the valley and spin degrees of freedom of charge carriers in semiconductors. Lastly, the photonic fabrication method provides a general platform for on-demand patterning of photonic structures on 2D materials with no deleterious effects on material quality, which can have an immediate impact on interfacing scalable photonic devices with van der Waals heterostructures and wafer-scale monolayers.

Chapter 6 reports the discovery that optical pumps can both control and measure correlated magnetic phases of low-density electrons in a TMDC monolayer, even at zero applied magnetic field. With recent observations of Wigner crystals, magnetic phases, and fractional quantum Hall states, TMDC monolayers are rapidly emerging as a leading platform to explore correlated electron states. However, while these systems have been intensely studied, little is understood at the microscopic level about the dynamics of these states. Remarkably, here, a sub-micron, nanosecond pulse of spin excitation generates a wave of magnetic order that spreads across large sample areas, instigating a long-range breakdown

of symmetry between competing quantum phases. These findings will spur further studies of dynamic, local processes in other correlated systems, such as electrons in moiré potentials. Additionally, they demonstrate a new optical toolbox for manipulating correlated phases, which combines ultrafast control, diffraction-limited spatial resolution, and optical polarization. Furthermore, the capability to optically manipulate magnetic memory and generate spin amplification in TMDCs, which are widely studied for next-generation technologies, will push optoelectronics and spintronics in new directions.

Chapter 7 unifies these results in a proposal for a low-power, all-optical isolator. Integrated magnet-free isolator designs in which optical reciprocity is broken without applying a restrictive magnetic field have been identified as essential elements for future photonic circuitry. TMDC monolayers are optically controllable magnetic materials exhibiting large circular dichroism (Chapter 6), which can be directionally coupled to the modes of chiral nanophotonic waveguides (Chapter 5). By simulating the non-reciprocal index contrast of forward and backward propagating cavity modes of a ring resonator structure interfaced with a TMDC monolayer, isolation exceeding 10 dB is predicted. Importantly, integrated optical driving of the non-reciprocity operates at low power – preliminary measurements suggest near the microwatt regime – orders of magnitude below that of leading alternatives.

Chapter 8 concludes with a brief perspective on future directions.

CHAPTER 2

ATOMICALLY THIN SEMICONDUCTORS

2.1 From bulk to monolayer TMDCs

Transition metal dichalcogenides (TMDCs) are a family of layered materials of the form MX_2, where M is an element of the group IV, V, or VI transition metals and X is a chalcogen. Crystalline sheets piled weakly by van der Waals forces, TMDCs have long been utilized for their unique mechanical properties as lubricants [1, 2]. However, although chemically and structurally similar, TMDCs – from insulating HfS_2 to metallic VSe_2 – display a variety of optical and electronic properties, which has sustained their study for over half a century [3, 4]. This work focuses on the sub-class of semiconducting transition metal dichalcogenides, including MoS_2, $MoSe_2$, WS_2, and WSe_2 [5].

The crystal structure of bulk TMDCs is defined by the intralayer atomic lattice and the interlayer registry. A single layer is only three atoms thick, consisting of an X–M–X "sandwich of 'anion' and 'cation' sheets" [3]. As illustrated in Figures 2.1a and 2.1b, the bonding geometry of a central metal atom to its six outer chalcogen atoms can be trigonal prismatic or octohedral, respectively [6]. The electron coordination of the chalcogen atoms is skewed towards in-plane covalent bonding with the metal atoms, leaving lone pairs of electrons on the outer surface (Fig. 2.1c). These lone-pairs interact with those of neighboring layers through van der Waals forces – *i.e.*, the sum of dipole and induced dipole interactions, attractive and repulsive, which do not lead to bond formation [7]. The weak out-of-plane forces allow easy cleaving, giving bulk crystals their characteristic flaky appearance (Fig. 2.1d).

Common polymorphs of TMDCs are shown in Figure 2.2. For the semiconducting TMDCs MoS_2, $MoSe_2$, WS_2, and WSe_2, the $2H_c$ phase is typical, although the 3R phase is also stable [9]. The $2H_c$ structure exhibits a stacking sequence of CaC AcA – *i.e.,* the

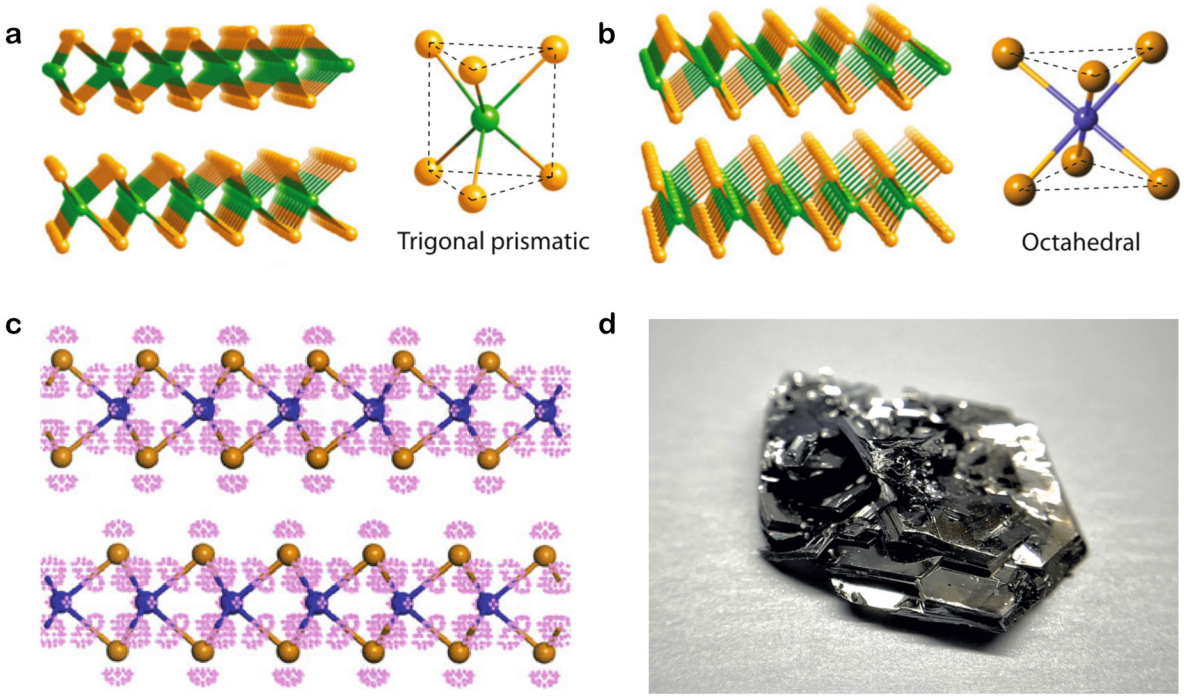

Figure 2.1: Bulk TMDC crystals. a, b, Representative schematics of a layered transition metal dichalcogenide crystal. Metal atoms, such as molybdenum (Mo) and tungsten (W), are colored green, and chalcogen atoms, such as sulpher (S) and selenium (Se), are colored orange. In the trigonal prismatic structure (**a**), the chalcogen atoms are aligned, while in the octahedral structure (**b**), they are staggered. **c**, The layers are held together by strong, in-plane covalent bonding and weak, out-of-plane van der Waals bonding, as shown in the charge density redistribution (pink) simulated by density functional theory. **d**, Bulk TMDC flakes – here grown and imaged by 2D Semiconductors – appear metallic and typically span a few millimeters in length. Figure adapted from source: **a, b, c** – [8].

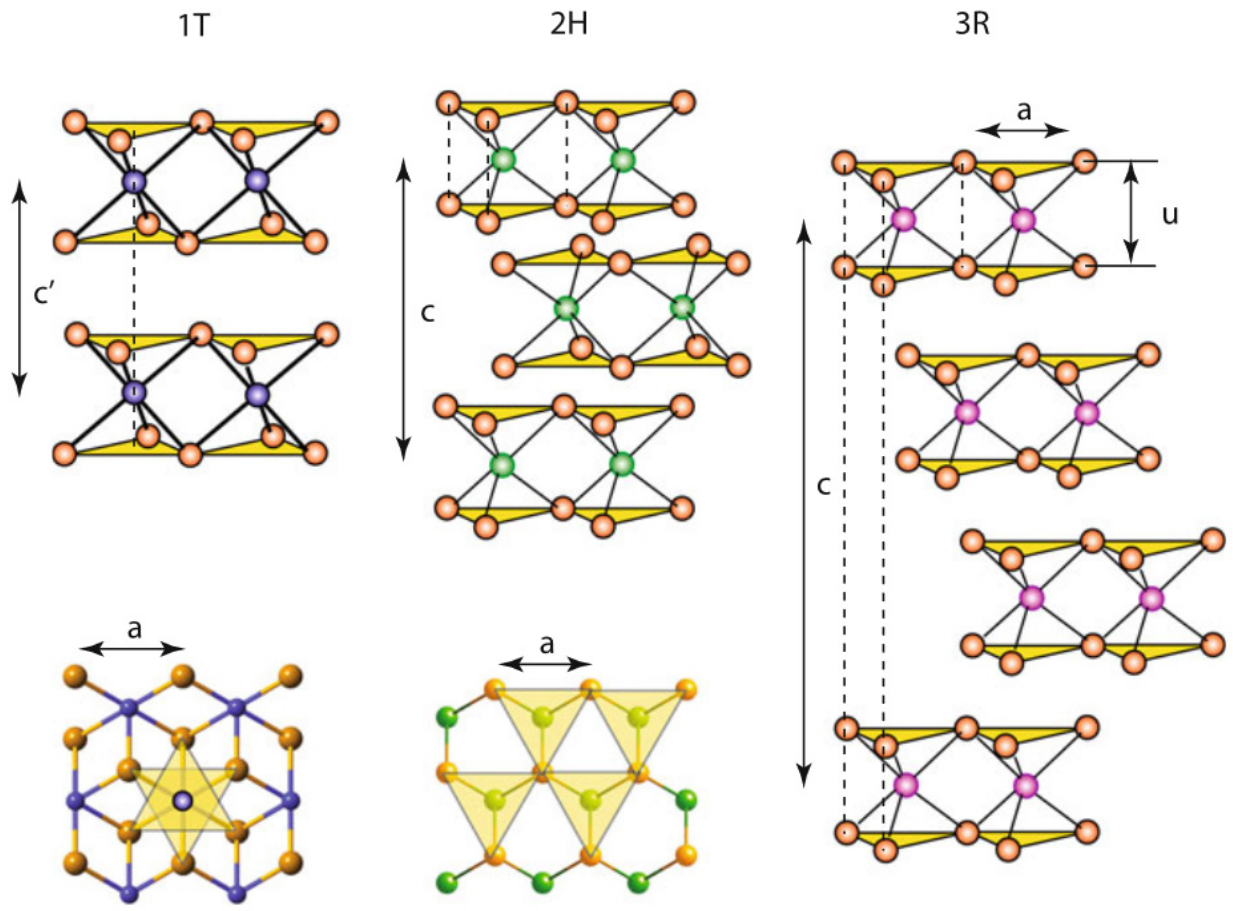

Figure 2.2: Structural polytypes. Structural polytypes display different symmetries (*i.e.*, T – tetragonal, H – hexagonal, and R – rhombohedral), intralayer/interlayer coordinations, and stacking orders. The bulk material from which TMDC monolayers are exfoliated in this work is of the 2H polytype. Figure adapted from source [8].

M atom (lower case letters) in one layer is vertically aligned with the two X atoms (upper case letters) in the neighboring layers. Crystals with odd numbers of layers, including single monolayers (Fig. 2.3a), belong to the D^1_{3h} hexagonal symmorphic space group. Crystals with even numbers of layers belong to the D^3_{3d} symmorphic space group. Notably, the even-layered polytypes display inversion symmetry through the central horizontal plane, while the odd-layered polytypes show only reflection symmetry [10].

Although few-layered thin films of TMDCs had been studied for decades prior [11–13], single monolayers were first reported only in 2010 [14, 15], aided by the methods for exfoli-

ating and identifying atomically thin crystals inherited from the discovery of graphene [16, 17]. The thinning of bulk van der Waals crystals by mechanical exfoliation is not a sophisticated procedure (see Chapter 4.1), essentially equivalent to "writing with a pencil." The technical difficulty is finding the three-atom-thick flakes among the debris. Their enduring absence from the experimental record led to some conjecture that monolayer sheets may not even be stable, scrolling or deteriorating upon isolation from bulk crystals [18]. However, by enhancing the optical contrast through thin film interference with carefully chosen substrates [19–21], few- and single-layer flakes can be found readily with a benchtop microscope and imaged subsequently with atomic force microscopy (AFM) (Fig. 2.3b). Ultimately, the two-dimensional nature of these materials is confirmed by their distinctive physics, such as massless electron transport [22] and the integer quantum Hall effect [23] in graphene. The unique electronic and optical properties of the monolayer semiconductors are discussed next.

2.2 Band structure in two dimensions

While indirect-gap semiconductors in bulk [5], TMDCs become direct-gap semiconductors in the monolayer limit [14, 15]. This striking conversion can be explained by considering the orbital character of the involved Bloch states. The bulk indirect transition occurs between electronic states constituted by hybridized transition metal d orbitals and chalcogen p orbitals, which spatially overlap with those of adjacent layers. As neighboring layers, and thus bonding partners, are removed, the states shift in energy (Fig. 2.3c). In contrast, electronic states consisting mostly of chalcogen d orbitals at the K points in reciprocal space are centrally localized around the buried M atoms and so remain unaffected by the loss of nearby layers [25, 26]. In monolayers, these become the lowest energy states with a direct-gap transition in the visible spectral range (Fig. 2.3d). As in graphene, which shares a honeycomb crystal lattice [27], these Bloch states, the "K-valleys" in the corners of the hexagonal Brillouin zone, govern the behavior of monolayer TMDCs.

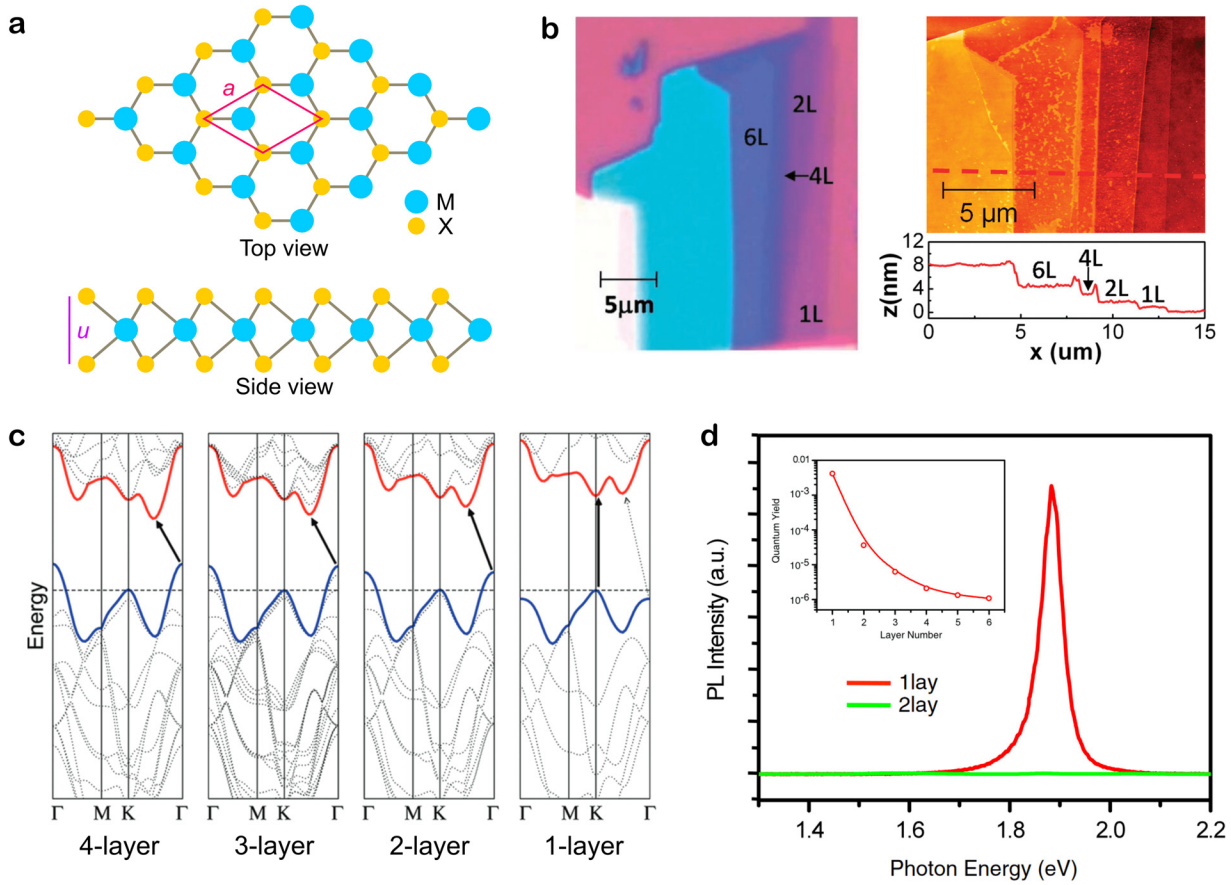

Figure 2.3: TMDC monolayers. **a**, Single-layer TMDC crystals are only three atoms thick (M = Mo, W; X = S, Se) with a honeycomb lattice. Both the lattice constant a and the layer width u are ~ 3.2 Å. **b**, Monolayers can be optically identified by their translucent appearance and profiled with atomic force microscopy. **c**, In the monolayer limit, a direct band gap emerges in the electronic structure at visible wavelengths, enabling, for example, bright photoluminescence, **d**. Figure adapted from sources: **a** – [24]; **b, c** – [14]; **d** – [15].

In addition to the presence of a band gap, the band structures of monolayer TMDCs differ from graphene in their spin and valley physics [28]. The monolayer crystal with triganol prismatic coordination lacks inversion symmetry (Fig. 2.1a). As theoretically explored for graphene with a staggered sub-lattice [29], broken inversion symmetry leads to a well-defined pseudospin – the valley degree of freedom – that distinguishes between the degenerate K and K' (or $K+$ and $K-$) valleys (Fig. 2.4a). This valley index originates from finite and opposite Berry curvatures at the K and K' points [30, 31]. Moreover, through strong spin-orbit coupling, the large orbital angular momentum of the heavy transition metal d orbitals of the K valley electronic states yields spin-splitting of the conduction and valence bands within each valley [30, 32–34]. The Bloch states of the conduction band minima are composed primarily of d_{z^2} orbitals, which, to leading order, have vanishing intra-atomic $L \cdot S$ coupling, resulting in small spin splittings of tens of meV. The valence band maxima consist of d_{xy} and $d_{x^2-y^2}$ orbitals, which have large spin-orbit coupling, yielding splittings on the order of hundreds of meV. Table 2.1 details band structure parameters computed by density functional theory [35]. Lastly, the direction of the out-of-plane electron spin inverts between valleys due to time-reversal symmetry (Fig. 2.4b,c).

Material	$E_g(eV)$	$\Delta_{cb}(meV)$	$\Delta_{vb}(meV)$	$m^1_{cb}(m_0)$	$m^2_{cb}(m_0)$	$m^1_{vb}(m_0)$	$m^2_{vb}(m_0)$
MoS_2	1.67	3	148	0.46	0.43	–0.54	–0.61
$MoSe_2$	1.40	22	186	0.56	0.49	–0.59	–0.70
WS_2	1.60	-32	429	0.26	0.35	–0.35	–0.49
WSe_2	1.30	-37	466	0.28	0.39	–0.36	–0.54

Table 2.1: Band structure parameters. Density functional theory results for the K-point band gap E_g, band spin-splitting Δ, and the upper (lower) band effective mass m^1 (m^2), which characterizes the band curvature [35]. The subscripts cb and vb correspond to the conduction bands and valance bands, respectively. The effective mass is given in units of the free electron mass m_0. Note that the band gap values shown here underestimate experimental and other theoretical predictions [36].

Polarized light provides a convenient avenue for selectively addressing the valley index [38]. In addition to contrasting Berry curvature, broken inversion symmetry leads to oppo-

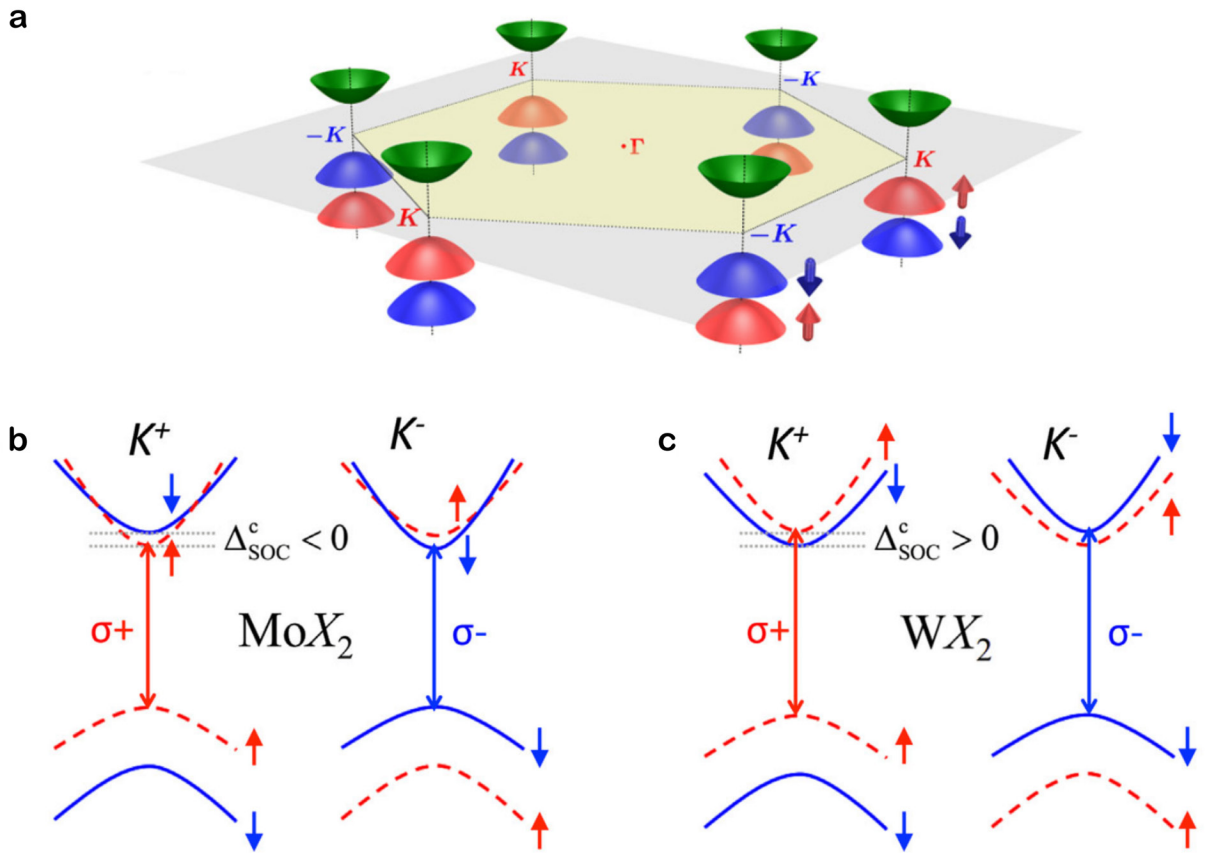

Figure 2.4: Spin-valley locking and optical selection rules. **a**, The broken inversion symmetry of the monolayer TMDC lattice yields a pair of inequivalent band gap minima at the corners of the Brillouin zone, named the $K+$ and $K-$ valleys. **b, c**, The spin degeneracy in the conduction and valance bands is broken by strong spin-orbit coupling, locking the electron spin (arrows) and valley degrees of freedom. The conduction band ordering is inverted between molybdenum-based and tungsten-based monolayers. The allowed optical transitions are in-plane and circularly polarized, $\sigma+$ and $\sigma-$, with valley-dependent chirality. Figure adapted from sources: **a** – [30]; **b, c** – [37].

sitely oriented orbital magnetic moments between the K and K' valley Bloch bands [30, 39]. Consequently, the valley-dependent optical transitions are chiral, exhibiting nearly perfect circular dichroism [40]. The K valley couples only to in-plane $\sigma+$ polarized light, while the K' valley couples only to in-plane $\sigma-$ polarized light (Fig. 2.4b,c). These strict optical selection rules enable optical initialization, coherent manipulation, and readout of the valley index [40–46]. Moreover, spin-valley locking enables optical access to the spin of resident electrons through their valley degree of freedom [47–49]. Such light-matter interactions can be mediated through excitonic states, which occupy a rich physical landscape and have oriented much ongoing research into monolayer TMDCs.

2.3 Excitons

A photon with sufficient energy excites an electron from the valance band to the conduction band. The negatively charged electron can bind through Coloumb interactions to the positively charged hole left behind in the valance band. The resulting Coloumb-correlated electron-hole quasi-particle is termed an exciton (Fig. 2.5a) [37]. The constituent electron and hole are actually coherent superpositions of Bloch electron and hole states within the K valleys (Fig. 2.5c). In real space, correlations may extend over many lattice constants, so-called Wannier-Mott excitons, or remain localized within a lattice constant, so-called Frankel excitons [50]. In TMDC monolayers, the electron and hole are tightly bound, with a Bohr radius $a_B = 4\pi\varepsilon_o\varepsilon_r\hbar^2/\mu e^2 \lesssim 1$ nm, where ε_r is the effective relative permittivity and μ is the exciton reduced mass. This value falls intermediately between the Wannier-Mott and Frankel regimes (Fig. 2.5b) and is over an order of magnitude smaller than in conventional semiconductor materials [51, 52]. Correspondingly, binding energies of hundreds of meV allow stable excitonic states even at room temperature [53, 54]. The optical band gap, *i.e.*, the photon energy needed to excite an exciton, is the electronic band gap less the exciton binding energy (Fig. 2.5d). Analogous to the Rydberg series of atomic hydrogen, excited

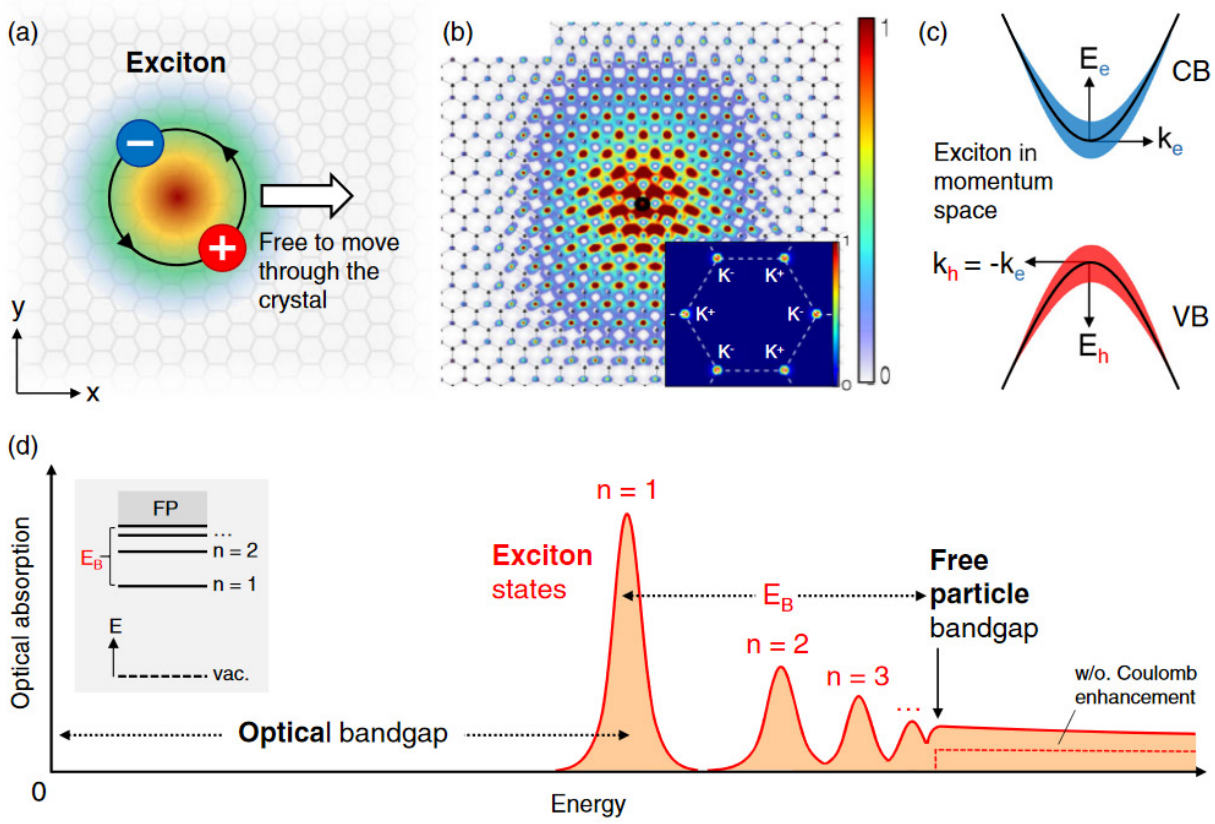

Figure 2.5: Excitonic states. **a**, Excitons are electron-hole pairs bound by Coloumb interactions. **b**, In real space, the electron and hole are spatially correlated over a few lattice constants. In momentum space (inset), excitons occupy the K valleys, composed of a superposition of electronic states (**c**). **d**, The large exciton binding energy results in an optical bangap hundreds of meV below the electronic band gap, between which excited states can be observed, analogous to Rydberg states in hydrogen. Figure adapted from source [37].

excitonic states can be observed above the optical gap until the free particle gap, where excitons "ionize" into free electrons and holes [55].

The markedly strong Coloumb interactions that give rise to such tightly bound excitons are due to quantum confinement, diminished dielectric screening, and large electron and hole effective masses [37, 56, 57]. The reduced dimensionality of the monolayer material restricts the out-of-plane extension of the electron and hole wavefunctions, leading to smaller spatial separations in comparison to bulk crystals and a fourfold increase in the binding energy. Additionally, the electric field mediating the Coloumb interaction leaks beyond the higher permittivity crystal into the surrounding lower permittivity environment, effectively decreas-

ing ε_r. The large effective masses of electrons and holes correspond to large reduced exciton masses $\mu = (m_e^{-1} + m_h^{-1})^{-1}$. A 2D hydrogen-like model provides a heuristic description of the binding energy $E_b \sim 4\text{Ry}\mu/m_0\varepsilon_r^2$, where Ry = 13.6 eV and m_0 is the free electron mass. Estimates of $\mu = 0.25m_0$, an order of magnitude larger than $\mu = 0.06m_0$ in GaAs, and $\varepsilon_r = 5$ give a binding energy around 0.5 eV [37].

Photo-excited excitons eventually relax to the vacuum ground state, during which the electron-hole pair recombines and a photon is emitted. This process, called photoluminescence (PL), is an essential spectroscopic tool for characterizing the optical properties of semiconductors [14, 15, 58]. The radiative decay rate Γ_0 is proportional to the probability of spatial co-localization of the bound electron and hole, which goes as $1/a_B^2$ [37]. The small exciton Bohr radius in TMDC monolayers thus leads to short picosecond lifetimes [59, 60], which can be observed in time-resolved PL experiments [61]. Continuous-wave PL measurements help reveal the energy spectrum of excitonic resonances. As shown in Figure 2.6b, the sulfide-based TMDCs emit in the visible (red) spectral range and selenide-based TMDCs in the near-infrared. At cryogenic temperatures, where phonon-induced broadening is suppressed, and encapsulated by hexagonal boron nitride, a van der Waals insulator that provides a uniform dielectric environment (Fig. 2.6a) [62], TMDC monolayers exhibit excitonic linewidths near the intrinsic limit $\sim$1 meV [63, 64].

Photoluminescence spectra can display complicated forests of peaks that point to the many possible relaxation pathways by which excited carriers recombine to emit light. In doped monolayers, where the Fermi level extends into the conduction or valence band, electron-hole pairs can bind with additional charge carriers to form three-particle charge states, called trions [65–67]. At high exciton densities, *i.e.*, under large excitation powers, excitons and trions bind together into neutral and charged biexciton complexes [68–70]. Such higher-order bound excitonic states are lower in energy than the bare neutral exciton by tens of meV and so appear in PL even though their oscillator strengths are weaker. Typically,

the optical response of TMDC monolayers is dominated by "bright" excitons, which preserve the electron spin and momentum. However, "dark" excitons, which are nominally spin- and momentum-forbidden, can form through various scattering processes [71–73]. Notably, in contrast to the circular in-plane optical dipoles of bright excitons, the dark, spin-forbidden optical dipole is polarized linearly out-of-plane. The weak resulting emission can be detected through wide-angle or in-plane collection [74, 75]. In tungsten-based monolayers (Fig. 2.4c), spin-forbidden dark excitons are energetically favorable, whereas bright excitons are favored in molybdenum-based monolayers (Fig. 2.4b). Excitons can also couple to the vibrational modes of the monolayer crystal, resulting in the co-emission of phonons and lower energy photons, termed phonon replicas, upon recombination [76–78]. Additionally, impurities, defects, and localized strain can trap excitonic states, which are preferably avoided in high quality samples, with the interesting exception of quantum emitters [79, 80].

Absorption spectroscopy provides a complimentary technique for studying excitonic states [58]. In a classical description, excitonic resonances can be understood as oscillating dipoles with orientation and oscillator strength determined microscopically from the transition dipole matrix element between the ground and excited electronic states [82]. Optical absorption depends on the oscillator strength and the electric field-dipole overlap (2.5d). Resonant absorption thus provides cleaner spectra, highlighting the dominant excitonic features and ignoring the weaker resonances that can obscure PL spectra (Fig. 2.6c,d). Neutral excitons appear most strongly, followed by trions – also referred to as Fermi-polarons, a correlated many-body description of neutral excitons dressed by the Fermi sea of resident charge carriers [83–86]. For convenience, reflection measurements are usually performed as a proxy for absorption, which would additionally require measurement of optical transmission. Remarkably, the neutral exciton oscillator strength is large enough to yield absorption above 10% and, aided by interference, nearly 90% reflectivity; a TMDC monolayer serves as a three-atom-thick mirror [87, 88]. Transient absorption and two-dimensional Fourier transform

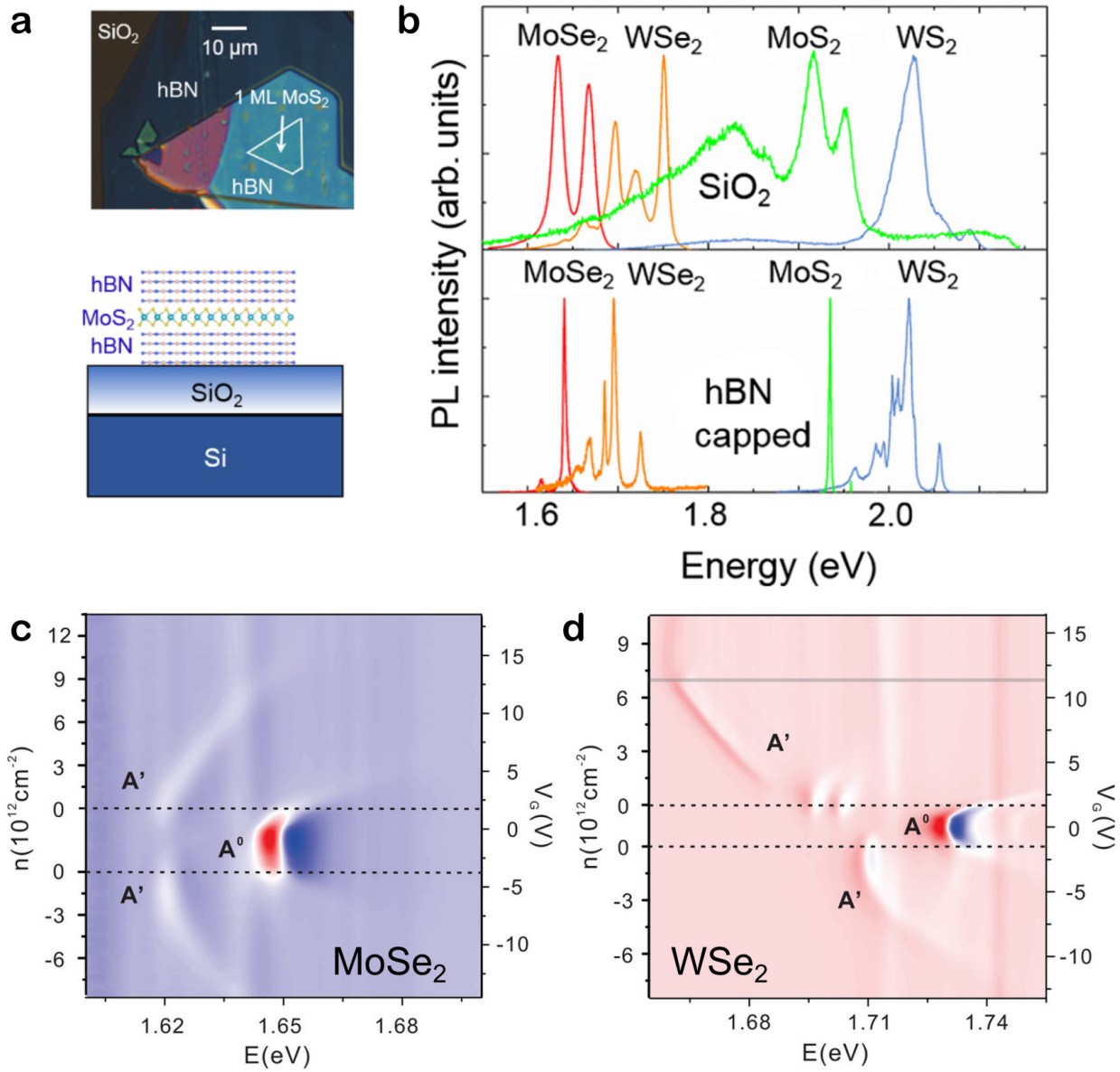

Figure 2.6: Optical response of TMDC monolayers. **a**, Encapsulation of monolayer TMDCs with hBN improves sample optical quality, yielding narrow excitonic resonances in photoluminescence spectra (T = 4 K, **b**). A complimentary technique, reflection spectroscopy directly probes the oscillator strengths of excitonic resonances (**c, d**). In doped monolayers (electron density shown on left axes), excitons bind with itinerant carriers, forming weaker, lower energy trion states. Note, the grey line in (**d**) indicates the Fermi level crossing the upper conduction band. Figure adapted from sources: **a, b** – [63]; **c, d** – [81].

spectroscopy enable further investigation of exciton dynamics and coherence [89–91].

Excitonic states inherit the valley degree of freedom and the associated chiral optical selection rules. The exciton valley polarization – the imbalance in exciton populations between the K and K' valleys – can be probed through helicity-dependent photoluminescence and absorption measurements. Valley depolarization is driven by exchange-mediated virtual recombination and opposite-valley excitation, leading to valley polarization lifetimes of several picoseconds for neutral excitons and tens of picoseconds for trions [59, 92–95]. Additionally, since trion resonances are correlated with the valley populations of resident electrons, the valley and spin polarizations of these itinerant carriers are optically accessible. Time-resolved Kerr rotation measurements, for example, have demonstrated free electron spin polarization lifetimes of hundreds of nanoseconds and free hole spin polarization lifetimes of several microseconds [96].

Moreover, the valley degeneracy can be broken through the application of external magnetic and optical fields. An out-of-plane magnetic field results in the valley Zeeman effect, in which the electronic Bloch bands shift according to their respective angular momentum [97–100]. These valley-dependent energetic shifts in the optical band-gap energy are directly detected by polarization-resolved measurements of excitonic resonances. Resident carriers, aided by interaction-driven correlations, can subsequently occupy the lower energy valley, yielding an additional imbalance in trion oscillator strengths [101, 102]. In contrast to the valley Zeeman effect, which is typically implemented using a large (~ 10 T) static magnetic field, the optical Stark effect enables dynamic valley modulation with light [103, 104]. High intensity light red-detuned from the optical band-gap creates photon-dressed states, which hybridize with the bare excitonic states, shifting the optical transition to higher energy. For circularly polarized pulsed pumps, this effect occurs only in a single valley, breaking the valley degeneracy over sub-picosecond timescales and enabling coherent control of the exciton valley degree of freedom [46].

Heterostructure engineering enables integrated control of two-dimensional semiconductors. Layered van der Waals materials can be assembled vertically in myriad stacking configurations, resulting in nanoscale composite interfaces with novel functionalities [105–107]. Encapsulation with insulating hexagonal boron nitride (hBN) significantly improves the optical quality of TMDC monolayers (Fig. 2.6a,b) [108]. Additional incorporation of few-layer graphite gates in a capacitor geometry facilitates charge accumulation in the semiconducting material, enabling *in situ* electron and hole doping (Fig. 2.6c,d). In heterobilayers, where different TMDC monolayers are directly contacted, staggered band alignment drives ultrafast charge transfer across the interface [109]. Interlayer excitons, in which the electrons and holes reside in spatially separated crystal layers, exhibit much longer radiative and spin/valley lifetimes [110]. Enhanced electrical tunability of the lateral transport of interlayer excitons and their valley properties mark promising advancements for exciton-based valleytronic devices [111, 112]. The relative twist angle between layers provides another control knob for band structure engineering [113, 114]. Moreover, these moiré heterostructures establish a new platform for exploring the exotic physics of electron correlation in quantum materials [115]. The emerging field of twistronics has duly captivated the two-dimensional materials community, beginning with the reports of unconventional superconducting and insulating states in magic-angle graphene lattices [116, 117]. However, exciting research has focused also on the physics of correlated electrons in humble TMDC monolayers, which is overviewed next.

2.4 Strongly correlated electrons

The many-body states of interacting electron systems have remained at the forefront of theoretical and experimental condensed matter physics for nearly a century [118]. Groundbreaking works by Bloch on ferromagnetism [119], Wigner on electron crystallization [120], and Mott on metal-insulator transitions [121], for example, predicted the surprising phases formed by correlated electrons in the presence of strong Coulomb interactions. The two-

dimensional electron gas (2DEG) is a workhorse model for investigating such phenomena, which is experimentally realized across a host of platforms including transistor inversion layers, liquid helium surfaces, quantum wells, and oxide interfaces [122–124]. In particular, studies on 2DEGs in GaAs and AlAs quantum wells, in dialogue with quantum Monte Carlo simulations, have revealed rich phase diagrams [125–131].

The onset of correlated phases is captured by the Wigner-Seitz parameter $r_s = 1/a_B\sqrt{\pi n}$, where a_B is the Bohr radius and n is the electron density. The dimensionless r_s parameter is the average electron separation in units of the Bohr radius and fully characterizes the system, giving the ratio of the interaction (Coulomb) energy to the kinetic (Fermi) energy [132]. At small $r_s \lesssim 1$, phase-space filling dominates in the dense electron gas, resulting in only a weakly coupled Fermi liquid. At large $r_s \gtrsim 10$, Coulomb interactions govern the dilute electron gas, enabling the formation of correlated order. Straightforwardly, material platforms that exhibit small Bohr radii and controlled, low-density carrier concentrations are desired to realize such high-r_s, interaction-driven regimes. In gold-standard GaAs quantum wells with electron Bohr radii $a_B \sim 10$ nm, electron densities of 10^{-9} cm^{-2} are needed for $r_s \gtrsim 10$, which have proved challenging to obtain due to impurities introduced during growth [126]. For TMDC monolayers, with Bohr radii $a_B \lesssim 1$ nm, the required electron densities are relaxed to 10^{-11} cm^{-2}, within reach of conventional electrostatic doping techniques. Additionally, spin-orbit coupling and the valley degree of freedom in TMDC monolayers, as well as the availability of wide-ranging optical probes, introduce interesting theoretical and experimental wrinkles for studying correlated electron phases. Recent reports on monolayer TMDCs have included fractional quantum Hall states [133], Wigner crystallization [134], and itinerant ferromagnetism [135].

The results presented in Chapter 6 engage with the growing body of work on magnetic ordering of resident electrons in doped TMDC monolayers [135–143]. Initial reflection measurements on monolayer MoS_2 found an unusual pair of polaron resonances under small

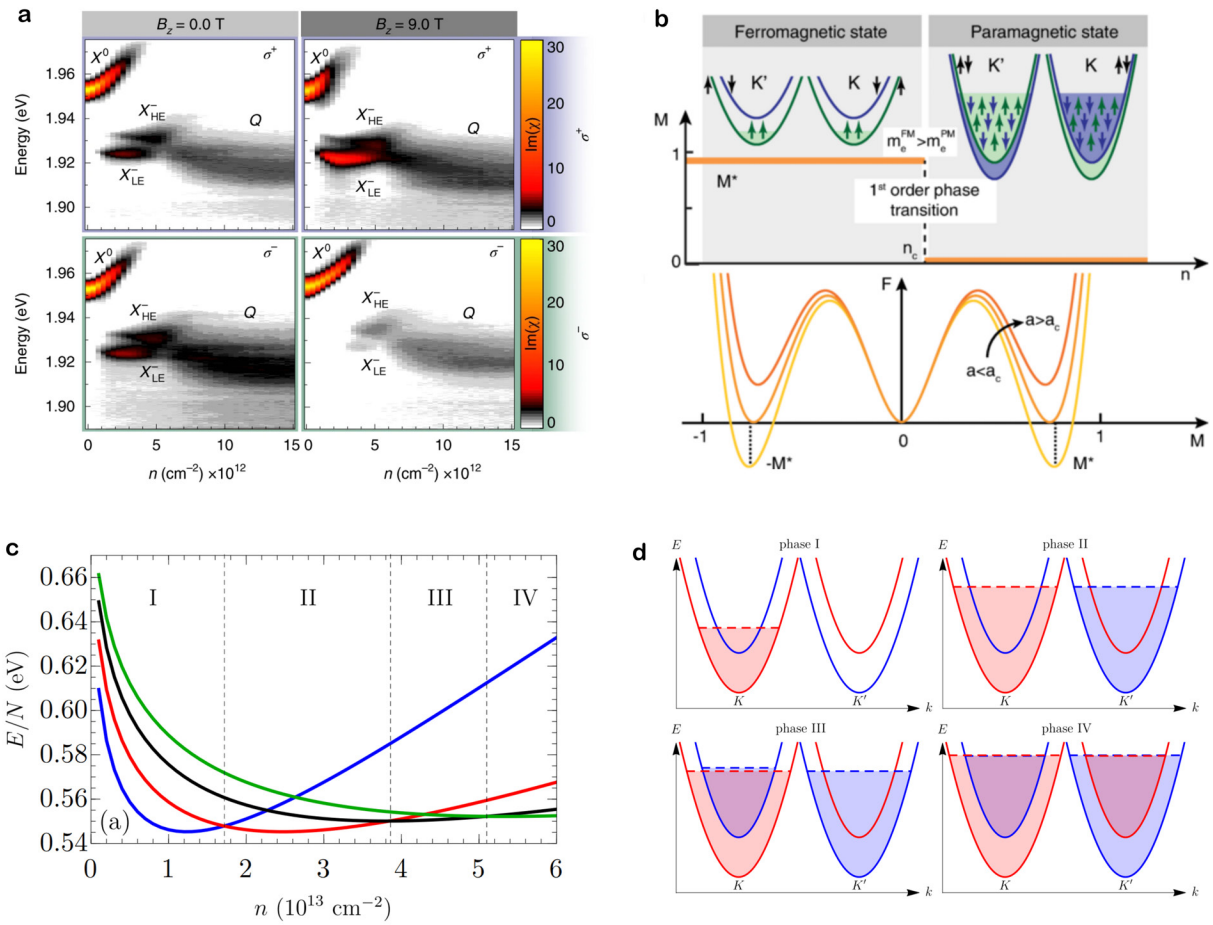

Figure 2.7: Itinerant ferromagnetism in TMDC monolayers. **a**, Under large magnetic field, resident electrons in doped MoS_2 exhibit spin polarization, which is reported through circular dichroism of polaron resonances. The spin polarization disappears with increased doping, signaling a first-order, ferromagnetic-to-paramagnetic phase transition, (**b**). **c, d**, Such spin/valley-polarized magnetic ground states are predicted for TMDC monolayers with carrier concentrations on the order of 10^{12} cm^{-2}. Figure adapted from sources: **a** – [135]; **b** – [136]; **c, d** – [137].

electron doping, $n_e \simeq 2 \times 10^{12}\text{cm}^{-2}$ or $r_s \simeq 10$, conflicting with typical MoS_2 spectra (compare Fig. 2.7a with representative Fig. 2.6c) [135]. Moreover, with the application of an external magnetic field, these resonances display strong circular dichroism. To explain the findings, a picture of interaction-induced band inversion was proposed: through intervalley exchange, an imbalance of electrons in one valley will pull the conduction band of the opposite valley below the valance band, resulting in a spin-polarized Fermi sea spanning both valleys (Fig. 2.7b). Confirmed through theoretical calculations that fully consider the electronic valley and spin degrees of freedom [140], intervalley exchange interactions are indeed sufficient to overwhelm the small spin-splitting in MoS_2 (Table 2.1). Additionally, with increasing electron concentration, the dichroic response vanishes in concurrence with the emergence of a new resonance feature, which demonstrates an abrupt change in the Fermi sea. This transition at $r_s \simeq 5$ is claimed to mark a first-order transition from a ferromagnetic to paramagnetic Fermi sea [136]. These conclusions are consonant with earlier theoretical studies of ferromagnetic phases in electron- and hole-doped monolayer TMDCs beyond MoS_2, which do not rely on band inversion (Fig. 2.7c,d) [137, 139].

The picture, however, is not completely clear, as neither spontaneous, zero-field ordering nor hysteresis was observed. It is suggested that the ferromagnetic domains are small and fluctuating (perhaps similar to the model of so-called superparamagnetism in nanoscale granular magnets [144] and oxide interfaces [145]), preventing detection in steady-state optical measurements [136]. In conventional magnetic thin films [146], the domain size scales with the film thickness – only a few angstroms for TMDC monolayers. The limit of ferromagnetism in a two-dimensional material is certainly complicated, already apparently violating the Mermin-Wagner theorem [147–149]. Yet, an initial mean field study indeed suggests domain sizes of a few nanometers [142]. Experimental techniques that can resolve such nanoscale order, such as scanning magnetometry with nitrogen-vacancy centers [150], could provide clarification. The optical control demonstrated in Chapter 6 introduces another

tool, less perturbative than a large external magnetic field, for dynamically manipulating and probing the magnetic order.

Since a full-fledged model of itinerant magnetism in TMDC monolayers remains to be developed, consider instead a simple two-electron system, which heuristically illustrates how Coulomb interactions can drive spin ordering (*i.e.*, the following treatment is adapted from reference [151] and was first used by Heitler and London to describe valence bonding in the hydrogen molecule [152]). The spin-independent Hamiltonian is:

$$H = \sum_{i=1,2} \frac{p_i^2}{2m} + V(\boldsymbol{r_1}, \boldsymbol{r_2}) \tag{2.1}$$

where the interaction term V depends on the positions of the electrons $\boldsymbol{r_1}$ and $\boldsymbol{r_2}$. The two-electron wave function is separable into orbital and spin parts:

$$|\Psi\rangle = |q\rangle^{(\pm)} \, |S; m_s\rangle^{(\mp)} \tag{2.2}$$

where the orbital (*i.e.*, spatially dependent) part is $|q\rangle$ and the spin part is $|S; m_s\rangle$. Fermion spin-statistics – or the Pauli exclusion principle – requires that the total wave function $|\Psi\rangle$ must be antisymmetric under electron exchange. Thus, if $|q\rangle$ is symmetric (antisymmetric), then $|S; m_s\rangle$ is antisymmetric (symmetric).

Directly, the spin solution is given by the antisymmetric singlet and symmetric triplet states:

$$|0; 0\rangle^{(-)} = \frac{1}{\sqrt{2}}(|\uparrow\downarrow\rangle - |\downarrow\uparrow\rangle) \tag{2.3}$$

$$|1; 1\rangle^{(+)} = |\uparrow\uparrow\rangle \tag{2.4}$$

$$|1; 0\rangle^{(+)} = \frac{1}{\sqrt{2}}(|\uparrow\downarrow\rangle + |\downarrow\uparrow\rangle) \tag{2.5}$$

$$|1; -1\rangle^{(+)} = |\downarrow\downarrow\rangle \tag{2.6}$$

The (anti)symmetry of the corresponding orbital solution is fixed, yielding total wave functions:

$$|\Psi_s\rangle = |q\rangle^{(+)} |0;0\rangle^{(-)} \tag{2.7}$$

$$|\Psi_t(m_s)\rangle = |q\rangle^{(-)} |1;m_s\rangle^{(+)} \tag{2.8}$$

Since H operates only on the orbital part, it follows that:

$$H |q\rangle^{(\pm)} = E_\pm |q\rangle^{(\pm)} \tag{2.9}$$

To find the energies $E_\pm$, consider the explicit Coulomb interactions corresponding to two electrons orbiting two stationary protons at positions $\boldsymbol{R_a}$ and $\boldsymbol{R_b}$:

$$V(\boldsymbol{r_1}, \boldsymbol{r_2}) = \frac{-e^2}{4\pi\varepsilon_0} \left(\frac{1}{|\boldsymbol{r_1} - \boldsymbol{R_a}|} + \frac{1}{|\boldsymbol{r_2} - \boldsymbol{R_b}|} + \frac{1}{|\boldsymbol{r_1} - \boldsymbol{R_b}|} + \frac{1}{|\boldsymbol{r_2} - \boldsymbol{R_a}|} \right.$$
$$\left. - \frac{1}{|\boldsymbol{r_1} - \boldsymbol{r_2}|} - \frac{1}{|\boldsymbol{R_a} - \boldsymbol{R_b}|} \right) \tag{2.10}$$

where the first line accounts the attractive electron-proton terms and the second line the repulsive electron-electron/proton-proton terms.

From the single-atom orbitals ϕ_a and ϕ_b, the two-electron orbital parts in real space can be written as:

$$|q\rangle^{(+)} = \frac{1}{\sqrt{2}} \left(\phi_a(\boldsymbol{r_1}) \phi_b(\boldsymbol{r_2}) + \phi_a(\boldsymbol{r_2}) \phi_b(\boldsymbol{r_1}) \right) \tag{2.11}$$

$$|q\rangle^{(-)} = \frac{1}{\sqrt{2}} \left(\phi_a(\boldsymbol{r_1}) \phi_b(\boldsymbol{r_2}) - \phi_a(\boldsymbol{r_2}) \phi_b(\boldsymbol{r_1}) \right) \tag{2.12}$$

The corresponding eigenvalues are found to be:

$$E_\pm = E_0 + \frac{C \pm J_{ex}}{1 \pm L^2} \tag{2.13}$$

where the Coulomb integral C, exchange integral J_{ex}, and overlap integral L are given by:

$$C = \int d^3r_1 d^3r_2 \; \phi_a^*(\boldsymbol{r_1})\phi_a(\boldsymbol{r_1})H\phi_b^*(\boldsymbol{r_2})\phi_b(\boldsymbol{r_2}) \tag{2.14}$$

$$J_{ex} = \int d^3r_1 d^3r_2 \; \phi_a^*(\boldsymbol{r_1})\phi_b^*(\boldsymbol{r_2})H\phi_a(\boldsymbol{r_2})\phi_b(\boldsymbol{r_1}) \tag{2.15}$$

$$L = \int d^3r \; \phi_a^*(\boldsymbol{r})\phi_b(\boldsymbol{r}) \tag{2.16}$$

For non-zero J_{ex} and L, the degeneracy of the singlet and triplet configurations is lifted, favoring parallel spin alignment (ferromagnetic) for $\Delta E = E_+ - E_- > 0$ and anti-parallel spin alignment (antiferromagnetic) for $\Delta E < 0$.

Additionally, an effective Hamiltonian $\tilde{H}$ can be written (*i.e.*, the Heisenberg model), which depends only on the spin degree of freedom, such that:

$$\tilde{H}\,|0;0\rangle^{(-)} = E_-\,|0;0\rangle^{(-)} \tag{2.17}$$

$$\tilde{H}\,|1;m_s\rangle^{(+)} = E_+\,|1;m_s\rangle^{(+)} \tag{2.18}$$

where

$$\tilde{H} = J_0 - J_{12}\boldsymbol{S_1}\cdot\boldsymbol{S_2} \tag{2.19}$$

The sign of the exchange constant J_{12} determines the preferred spin ordering and is related to the above interaction integrals by:

$$J_{12} = \Delta E/\hbar^2 = \frac{2}{\hbar^2}\frac{J_{ex} - CL^2}{1 - L^4} \tag{2.20}$$

To summarize, magnetism arises primarily from exchange interactions – *i.e.*, electrostatic Coulomb forces acting in concert with the Pauli exclusion principle. If, instead, magnetic dipole-dipole interactions were responsible for magnetic ordering, Curie temperatures around

1 K are predicted, nearly three orders of magnitude lower than experimentally observed. Many effective magnetic models have been developed to explain the wide variety of magnetic phenomena [151, 153, 154]. The Heisenberg model and its relatives, such as the Ising model and the XY-model, describe systems of localized magnetic moments in insulators. For the case of itinerant electrons in metals, relevant to monolayer TMDCs, the Hubbard model is often utilized, which introduces kinetic effects and incorporates the electronic band structure. Here, the kinetic cost of piling electrons into the ordered state is weighed against interaction-driven savings [155]. Even hybrid models, such as the RKKY model, can be appropriate for describing interactions between the localized moments of magnetic impurities and reservoirs of itinerant electrons [156].

CHAPTER 3

CHIRAL PHOTONIC INTERFACES

3.1 Optical spin-orbit coupling

For more than a century, it has been known that light carriers spin angular momentum in the form of elliptically polarized fields [157, 158]. Conventionally in paraxial beams, this spin angular momentum is longitudinal, associated with right-handed or left-handed field rotations about the propagation axis (Fig. 3.1a). More recently, non-trivial orbital angular momentum due to optical phase circulation was discovered in vortex beams [159, 160], invigorating new research into the exotic momentum properties of light [161]. Optical spin-orbit interactions, which intrinsically emerge from the Maxwell equations in light fields structured at the sub-wavelength scale [162, 163], give rise to optical phenomena where the spin (*i.e.*, field polarization) and orbital (*i.e.*, spatial profile and propagation) properties are correlated, adding new techniques to the modern optical toolbox for the design of photonic devices and the manipulation of matter [164–166]. A striking example of spin-orbit interactions is transverse spin angular momentum, which is carried by field components tumbling along the propagation axis (Fig. 3.1b) – so-called photonic wheels [167].

Before proceeding, note that the following independent quantities provide a complete description of the dynamical properties of classical optical fields [168]:

$$W = 4\pi \left(|\boldsymbol{E}|^2 + |\boldsymbol{H}|^2\right) \tag{3.1}$$

$$\boldsymbol{P} = \frac{4\pi}{\omega} \operatorname{Im}\left\{\boldsymbol{E}^* \cdot (\boldsymbol{\nabla})\boldsymbol{E} + \boldsymbol{H}^* \cdot (\boldsymbol{\nabla})\boldsymbol{H}\right\} \tag{3.2}$$

$$\boldsymbol{S} = \frac{4\pi}{\omega} \operatorname{Im}\left\{\boldsymbol{E}^* \times \boldsymbol{E} + \boldsymbol{H}^* \times \boldsymbol{H}\right\} \tag{3.3}$$

$$K = -\frac{8\pi}{\omega} \operatorname{Im}\left\{\boldsymbol{E}^* \cdot \boldsymbol{H}\right\} \tag{3.4}$$

where W is the time-averaged energy density; $\boldsymbol{P}$ is the canonical momentum density, which

is proportional to the local wave vector; $\boldsymbol{S}$ is the spin angular momentum density, which is proportional to and normal to the local elliptical field polarization; and K is the helicity density, which is related to the dual-symmetry between the electric and magnetic field [169].

To demonstrate the origin of transverse spin angular momentum, consider a focused, free-space beam of light with wavenumber $k = \frac{2\pi}{\lambda}$ and frequency ω allowed to propagate forward or backward in the $\pm\hat{\boldsymbol{z}}$ direction [165, 166, 168]. The electric field $\boldsymbol{E}_{\pm}(\boldsymbol{r}, t)$ is given by:

$$\boldsymbol{E}_{\pm}(\boldsymbol{r}, t) = \mathrm{Re}\left\{\boldsymbol{\mathcal{E}}_{\pm}(\boldsymbol{r})\exp[-i(\omega t \mp kz)]\right\} \tag{3.5}$$

where the mode profile $\boldsymbol{\mathcal{E}}_{\pm}(\boldsymbol{r})$ depends only on the spatial coordinates $\boldsymbol{r}$.

According to Gauss's law, the divergence of the electric field must vanish:

$$\boldsymbol{\nabla} \cdot \boldsymbol{E}_{\pm} = \mathrm{Re}\left\{\left(\frac{\partial \mathcal{E}_{\pm}^{x}}{\partial x} + \frac{\partial \mathcal{E}_{\pm}^{y}}{\partial y} + \frac{\partial \mathcal{E}_{\pm}^{z}}{\partial z} \pm ik\mathcal{E}_{\pm}^{z}\right)\exp[-i(\omega t \mp kz)]\right\} = 0 \tag{3.6}$$

Assuming the longitudinal component varies slowly along the propagation direction – *i.e.*, $\partial \mathcal{E}_{\pm}^{z}/\partial z = 0$ – its amplitude can be related to the outward decay of the transverse field components:

$$\mathcal{E}_{\pm}^{z} = \pm\frac{i}{k}\left(\frac{\partial \mathcal{E}_{\pm}^{x}}{\partial x} + \frac{\partial \mathcal{E}_{\pm}^{y}}{\partial y}\right) \tag{3.7}$$

For a Gaussian mode polarized linearly in the $\hat{\boldsymbol{x}}$ direction with a Rayleigh length $z_0 = \pi w_0^2/\lambda$ (Fig. 3.1c), the transverse components are approximately:

$$\mathcal{E}_{\pm}^{x} = \frac{1}{z_0 + iz}\,\exp\!\left(-\frac{k}{2}\,\frac{x^2 + y^2}{z_0 + iz}\right) \tag{3.8}$$

$$\mathcal{E}_{\pm}^{y} = 0 \tag{3.9}$$

The longitudinal component follows from equation (3.7):

$$\mathcal{E}_{\pm}^{z} = \mp \frac{ix}{(z_0 + iz)^2} \exp\left(-\frac{k}{2} \frac{x^2 + y^2}{z_0 + iz}\right) \tag{3.10}$$

In the focal plane $z = 0$:

$$\mathcal{E}_{\pm}^{x} \propto 1/z_0 \tag{3.11}$$

$$\mathcal{E}_{\pm}^{z} \propto \mp ix/z_0^2 \tag{3.12}$$

Note that the imaginary longitudinal component is $\pi/2$ out of phase with the real transverse component, resulting in elliptical polarization, nearly circular, spinning in the $x-z$ plane (Fig. 3.1c). Moreover, the sign of this phase, and so the rotation direction of the electric field, depends on both the propagation direction – *i.e.*, the $\mp$ factor in equation (3.12) – and the off-axis displacement – *i.e.*, the odd x factor in equation (3.12). The locking of the local ellipticity of the field polarization to position and momentum is due to optical spin-orbit coupling. The electric contributions to both the intrinsic spin angular momentum density $\boldsymbol{S}$ and the extrinsic orbital angular momentum density defined by $\boldsymbol{L} = \boldsymbol{r} \times \boldsymbol{P}$ are transverse, pointing oppositely in the $\hat{\boldsymbol{y}}$ direction. Inversions of $\boldsymbol{L}$ under $\boldsymbol{r} \to -\boldsymbol{r}$ and $\boldsymbol{P} \to -\boldsymbol{P}$ are accompanied by inversions of $\boldsymbol{S}$. Remarkably, the cycloidal field rotations are independent of the helicity $K \simeq 0$ – *i.e.*, structured, "linearly polarized" light consists locally of an elliptical electric field [171–173]. Lastly, consider the relative magnitudes of the components $\left|\mathcal{E}_{\pm}^{z}/\mathcal{E}_{\pm}^{x}\right| \propto |x|/z_0 \sim |x|\lambda/w_0^2 \sim \lambda/w_0$. The longitudinal field component, and so the transverse spin angular momentum, only becomes appreciable if the beam is tightly focused, where the beam width w_0 is on the order of the wavelength.

Nanoscale optical structures thus are natural test beds for studying the spin-orbit interactions of light. Specifically, evanescent fields ubiquitous in plasmonic systems and nanophotonic structures display robust optical spin-orbit coupling [170]. Plasmon polaritons are

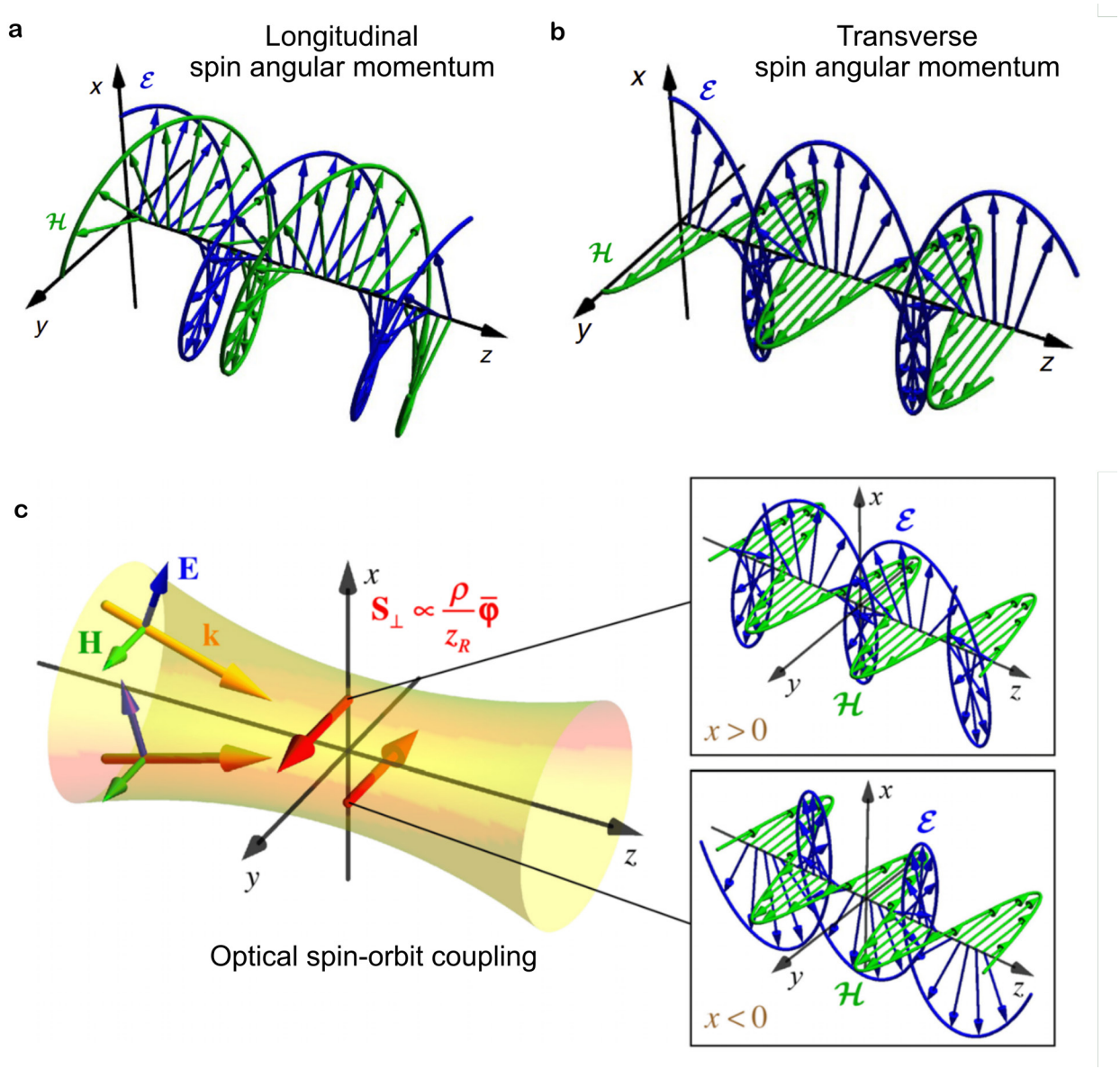

Figure 3.1: Optical spin angular momentum. **a**, Longitudinal spin angular momentum is commonly associated with helical fields rotating about the axis of propagation. **b**, Transverse spin angular momentum is carried by fields tumbling along the axis of propagation, which manifest in tightly confined light, such as a highly focused Gaussian beam, (**c**). The local ellipticity of the electric field inverts across the propagation axis and with propagation direction, an effect known as optical spin-orbit coupling. Figure adapted from sources: **a, b** – [170]; **c** – [168].

surface electromagnetic waves trapped at metal-dielectric interfaces [174, 175]. In propagating surface plasmon polaritons, the evanescent waves that exponentially decay into the bounding bulk media exhibit transverse spin angular momentum [176, 177]. As a result, circularly polarized light selectively scatters into a plasmonic mode with a propagation direction determined by the far-field helicity – the so-called quantum spin Hall effect of light [178]. This directional coupling holds for emission from a proximal circularly polarized dipole and can be engineered through patterning of the plasmonic interface (Fig. 3.2) [179–182]. Optical nanofibers and photonic crystal waveguides with sub-wavelength cross-sections also host tightly confined guided modes [183, 184]. Likewise, the evanescent field extending beyond the guiding dielectric core shows optical spin-orbit coupling, enabling directionally asymmetric scattering and emission into the propagating waveguide modes [185, 186]. These chiral photonic interfaces – *i.e.*, where the local field handedness is correlated with the mode propagation direction – open new avenues for designing directional light-matter interactions.

3.2 Chiral quantum optics

In particular, chiral interfaces have found fruitful application in the field of quantum optics [166]. More broadly, photonic technologies have been utilized to tailor the coupling of quantum emitters with light, becoming foundational hardware elements for future quantum networks [187–189]. In the case of circularly polarized emitters, chiral interfaces enable the engineering of directional single-photon emission and non-reciprocal absorption (Fig. 3.3a,d). Experimental demonstrations with quantum dots and cold atoms have reported nearly deterministic unidirectional emission routing (Fig. 3.3b,c) [190–193]. Conversely, counter-propagating photons differentially scatter off the circular emitters, breaking reciprocity and enabling single-photon isolation [194–197]. The polarity of isolation can be controlled by the internal state of the emitter, which sets the transition dipole polarization, and the magnitude of isolation can be enhanced through integration with ring resonators,

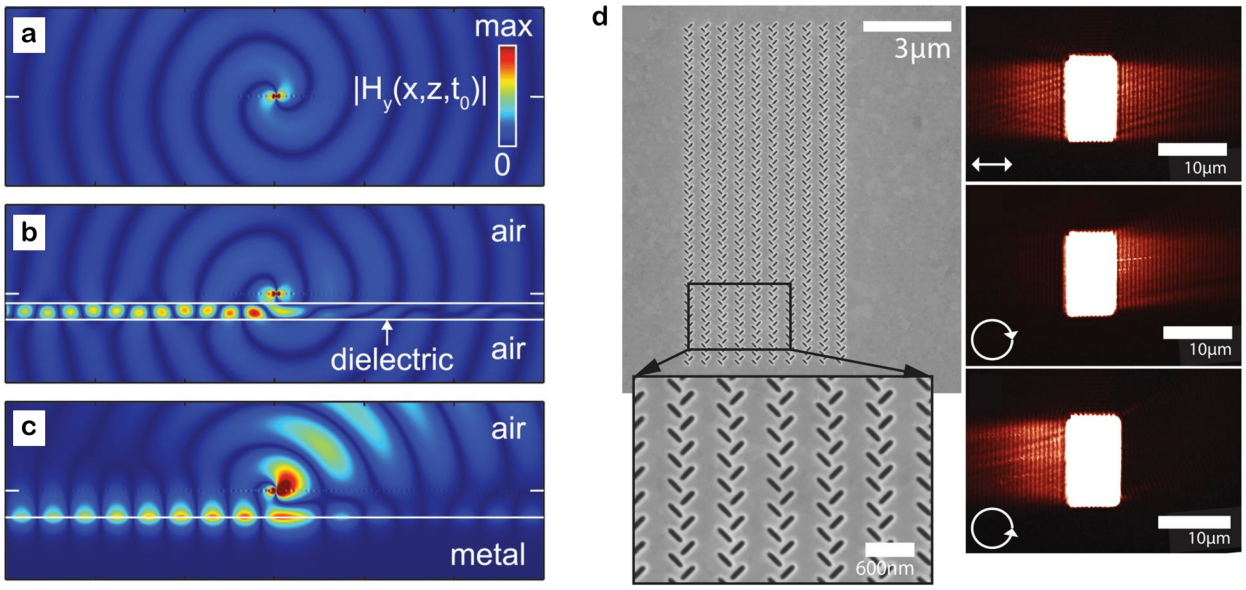

Figure 3.2: Directional coupling at chiral interfaces. A circularly polarized dipole (**a**) couples to the transverse spin angular momentum of the evanescent field of a nanophotonic waveguide (**b**) and a plasmonic interface (**c**). The excited modes propagate in a direction given by the polarization of the dipole. Such chiral interfaces enable polarization-dependent routing of light, as performed by the plasmonic groove structures in (**d**). Figure adapted from sourcess: **a, b, c** – [179]; **d** – [181].

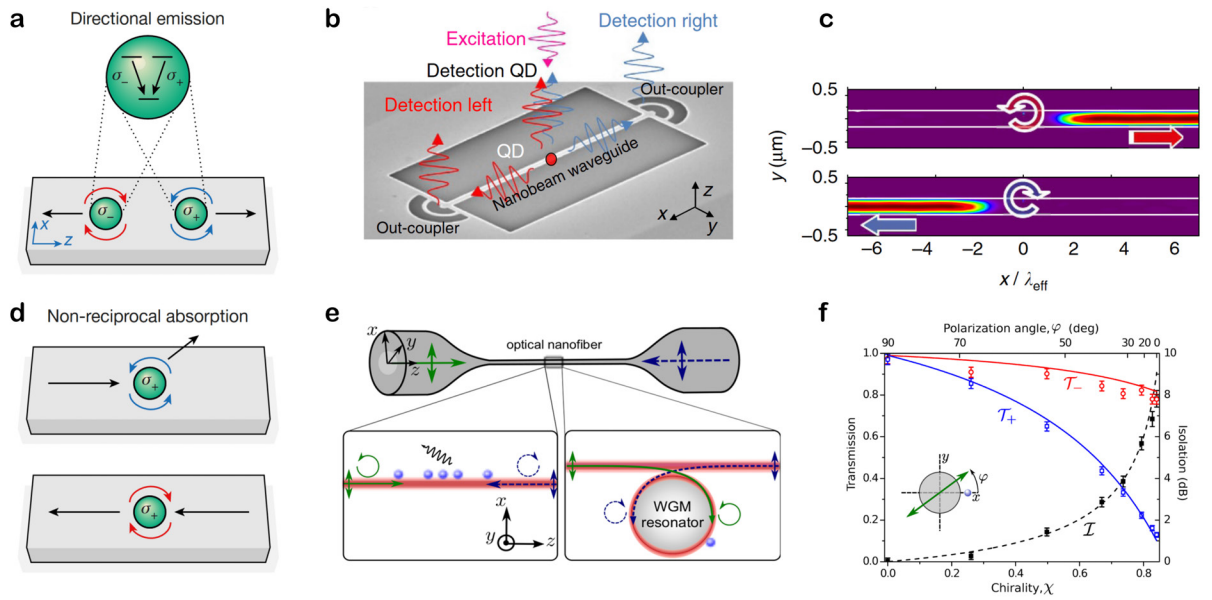

Figure 3.3: Chiral interfaces with quantum emitters. Optical spin-orbit coupling allows directional emission (**a**) and non-reciprocal absorption (**d**) of light by quantum emitters. **b, c**, Depending on the dipole polarization, embedded quantum dots preferentially emit into propagating modes of a nanobeam waveguide. **e**, Light in a nanofiber scatters non-reciprocally off an ensemble of cold atoms, displaying isolation approaching 10 dB (**f**). Instead of many atoms interacting once with the propagating mode, a ring resonator enables a single atom to interact many times with the circulating mode, resulting in single-atom controlled single-photon isolation. Figure adapted from sourcess: **a, d** – [166]; **b, c** – [193]; **e, f** – [196].

which preserve optical spin-orbit coupling [198, 199].

Beyond applications to photonic circuitry and quantum communication, chiral photonic interfaces provide a novel context for exploring quantum many-body physics [200]. Arrays of emitters interfaced with a common chiral waveguide mode are radiatively coupled to an effective unidirectional photon bath, forming a cascaded open quantum system [201, 202]. Under a coherent drive, the system collectively decays into a many-body dark state exhibiting entanglement [203–205]. Here and above, the asymmetry of light-matter interactions – even at the single photon, single emitter level – arising from optical spin-orbit coupling is the essential ingredient.

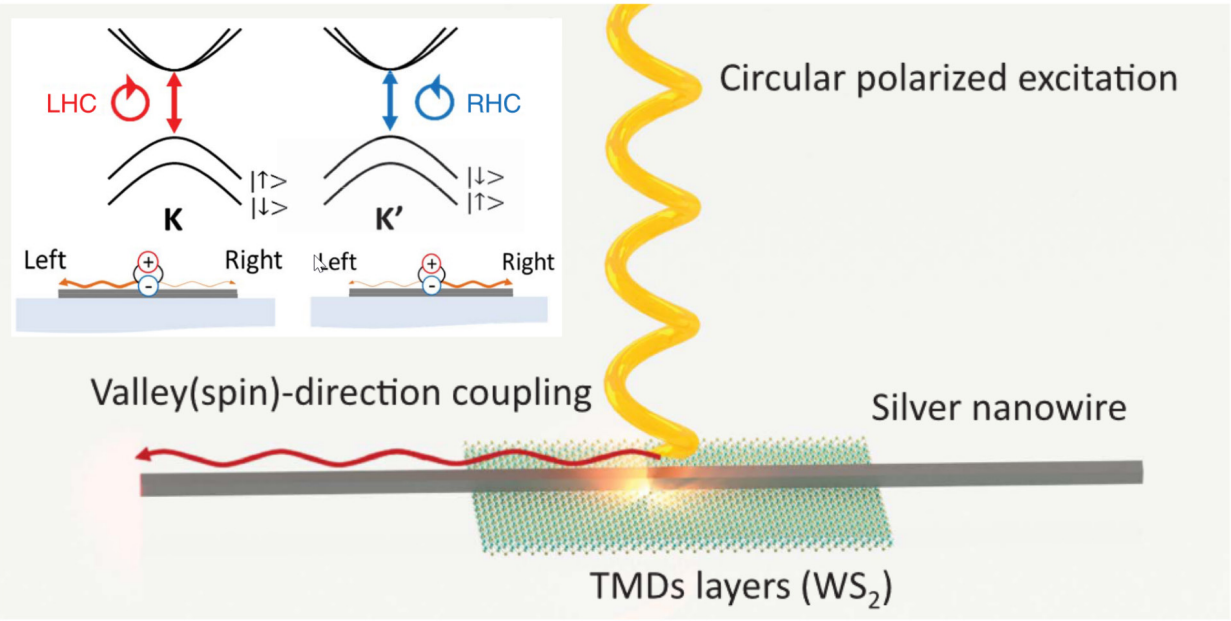

Figure 3.4: TMDC-based chiral interface. Emission from valley excitons is directionally routed into the propagating modes of a plasmonic nanowire. Figure adapted from source [215].

3.3 TMDCs for integrated chiral interfaces

Two-dimensional semiconductors are an appealing material candidate for designing integrated chiral photonic interfaces. As discussed in Chapter 2, the strong, controllable optical response of TMDC monolayers has attracted much interest for photonic and optoelectronic applications spanning photodetection, tunable emission, polaritonics, and designer metasurfaces [206–208]. Moreover, the chiral valley selection rules provide a direct route for implementation in chiral interfaces [209–211]. Indeed, within the last few years, preliminary experimental works have illustrated directional coupling between valley excitons and light in a range of nano-optical systems (Fig. 3.4) [212–222].

While these works serve as important proofs-of-principle for chiral TMDC-nanophotonic interfaces, obstacles remain for large scale incorporation into mature photonic integrated circuitry. Plasmonic structures are especially useful for their tight field confinement and so significant transverse optical spin angular momentum. However, large dissipative losses

limit propagation lengths to the order of 10 µm [223]. Additionally, previously utilized techniques for fabricating plasmonic structures – such as drop-casting – are not suitable for robust, deterministic processing. Moreover, the reported devices so far have remained passive, ignoring the suite of varied excitonic resonances available in gated TMDC heterostructures, which potentially allow for novel functionalities. Chapter 5 demonstrates a new chiral TMDC-nanophotonic interface that leverages a scalable photonics fabrication method and introduces an electrical knob for active control of emission routing.

CHAPTER 4

EXPERIMENTAL METHODS

4.1 Van der Waals heterostructure fabrication

Since the advent of graphene, two-dimensional materials have spurred fruitful ventures in engineering novel devices and exploring new physical phenomena [16–18, 22]. The isolation and identification of monolayer crystals and their assembly into high quality van der Waals heterostructures are necessary antecedents, which have received much on-going attention over the last decade [224]. Here, we employ a "top-down" method, wherein mono- and few-layer flakes are mechanically exfoliated from respective bulk crystals and deterministically placed layer-by-layer [225]. The final heterostructures can be processed further by conventional lithographic techniques – for example, the patterning of electrodes for electrostatic control and integration with photonic structures (Chapter 5). While technical refinements continue in the pursuit of scalable (re)production of pristine samples, as in references [226–229], the stacking craft has remained effectively artisanal. Below overviews our current approach.

To exfoliate atomically thin crystals, we follow the celebrated "Scotch tape" technique, shown in Figure 4.1. Low-impurity bulk crystals (*i.e.* defect concentrations $\sim 10^9 - 10^{10}$ cm^{-2}) are purchased from commercial vendors: transition metal dichalcogenides from 2D Semiconductors; graphite and hexagonal boron nitride from HG Graphene. A large flake (~ 1 mm^2) is taken from the bulk material and placed on a corner of tape (Ultron Systems) (Fig. 4.1a). Pressing the ends together and pulling apart, the flake is cleaved onto the other side of the tape (Fig. 4.1b). This process is repeated, offsetting the material at each step (Fig. 4.1b-d), until two large squares are formed (~ 1 cm^2). Each square is then duplicated (Fig. 4.1e). Because each cleavage exposes a fresh face of material, the flakes are free of tape residue. The four patches are aligned to thermally oxidized silicon substrates (*i.e.*, ~ 285 nm SiO_2 on Si enhances the visibility of monolayers), onto which the tape is draped

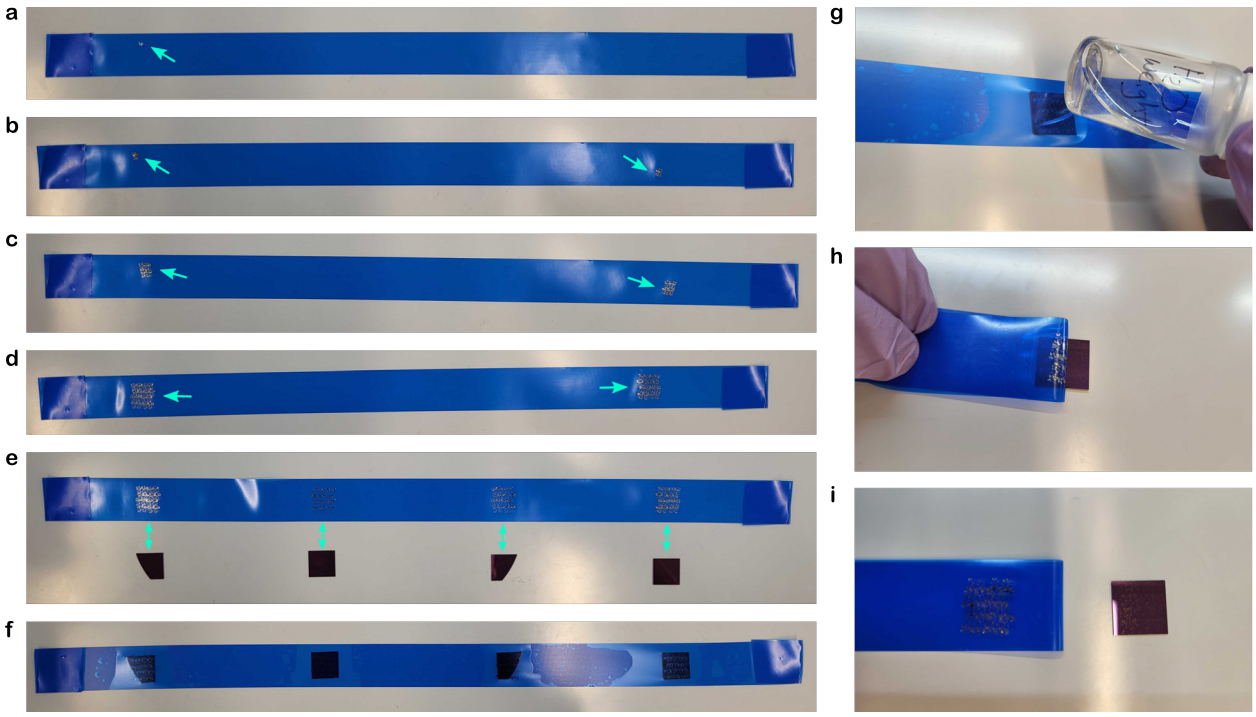

Figure 4.1: Mechanical exfoliation. Beginning with a small piece of bulk material (**a**), four patches are exfoliated through successive cleavage (**b-e**). Aligning each to an oxidized silicon substrate (**f**), the patches of material are smoothly pressed onto the surfaces (**g**). Peeling away the tape (**h**) leaves freshly cleaved material on the chips (**i**).

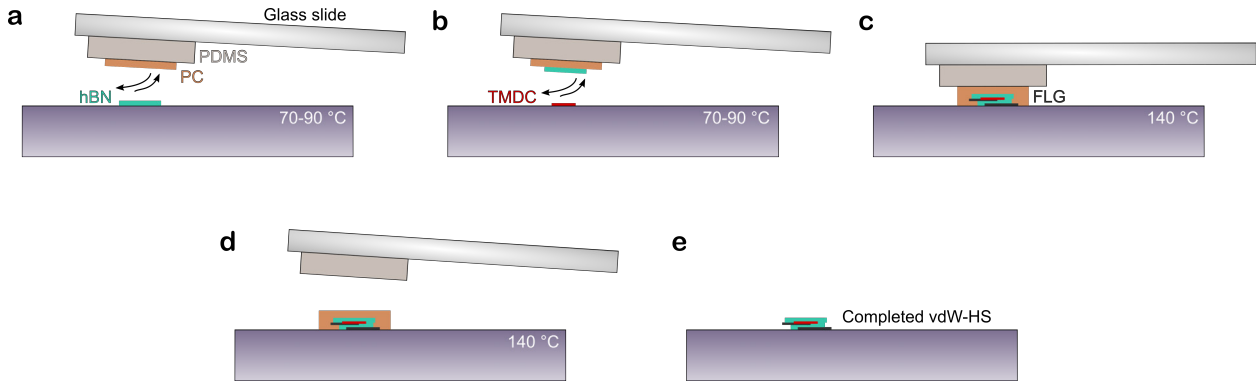

Figure 4.2: Assembly of van der Waals heterostructures. a, A PC/PDMS stamp is pressed into contact with a heated hBN flake. As the stamp is pulled away slowly, the flake is picked up with it through van der Waals adhesion. **b**, Subsequent flakes are picked up similarly by the growing stack of materials. **c**, To disengage the heterostructure, the stamp is pressed into full contact with the substrate and heated to 140 °C, where the PC film begins to soften. **d**, Withdrawing the stamp, the PC film and the encapsulated stack delaminate. **e**, Rinsing in chloroform removes the PC film.

(Fig. 4.1f). A weighted vial is then used to smooth the tape slowly over the surface of each chip, aiming for uniform contact without trapped blisters (Fig. 4.1g). The tape is peeled back – one final cleavage (Fig. 4.1h) – leaving flakes of various thicknesses on the substrate surface affixed through only van der Waals adhesion (Fig., 4.1i). Using a benchtop optical microscope, candidate flakes are identified. Using an atomic force microscope (Fig. B.1), the flakes are confirmed to be clean and verified as the appropriate height.

Figure 4.2 illustrates the process by which these materials are assembled into van der Waals heterostructures (vdW-HS). First, a viscoelastic stamp consisting of a polydimethylsiloxane (PDMS) block with a polycarbonate (PC) film approaches the top-layer flake, typically hBN (Fig. 4.2a). The substrate is held at a temperature of 70 °C–90 °C to strengthen the PC-hBN adhesion. The stamp is at a slight tilt, so that a controlled contact front forms as the stamp is lowered. The contact front is steadily advanced across the hBN flake and then slowly receded, peeling up the material as the stamp is withdrawn. If the flake is not picked up, the substrate temperature is raised. Subsequent flakes are similarly lifted, but now directly by adhesion to the preceding layers, reducing contamination from the polymer

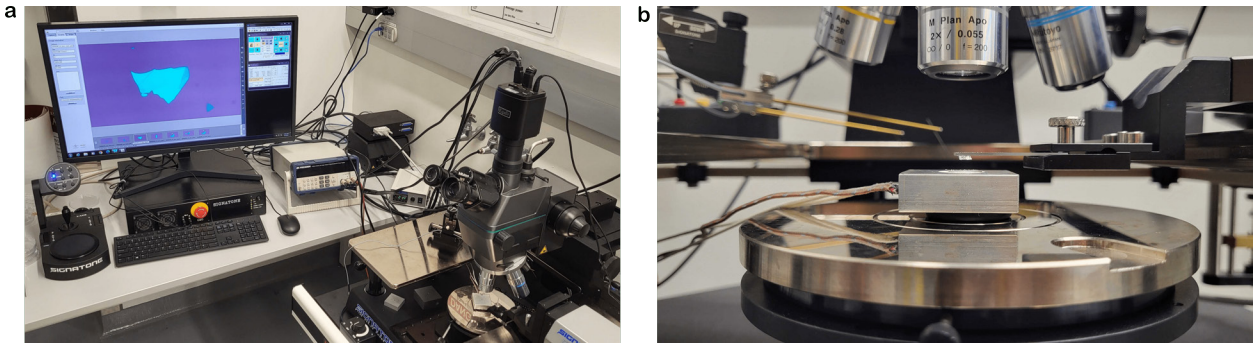

Figure 4.3: Transfer station. **a**, The assembly setup includes a probe station with computer aided positioning, an integrated microscope, and a heated stage. **b**, PC/PDMS stamp approaching the sample.

stamp (Fig. 4.2b). To deposit the finished vdW-HS, the stamp is brought into full contact with the target substrate, and the temperature is raised above 140 °C, which is near the glass transition temperature of PC (Fig. 4.2c). As the stamp is withdrawn, the PC film delaminates from the PDMS block, leaving the encapsulated structure on the substrate (Fig. 4.2d). The PC film is removed by soaking in chloroform for 10–15 minutes (Fig. 4.2e).

The transfer setup utilized for the assembly procedure is shown in Figure 4.3. A Signatone probe station equipped with long working distance objectives and a computer-aided micropositioner performs the precise flake alignment with a placement resolution $\sim$ 1 µm. A custom heated vacuum stage controls the sample temperature. The assembly is performed under otherwise ambient conditions. The stage also has a rotational knob with a few degrees of range, allowing, in principle, twist alignment between layers.

After assembly, the sample is annealed in a tube furnace at 350 °C in an inert argon atmosphere for thirty minutes. Annealing improves the adhesion between the heterostructure and the substrate and helps remove remaining residue. Patterning of electrodes and alignment markers is carried out with photolithography. Titanium/gold (5 nm/95 nm) thin films are deposited by electron-beam evaporation and lifted-off in N-Methyl-2-pyrrolidone (NMP) at 80 °C overnight. Ready for optical characterization, the sample is diced and wirebonded. Following a preliminary round of measurements, the vdW-HS may be used for interfacing

with photonic structures, whose fabrication is detailed next.

4.2 TiO_2 photonics fabrication

Adapted from: Amy Butcher, Xinghan Guo, Robert Shreiner, Nazar Delegan, Kai Hao, Peter J. Duda III, David D. Awschalom, F. Joseph Heremans, and Alexander A. High. High-Q Nanophotonic Resonators on Diamond Membranes using Templated Atomic Layer Deposition of TiO_2. *Nano Letters* **20**, 4603-4606 (2020).

Since the turn of the century, photonic nanostructures have become essential elements of next-generation technologies, enabling unprecedented control of light at the nanoscale [230, 231]. Applications range from quantum processing and communication [232–234] to energy harvesting [235] and biosensing [236]. Perhaps the most mature photonic material platform is silicon, which benefits from the advanced fabrication techniques developed by the CMOS industry and is well-suited to telecom operation [237]. Emerging alternatives include, for example, lithium niobate [238] and silicon carbide [239, 240], which possess strong electro-optical and non-linear-optical properties useful for active photonic elements, and diamond, which, in addition to silicon carbide, hosts a variety of optically addressable spin defects [241, 242].

Here, we employ an integrated photonics platform based on templated atomic layer deposition (ALD) of titanium dioxide (TiO_2). TiO_2 is chosen as the guiding material for our devices because of its high refractive index ($n > 2.3$) over a broad range of wavelengths and its relatively large bandgap ($\sim$3.3 eV), making it suitable for visible device operation [243–245]. Notably, this technique avoids etching either the sidewalls of the photonic waveguides, a major source of scattering loss, or the underlying substrate, facilitating integration with sensitive materials, such as van der Waals heterostructures (Chapter 5) and diamond membranes [246].

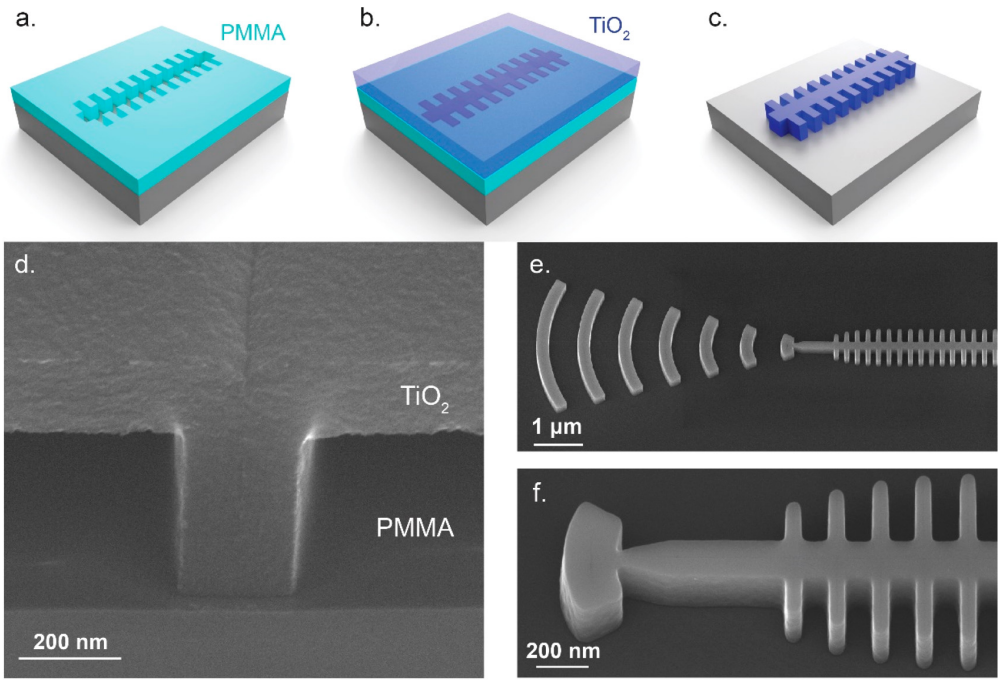

Figure 4.4: Templated deposition of nanophotonics. Nanophotonic device templates (**a**) are patterned into e-beam resist and then (**b**) conformally filled with ALD TiO_2. **c**, Overfilled TiO_2 is etched back and the resist template is stripped. **d**, 45° cross-sectional scanning electron microscope (SEM) image of a resist trench overfilled with TiO_2. **e,f**, 30° tilted SEM images of completed nanophotonic structures.

We begin our fabrication process by patterning device templates into poly (methyl methacrylate) (PMMA) via electron beam lithography (Fig. 4.4a). Next, we use ALD to conformally fill the resist templates with high-index TiO_2. To avoid reflowing the resist, the deposition occurs at 90 °C, which is below the glass transition temperature of most resists (∼105 °C for PMMA). A low chamber temperature also ensures that the TiO_2 remains amorphous rather than rutile or anatase. These other phases of TiO_2 develop during ALD at higher deposition temperatures and form grain boundaries, which can lead to scattering loss [245]. We significantly overfill the device templates to help planarize the top TiO_2 surface, where a slight crease forms (Figure 4.4d) due to the conformal filling profile.

After deposition, we etch away the excess TiO_2 with inductively coupled plasma reactive ion etching (ICP RIE) to expose the resist underneath. Importantly, because we do not etch through the resist template during this step, neither the substrate nor the device sidewalls are etched by the ICP. After removing the TiO_2 overfill, we chemically strip the remaining resist and any etch residues (Nano-Strip at room temperature or NMP at 80 °C) to reveal the templated devices (Fig. 4.4e,f). Lastly, we anneal the TiO_2 structures on a hot plate at 250 °C for 2 h, which we found was critical for reducing material optical loss.

To demonstrate the performance of this fabrication platform, we built high-Q microring resonators and 1D photonic crystal cavities on fused silica substrates (Fig. 4.5). Microring structures with radii of 5 µm display loaded quality factors above 30,000, which are quite high for their small footprint [243]. Likewise, the 1D photonic crystal cavities show quality factors approaching 20,000, corresponding to Purcell factors exceeding 100 [247]. Such high quality devices can be implemented in hybrid material interfaces for applications in quantum networking and photonic circuits (Chapter 7).

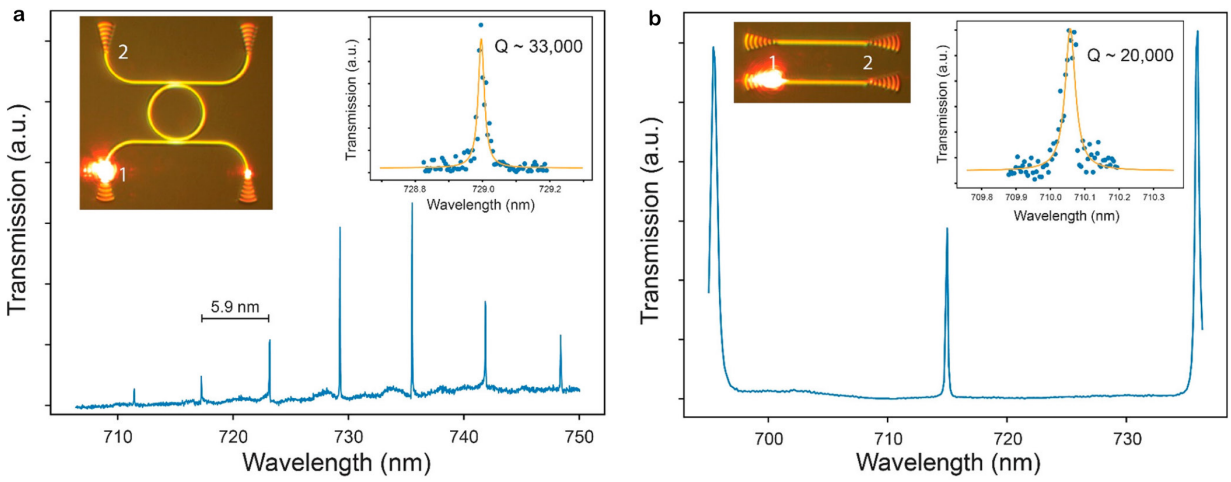

Figure 4.5: Nanophotonic devices. Microring resonators (**a**) and photonic crystal cavities (**b**) on fused silica exhibit quality factors on the order of 10^4. In each, transmission is probed from port 1 to port 2.

4.3 Optical setup

To optically characterize the above devices, we use the confocal scanning microscope shown in Figure 4.6. Confocal microscopy is a powerful tool for high resolution optical imaging with applications ranging from fluorescence mapping of biological systems to optical spectroscopy of semiconductors [58, 248, 249]. By spatially filtering the collected light through a pinhole aperture at a focal plane conjugate with the sample – or, here, by coupling into a single-mode fiber – a single focal plane with depth of field λ/NA^2 is selectively probed with lateral resolution at the diffraction limit, $\lambda/2NA$, where λ is the wavelength of light and NA is the numerical aperture of the objective. By translating the sample – or, here, by sweeping the beam direction into a 4f lens system via dual-axis scanning galvanometer mirrors – the focal plane is sampled at sub-μm^2 precision over areas of $\sim 1,000$ μm^2. In principle, the focal plane itself also can be scanned for three-dimensional reconstruction, which is helpful for imaging cellular specimen, but less so for probing two-dimensional materials.

The setup is designed to be modular to meet our varied measurement demands. Two confocal scanning systems, controlled by galvo mirrors GM1 (paths A/B) and GM2 (path C)

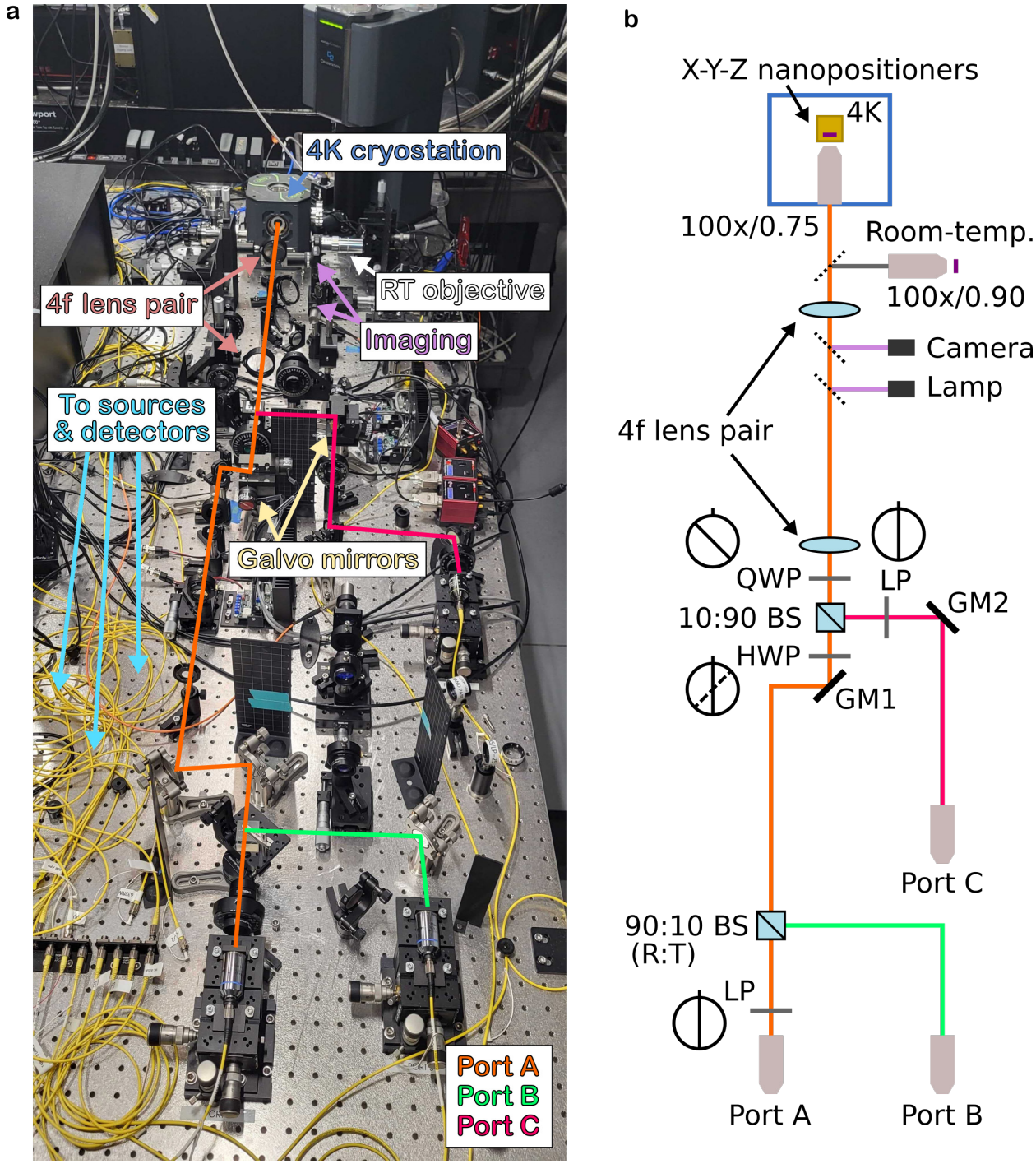

Figure 4.6: Optical setup. Image (**a**) and schematic (**b**) of the setup used for optical measurements of TMDC monolayers and nanophotonic devices. Abbreviations: GM – galvo mirror; LP – linear polarizer; HWP – halve-wave plate; QWP; quarter-wave plate; BS – beam splitter; objective magnification/numerical aperture.

(Thorlabs), are actually implemented on the same 4f apparatus, which provide independent positioning of two focused beams on the sample. This freedom allows spatially separated excitation and collection, which is useful for probing the transmission properties of nanophotonic structures and measuring spatially correlated optical properties of TMDC monolayers. Path B, collinear with path A, facilitates local measurements. A room-temperature mount (Mitutoyo objective) is typically used for rapid characterization of photonic devices, while a closed-cycle cryostation (Montana Instruments, Zeiss objective) with electrical access enables low-temperature (4 K) measurements of TMDC monolayers with gate control (Keithley Instruments). Widefield imaging for sample navigation is aided by a white LED lamp and CMOS camera (Thorlabs). The free-space optical beams are coupled through fiber launchers to single-mode patch fibers, which are connected to the desired sources and detectors. Polarization and wave plate optics (Thorlabs) can be introduced for selecting the excitonic valley index or the mode orientation of photonic waveguides, as well as for fine-tuned power control. Specific configurations relevant to the results of Chapters 5 and 6 are presented in Appendices A and B, respectively.

For TMDC monolayers, we rely on photoluminescence (PL) and reflection spectroscopy. In PL measurements, pigtailed laser diodes at above-band gap energies are employed, either at 518 nm (Thorlabs, continuous-wave), 632 nm (QPhotonics/AeroDIODE, continuous-wave or pulsed: $\sim$1 ns pulse width at $\sim$100 kHz repetition rate), or 660 nm (Thorlabs, continuous). For local measurements, the excitation is routed to path A with a short-pass filter (Semrock/AVR Optics), while path B with a long-pass filter serves as collection. The collected light is sent either to an avalanche photodiode (APD, Excelitas) for energy-agnostic imaging or to a spectrometer (Teledyne Princeton Instruments) for capturing energy-resolved spectra with wavelength resolution $\sim$0.05 nm. In reflection measurements, a pulsed ($\sim$100 ps pulse width at $\sim$ 1 MHz repetition rate) supercontinuum laser (YSL Photonics) provides a broadbrand probe spanning the energy range of the excitonic resonances, which again is

measured by the spectrometer. For high-resolution ($\sim 10^{-4}$ nm) or fixed wavelength probing, a continuous-wave Ti:sapphire laser (M Squared Lasers) is used with APD detection. Time-correlated photon counting for dynamic PL or reflection measurements is implemented with a time-tagger (quTAG, Qutools).

Polarization control is achieved with linear film polarizers and achromatic half- and quarter-wave plates. As an example, the configuration in Figure 4.6b illustrates the setup used in Chapter 6 for performing polarized pump-probe measurements of TMDC monolayers. The pump is on path C, the probe is on path A, and the collection is on path B. The pump has a fixed circular polarization, generated by the linear polarizer (LP) after GM2 and the quarter-wave plate after the 10:90 beam splitter (BS). The probe is similarly circularly polarized. However, this polarization can be alternated between right- and left-handed circular by rotating between the two indicated angles of the half-wave plate (HWP), which changes the linear polarization incident on the QWP between vertical and horizontal. The collection is unpolarized. To realize the exciton valley polarization measurements in Chapter 5, path C can be used as excitation and path A as collection. The have-wave plate now alternates between co- and cross-circular polarized PL.

For nanophotonic devices, the transmission response is studied in a similar manner as the reflection measurements above. The broadband supercontinuum laser provides a coarse probe, while the tunable Ti:sapphire laser resolves narrow cavity features (Fig. 4.5). The TE-like and TM-like waveguide modes can be selected by polarizing the probe beam and rotating the polarization with a HWP to align parallel or perpendicular to the grating coupler. The transmission can be quite sensitive to the probe and collection positions, which can require iterative adjustments to find the optimal signal.

CHAPTER 5

ELECTRICAL CONTROL OF NANOPHOTONIC CHIRALITY

Adapted from: Robert Shreiner†, Kai Hao†, Amy Butcher, and Alexander A. High. Electrically controllable chirality in a nanophotonic interface with a two-dimensional semiconductor. *Nature Photonics* **16**, 330-336 (2022).

Chiral nanophotonic interfaces enable propagation direction-dependent interactions between guided optical modes and circularly dichroic materials. Electrical tuning of interface chirality would aid active, switchable non-reciprocity in on-chip optoelectronic and photonic circuitry, but remains an outstanding challenge. Here, we report electrically controllable chirality in a nanophotonic interface with atomically thin monolayer tungsten diselenide (WSe_2). Titanium dioxide (TiO_2) waveguides are directly fabricated on the surface of low disorder, boron nitride-encapsulated WSe_2. Following integration, emission from excitonic states into the waveguide can be electrically switched between balanced and directionally biased. The operational principle leverages the doping-dependent valley polarization of excitonic states in WSe_2. Furthermore, the nanophotonic waveguide can function as a near-field source for diffusive exciton fluxes, which display valley and spin polarizations inherited from the interface chirality. Our versatile fabrication approach enables deterministic integration of photonics with van der Waals heterostructures and opens new pathways towards optically driving their excitonic and charge carrier behavior.

†. These authors contributed equally to this work.

5.1 Introduction

In tightly confined, propagating optical fields, Gauss' law requires that a rapidly varying electric field in the transverse direction must be accompanied by an electric field in the longitudinal direction that is 90° out of phase with the transverse field [164, 165]. The transverse and longitudinal field components combine to create regions of elliptical polarization in which the transverse component of the optical spin angular momentum is locked to the direction of the wavevector of the optical mode. Notably, in such tightly confined fields, the optical spin angular momentum has a component perpendicular to the propagation direction, in contrast to paraxial circularly polarized free-space optical fields. This phenomenon, referred to as optical spin–orbit coupling (OSOC), has been observed in a variety of experimental platforms, including optical fibres [185, 191, 196], whispering gallery mode resonators [195–197], photonic crystal waveguides [186, 192], plasmonic waveguides [215] and hyperbolic metamaterials [250] and metasurfaces [251].

Photonic structures exhibiting OSOC can be coupled with circularly dichroic materials – that is, materials that interact selectively with circularly polarized light – to generate chiral light–matter interfaces. Such interfaces create light-matter interactions that depend on the propagation direction of the light and provide a foundation for new photonic and plasmonic technologies, such as on-chip beam splitting for circularly polarized input light [181] and optically driven optical isolation [252]. Beyond classical systems, OSOC enables directional quantum nonlinear interactions between quantum states of photons and matter and has stimulated the development of chiral quantum optics [166].

An emerging platform for these chiral optical interfaces is atomically thin transition metal dichalcogenides (TMDCs). TMDC monolayers are direct bandgap semiconductors with optical resonances in the visible and near-infrared range dominated by excitonic states [14, 15]. Owing to broken inversion symmetry in the monolayer crystal lattice, two inequivalent sets of bandgap minima exist at the momentum space K points (that is, K and K' valleys),

which couple to light of opposite circular polarization [30, 40–42]. Preliminary demonstrations with plasmonic, nanowire and photonic crystal systems have shown the feasibility of coupling light to TMDC valley excitonic states through OSOC [212, 215–220]. However, the scalable, deterministic incorporation of such architectures in existing integrated photonic platforms is challenging to achieve due to large propagation losses, restrictive design constraints and poor processing compatibility with delicate TMDC materials. Moreover, the chiral TMDC interfaces demonstrated so far are passive. A scalable nanophotonic–TMDC interface equipped with active electrical tunability could enable new applications in optoelectronic and integrated photonic technologies. Valley polarization, which characterizes the circular dichroism of TMDCs, can be modified via electrostatic doping [253], providing an avenue for active control. In addition, in monolayer TMDCs, in contrast to the multilayer TMDCs used previously [215], the exciton valley index determines the spin configurations of the underlying charge carriers in charged excitonic states [30]. Therefore, a photonic–TMDC interface also provides the opportunity to control semiconductor spins [254] with integrated photonics, enabling nanoscale optical manipulation of solid-state memories [255, 256].

5.2 Electrically controlled chiral interface

Here, we demonstrate an interface that exploits these unique material properties to realize electrically tunable chirality. The interface is based on deterministic fabrication of nanophotonic structures on arbitrary substrates and can be applied to a range of devices, facilitating broader application of chiral interfaces in nanophotonic circuitry. Our device consists of a titanium dioxide (TiO_2) nanophotonic waveguide fabricated on a WSe_2 monolayer that is encapsulated in hexagonal boron nitride (hBN) (Fig. 5.1a). Encapsulation with hBN substantially reduces inhomogeneity in TMDCs [63, 64] and serves as a dielectric for electrostatic tuning [74]. Electrical control is achieved with a few-layer graphene (FLG) back gate and contact flakes (for fabrication details, see Appendix A.1). We fabricate TiO_2 waveguides on

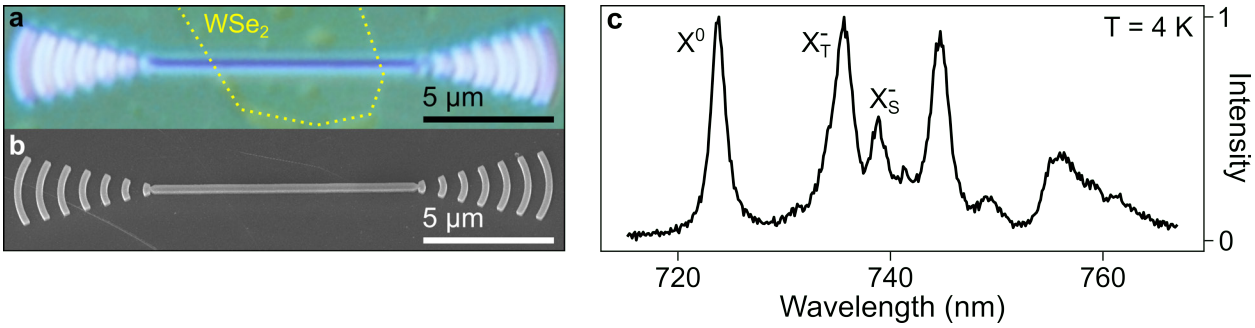

Figure 5.1: Fabricated TMDC-photonic waveguide interface. Optical (**a**) and scanning electron microscope (**b**) images representative of the TMDC-waveguide interface. **c**, PL of encapsulated WSe_2 at 4 K shows prominent exciton, trion and charged biexciton peaks.

top of these heterostructures using templated atomic layer deposition [246]. This fabrication method produces low-loss nanophotonic structures (Fig. 5.1b) without damaging the underlying substrate, making it ideal for interfacing with two-dimensional materials (for an image of the measured device, see Fig. A.1). Following waveguide fabrication, the WSe_2 monolayer exhibits narrow linewidth excitonic emission (Fig. 5.1c), confirming that our photonic integration process generates minimal inhomogeneities in the van der Waals heterostructure and is suitable for photonic integration with TMDCs.

Figure 5.2 illustrates the directional coupling that emerges between the waveguide modes and the TMDC material. The electric field distribution (for full simulation data, see Appendix A.3) of the propagating transverse electric mode is tightly confined (waveguide width $< \lambda/2$, manifesting in-plane, circularly polarized evanescent fields (Fig. 5.2, right inset). The sign of the polarization, $\sigma+$ or $\sigma-$ (for definitions, see Appendix A.3), inverts across the waveguide and with the propagation direction. Depending on their location, excitons in the K and K' valleys (Fig. 5.2, left inset) will selectively couple to left- or right-wards propagating modes of the waveguide, thus establishing chiral–directional coupling at the waveguide–monolayer interface.

To characterize the interface, we first generate excitons and observe their radiative emission into the guided optical modes of the waveguide. The monolayer is excited from the

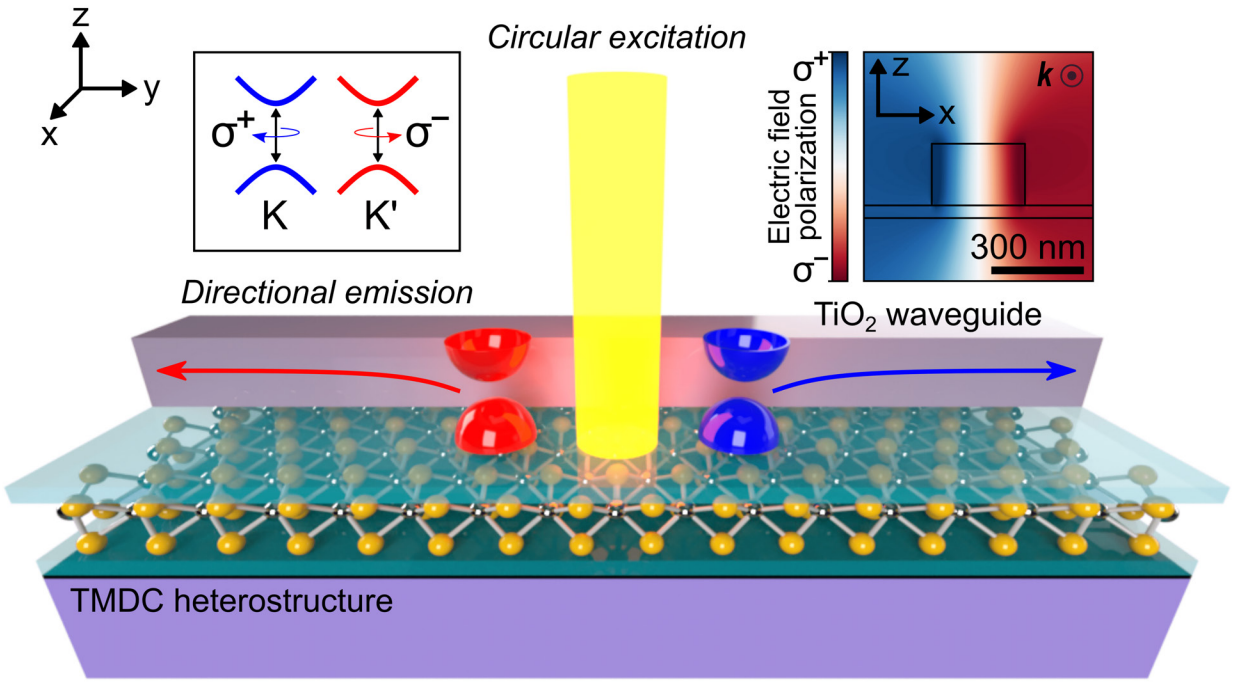

Figure 5.2: Chiral-directional coupling. Schematic depicting chiral-directional coupling of emission from valley excitons into the propagating modes of the waveguide. Left inset: Valley-dependent optical selection rules of monolayer TMDCs. Right inset: Polarization of electric field distribution of waveguide mode propagating out of the page.

far-field using a 660 nm laser with a spot size ∼495 nm (see Appendix A.2). Excitonic photoluminescence (PL) couples to the waveguide and is detected via collecting the light scattered from gratings at the waveguide ends. Figure 5.3a displays the measured PL intensity from the left port (for the right port data, see Fig. A.9d) when a linearly polarized excitation is scanned around the waveguide. To study the chiral–directional coupling, we switch the polarization of the excitation laser from linear to circular, $\sigma+$ and $\sigma-$, creating valley-polarized excitonic states that preferably emit with the same polarization as the excitation (Fig. 5.2). We characterize the interface using the chiral–directional coupling efficiency (CDCE). Here, $\mathrm{CDCE}(x,y) = (I_{GP}^{\sigma+}(x,y) - I_{GP}^{\sigma-}(x,y))/(I_{GP}^{\sigma+}(x,y) + I_{GP}^{\sigma-}(x,y))$, where $I_{GP}^{\sigma+(\sigma-)}(x,y)$ is the PL intensity measured from a specific grating port under $\sigma+(\sigma-)$ excitation at position (x,y). Figure 5.3b shows the spatial mapping of the CDCE for left port collection (for the right port data, see Fig. A.9e). As anticipated [215, 218], we observe that the sign of the CDCE inverts as the excitation spot crosses the waveguide, approaching a magnitude of 20%, and that the sign of the CDCE flips between the two outcoupling ports (Fig. 5.3c). We also note that under linearly polarized excitation, the chiral–directional coupling vanishes as expected (Fig. A.9c,f). For both ports, the CDCE goes to zero near the centre of the waveguide ($x = 0$ µm), where the mode polarization is linear (Fig. 5.2, right inset). Far from the waveguide centre, the CDCE also falls to zero as the low signal-to-noise ratio dominates. These experimental signatures directly verify the predicted chiral interface between the TMDC monolayer and the photonic waveguide.

The integration of contacts and electrodes in our device architecture enables us to electrically dope the TMDC monolayer and, in turn, potentially control the chirality of our integrated photonic interface. To study this tunability, we apply a gate voltage to the TMDC monolayer and investigate the impact on the chiral-directional coupling. Figure 2a,b show the spatially mapped CDCE measured for gate voltages of -5 V and +5 V, respectively (for the right port data, see Supplementary Fig. A.10d,f). The CDCE notably diminishes under

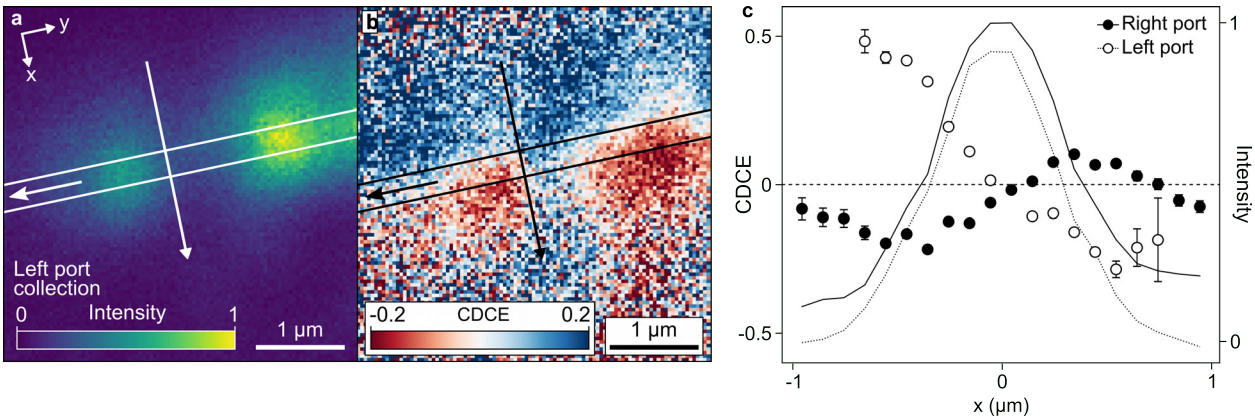

Figure 5.3: Spatial imaging of CDCE. a, PL intensity measured through the left port under linear far-field excitation. **b**, CDCE through the left port under circular far-field excitations. **c**, Line cuts of CDCE across the waveguide along the arrow direction in e and f for left (open circles) and right (solid circles) ports. Lines show total intensity (*i.e.*, $I_{GP}^{\sigma+} + I_{GP}^{\sigma-}$) measured for each port. Data points are presented as mean values over the full spectral range with error bars corresponding to 1SD of the background noise.

negative applied bias. Comparing transverse line cuts across the waveguide (Fig. 2c), the CDCE spatial dependence at -5 V flattens to zero, whereas at +5 V it displays the expected crossing at $x = 0$ μm. At a fixed displacement of ∼300 nm away from the waveguide, we observe a sharp transition in CDCE from near 0% at -5 V to around 15% at -2.5 V (Fig. 2c, inset). This result directly demonstrates the active electrical control over the chirality of the TMDC-waveguide interface.

To investigate the electrical tuning in more detail, we perform spectrally resolved measurements of the out-coupled PL. Figure 5.5a–d shows gate-dependent PL spectra collected from the right grating port for fixed-position off-waveguide $\sigma+$ and $\sigma-$ excitations. We attribute the characteristic peaks to the neutral and charged exciton and biexciton states delineated in recent literature reports [253, 257, 258]. Combining this spectroscopic information with the electrostatic control afforded by our high-quality interface, we analyse the chiral-directional coupling for each excitonic state. From the spectra in Fig. 5.5a–d, we find that the positive trion (X^+) and neutral exciton (X^0) states display balanced emission into the waveguide, independent of the excitation polarization. By contrast, the negative

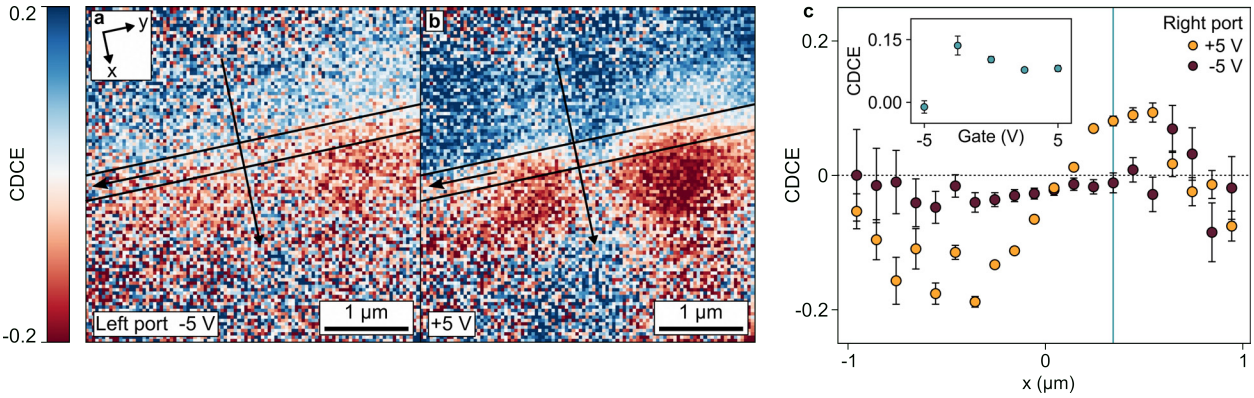

Figure 5.4: Gate control of CDCE. Spatial mapping of CDCE of emission collected through left port under applied gate biases of (**a**) -5 V and (**b**) 5 V. **c**, Line cuts of CDCE of emission collected through right port along the arrow direction. Inset: Gate dependence of CDCE at $x \approx +300$nm (blue vertical line in **c**). Data points are presented as mean values over the full spectral range with error bars corresponding to 1SD of the background noise.

trion (X^- and X^{--}) and biexciton (XX^0 and XX^-) states exhibit directional emission. More completely, Fig. 5.5e–h(i–l) shows the wavelength-resolved right (left) port CDCE versus the position of the excitation beam. Minimal variation is observed for the X^+ and X^0 peaks, whereas for the X^-, X^{--}, XX^0 and XX^- peaks, the CDCE inverts across the waveguide and reaches magnitudes near 20% on either side (for complete data, see Fig. A.11). These measurements indicate that the different excitonic states in the monolayer exhibit varying degrees of chiral–directional coupling and that the electrostatic control of this coupling correlates with switching between the dominant excitonic states.

5.3 Exciton valley polarization

To better understand the doping-dependent chiral–directional coupling for different excitonic states, we perform gated far-field PL measurements of the encapsulated WSe_2. Figure 5.6a shows the unpolarized PL versus the wavelength and gate voltage, which exhibits characteristic peaks for different doping regimes. Figure 5.6b plots the degree of circular polarization (DOCP), which characterizes the valley polarization P_v, defined as $P_v = (I_{co} - I_{cross})/(I_{co} + I_{cross})$, where $I_{co(cross)}$ refers to the PL intensity collected

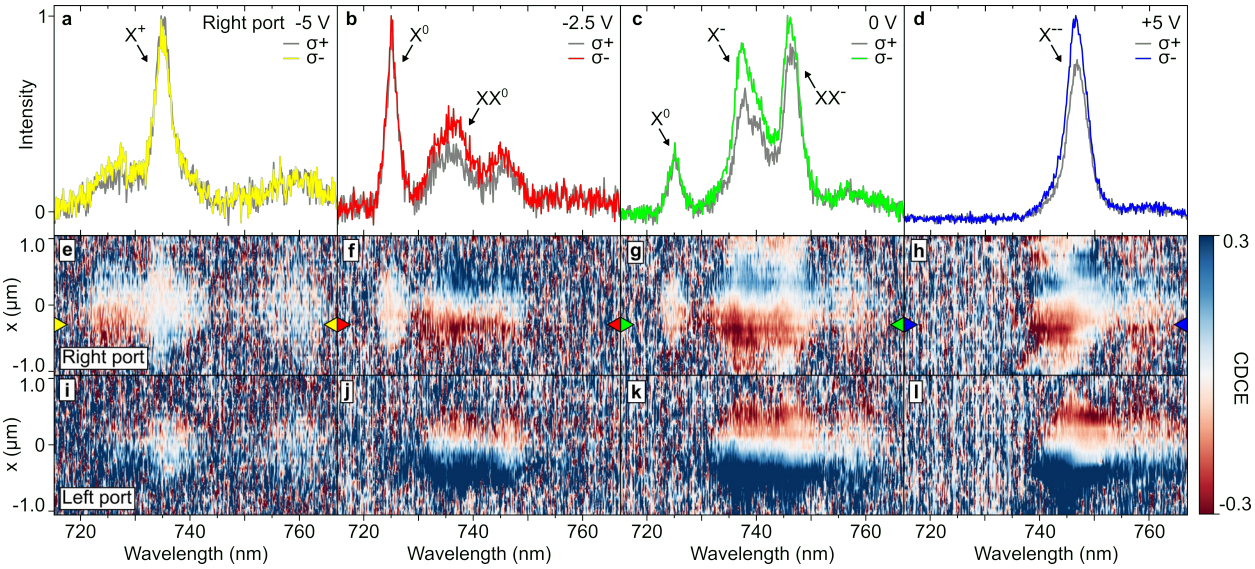

Figure 5.5: Spectrally resolved CDCE. a-d, PL out-coupled from right port under selected gate voltages with $\sigma+$ and $\sigma-$ excitations fixed at $x \approx -300$nm. Excitonic states are labeled. **e-h** (**i-l**), Spectrally resolved spatial mapping of right (left) port CDCE at selected voltages. Colored triangles indicate the corresponding spectra line cuts in **a** through **d**.

co(cross)-circularly polarized to the excitation. Importantly, the valley polarization results revealed here agree with the chiral-directional couplings of the respective excitonic states at the interface. Notably, X^+ shows no valley polarization, which explains the quenched waveguide coupling in the hole region, while X_T^- (triplet trion) and X^{--} show the strongest far-field polarization, as well as the clearest CDCE signatures. Considering these far-field valley polarization results, we fit the measured CDCE profiles for the excitonic states to simulations and find an isolated interface fidelity as high as 90 $\pm$ 2 % (see Supplementary Section 2).

Our observation of widely differing valley polarizations for different species can be understood by considering valley relaxation processes that occur at differing rates. We consider two distinct processes that contribute to valley relaxation: the exchange interaction and the intervalley charge-carrier scattering. The exchange interaction is considered the primary depolarization mechanism for neutral excitons and negative trions [92, 95]. The fast scattering of electron–hole pairs into the opposite valley depolarizes neutral excitons (Fig. 5.7a).

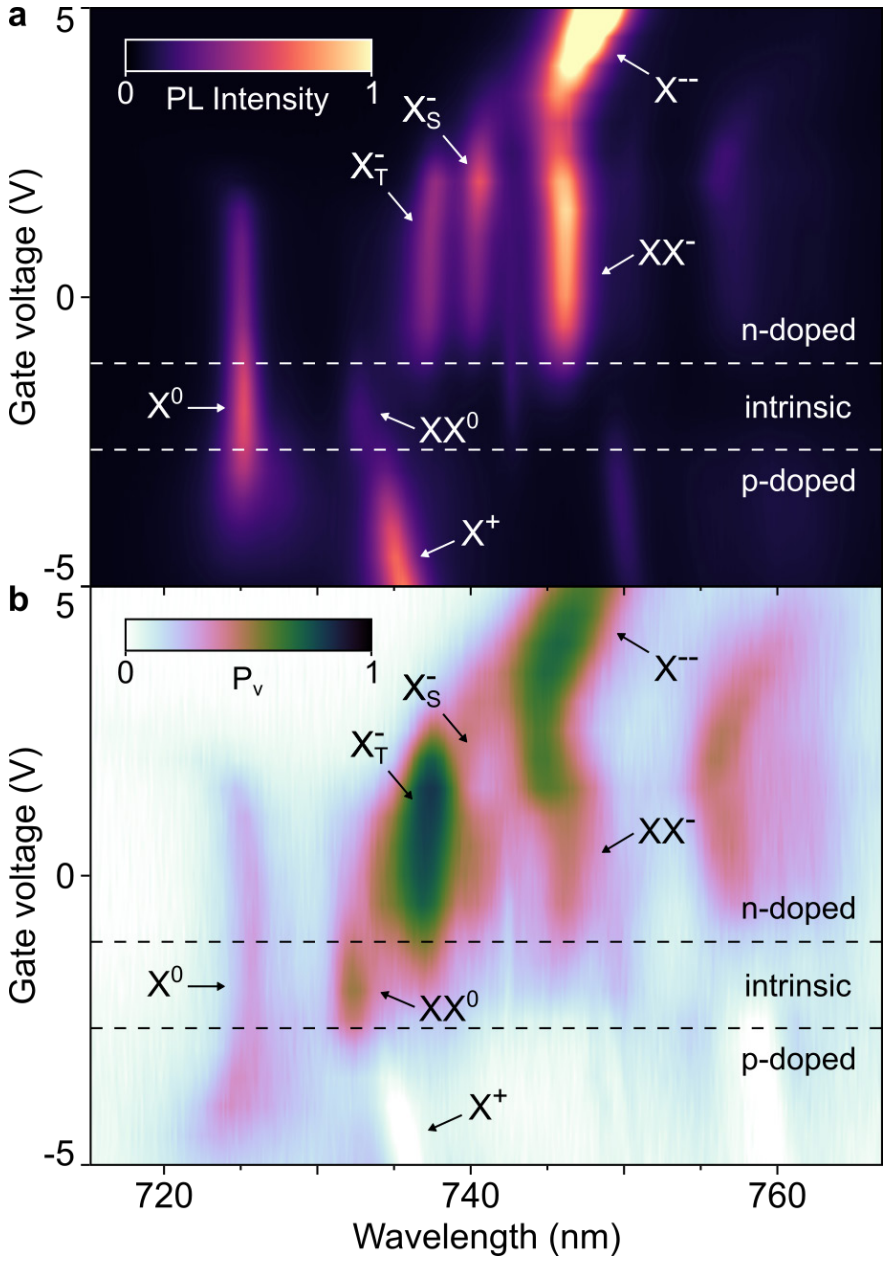

Figure 5.6: Gate-dependence of valley polarization. **a**, Unpolarized PL spectra versus gate voltage under far-field excitation and collection. Relevant excitonic states are highlighted, and approximate doping regimes are labelled. **b**, P_v of emission from electrostatically tuned excitonic states in WSe_2.

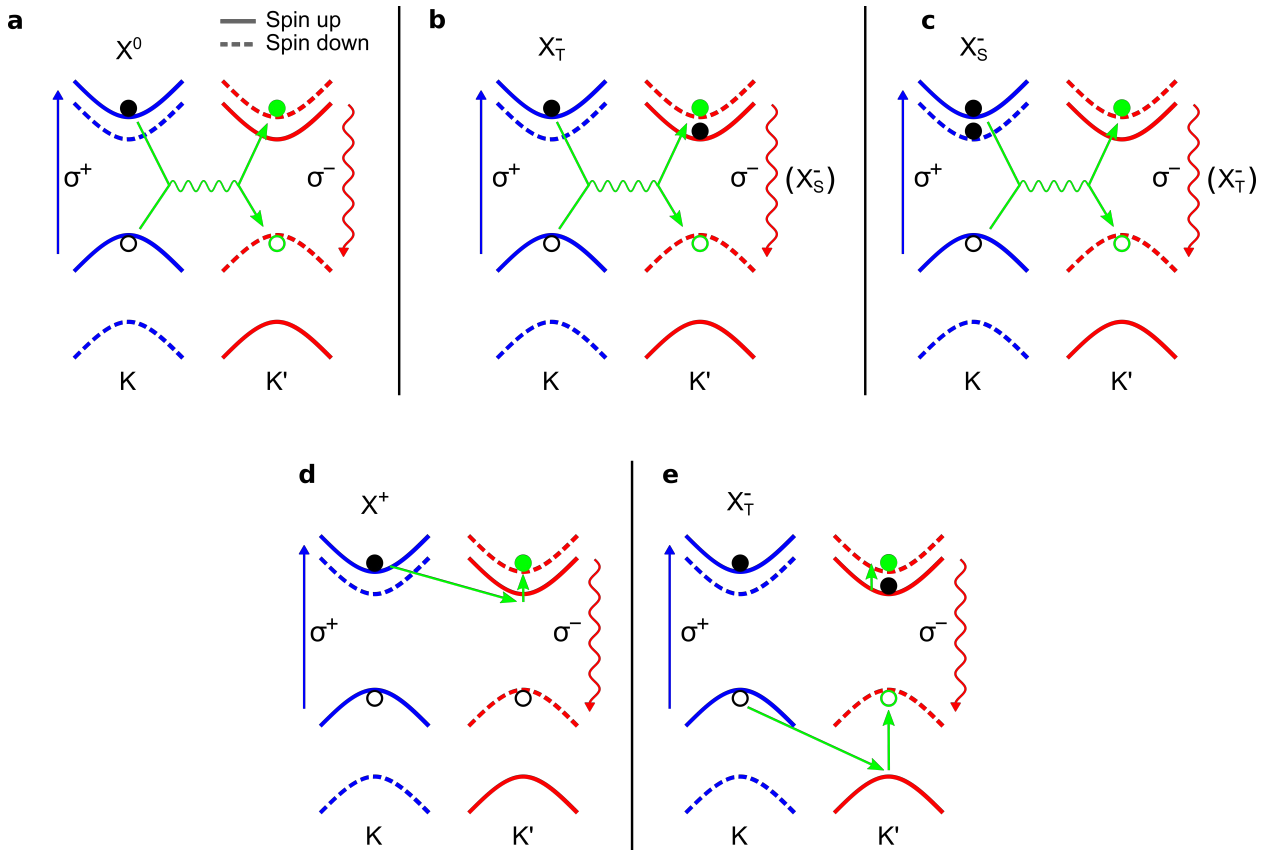

Figure 5.7: Valley depolarization mechanisms. **a**, Fast neutral exciton valley depolarization from exchange interaction. **b**, Exchange interaction-induced fast relaxation from K valley trion triplet to K' valley trion singlet. **c**, Energy unfavorable relaxation from K valley trion singlet to K' valley trion triplet. **d**, Electron intervalley scattering of positive trions. **e**, Hole intervalley scattering of negative triplet trions, suppressed due to large valence band splitting.

Through this same process, the K valley triplet trions rapidly relax to the energetically lower singlet trions (X_S^-) in the K' valley, quickly eroding the polarization of existent singlet trions (Fig. 5.7b). Inversely, the depolarization of triplet trions can result from exchange-interaction-induced intervalley scattering from energetically lower singlet trions (Fig. 5.7c). However, this process is energetically unfavourable and, thus, highly suppressed, leaving triplet trions highly valley polarized. In addition to these exchange-interaction mechanisms, intervalley scattering of charge carriers also can lead to valley depolarization. For positive trions, the small spin splitting of the conduction band allows ready scattering of electrons into the opposite valley (Fig. 5.7d), leading to fast depolarization [259]. For negative trions (triplet case in Fig. 5.7e), the large valence band splitting suppresses the hole scattering in between the valleys. Such scattering processes, then, will not contribute substantially to the valley depolarization of negative trions. The measured results described by these depolarization pictures confirm that the tuning of the chirality in the photonic interface is due to gate modification of the valley dynamics in monolayer TMDCs.

5.4 Driving valley(spin)-polarized exciton fluxes

In addition to enabling electrical control over chiral–directional coupling of the excitonic emission, the TMDC–waveguide interface opens new possibilities to locally create and manipulate excitons and spins. With improvements in sample quality and the observation of long-lived excitons in heterostructures, exciton diffusion in two-dimensional semiconductors has recently garnered increasing interest, providing a context for the fundamental exploration of planar spatial dynamics in systems with many-particle interactions [260, 261] and enabling optoelectronic technologies such as room-temperature excitonic transistors [112]. Unlike in bare, few-layer samples [219], the encapsulated TMDC monolayers in our interface provide reduced-disorder environments for studying exciton propagation [262] and preserve spin-valley locking, enabling the simultaneous transport of spin-polarized charge carriers.

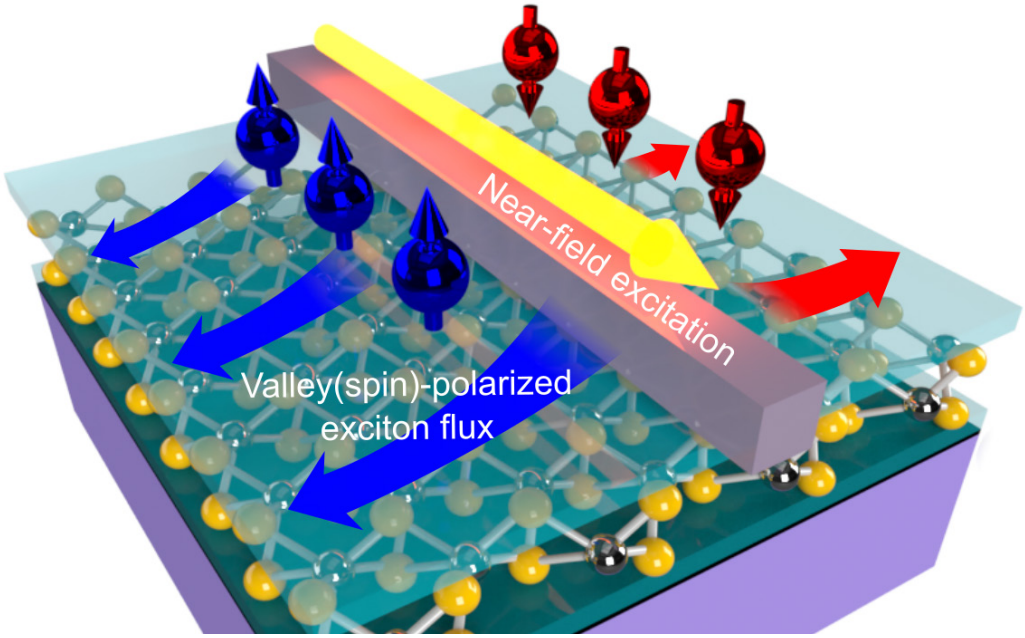

Figure 5.8: Schematic of valley(spin)-polarized exciton flux generation. Outward arrows (blue/red) indicate diffusion of oppositely valley-polarized excitons carrying spins for fixed propagation direction of the waveguide excitation mode (yellow).

Compared with the far-field optical excitations currently utilized to drive exciton diffusion, the waveguide modes of high-index nanophotonic structures can act as compact, tailored, on-chip sources of exciton fluxes. Moreover, the high DOCP of their evanescent fields enables the generation of valley-polarized exciton fluxes [263–265], which can be directionally reconfigured (Fig. 5.8). Therefore, a new modality for injecting spin currents in semiconductors with integrated photonics – in contrast to the case with conventional ferroelectric contacts [266, 267] – can be realized, promising advancements in optical computing and spintronics [268].

With our device, we first show that the waveguide can locally generate diffusive excitons. To probe this functionality, we couple the excitation laser into the right grating port and collect the PL emitted from the TMDC monolayer into the far-field. Figure 5.9 shows the spatial distribution of the exciton PL spectrally selected over the wavelength regions of interest (for representative spectra with peak identifications, see Fig. A.14). The shaded area

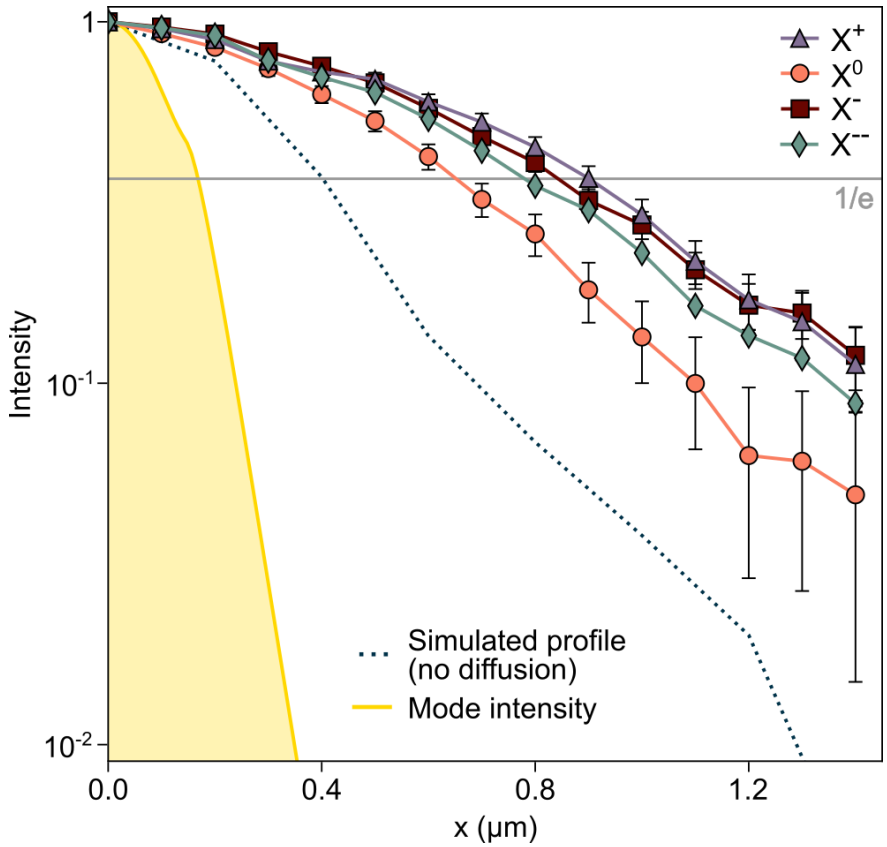

Figure 5.9: Exciton diffusion. Normalized PL intensity distributions versus distance from waveguide (center at $x = 0$μm) for different excitonic states. Shaded area is the simulated electric field intensity profile of the guided mode in the waveguide. Dashed line shows the simulated collection profile in the absence of diffusion given experimental resolution.

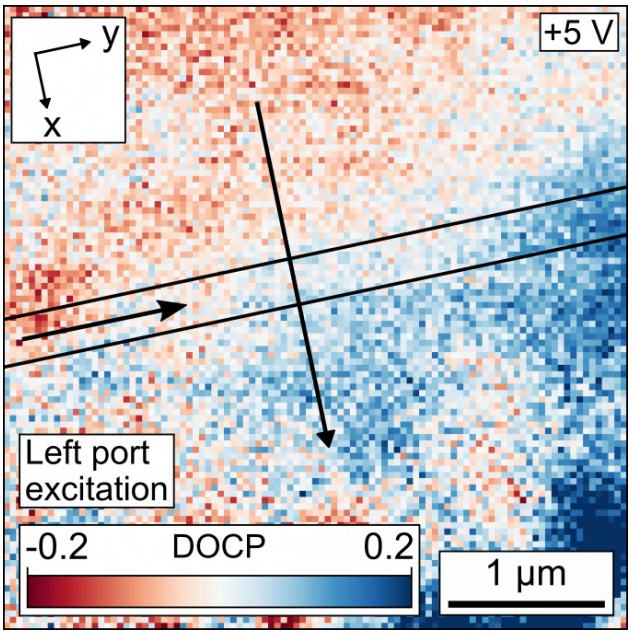

Figure 5.10: Spatial imaging of DOCP. DOCP map under 5 V gate bias, left port excitation, and far-field collection.

illustrates the simulated electric field intensity of the waveguide mode. The quickly decaying evanescent tail implies a large density gradient of the excitonic states generated by the mode, which induces their diffusive transport away from the waveguide. Considering the measured resolution of our collection channel (see Appendix A.2), we compute the anticipated PL spatial distribution in the absence of exciton diffusion (dotted line in Fig. 5.9; for simulation information see Appendix A.3). We find that the profiles of the excitonic states extend beyond this boundary, indicating their diffusion away from the waveguide. For the charged excitons, both negative and positive, we extract the 1/e diffusion lengths $L_{X^{\pm}} \simeq 0.45$ μm based on the predicted no-diffusion profile. The neutral exciton displays a diffusion length $L_{X^0} \simeq 0.25$ μm. These diffusion lengths of hundreds of nanometers are comparable to literature values [269] and may differ due to longer trion lifetimes. The excellent sample quality and comprehensive electrostatic control over our interface enable this extraction of state-specific diffusion.

We next examine the valley(spin)-polarization of these near-field-driven exciton fluxes.

As before, the evanescent fields on either side of the waveguide exhibit opposite nearly circular polarizations and therefore populate the excitonic states in opposite valleys (Fig. 5.8). To measure this resulting valley polarization, we analyse the circular polarization of the far-field PL. The valley polarization of the excitonic states is characterized by the PL DOCP. Here, $\mathrm{DOCP}(x,y) = (I_{FF}^{\sigma+}(x,y) - I_{FF}^{\sigma-}(x,y))/(I_{FF}^{\sigma+}(x,y) + I_{FF}^{\sigma-}(x,y))$, where $I_{FF}^{\sigma+(\sigma-)}(x,y)$ is the $\sigma+(\sigma-)$ component of the far-field PL intensity collected at position (x,y). Figure 5.10 shows the DOCP measured under left port excitation and 5 V gate bias, confirming the generation of valley-polarized excitonic states (for additional port and gate voltage results, see Figs. A.12 and A.13). Figure 5.11a–d displays the position-dependent, spectrally resolved DOCP for the respective X^+, X^0, X^- and X^{--} peaks, respectively. Like the CDCE (Fig. 5.5a–d) and far-field P_v (Fig. 5.6b) results, negative trions exhibit a large DOCP, whereas positive trions and neutral excitons show nearly zero DOCP. We also note the presence of prominent dark trion peaks at ∼750 nm [270] (Fig. A.14). Owing to their linear out-of-plane dipole moment [74], dark trions predominantly couple to the transverse magnetic mode, showing biased DOCP with a spatial profile that is independent of the excitation port. For negative trions, owing to valley–spin locking, the paired hole spin is fixed by the valley index (Fig. A.15). Thus, spin-polarized holes are injected with the valley-polarized X^- and X^{--} states. With the diffusion measurements described above, we conclude that our chiral photonic interface serves as a directionally reconfigurable source for injecting hole spin currents in atomically thin semiconductors.

5.5 Conclusion

We have demonstrated a photonic waveguide interfaced with an hBN-encapsulated, electrically gated WSe_2 monolayer. The interface exhibits a CDCE that is electrically tunable from 0% to 20% and generates valley(spin)-polarized exciton fluxes via near-field excitation. Beyond linear waveguides, our versatile nanophotonic fabrication method can interface

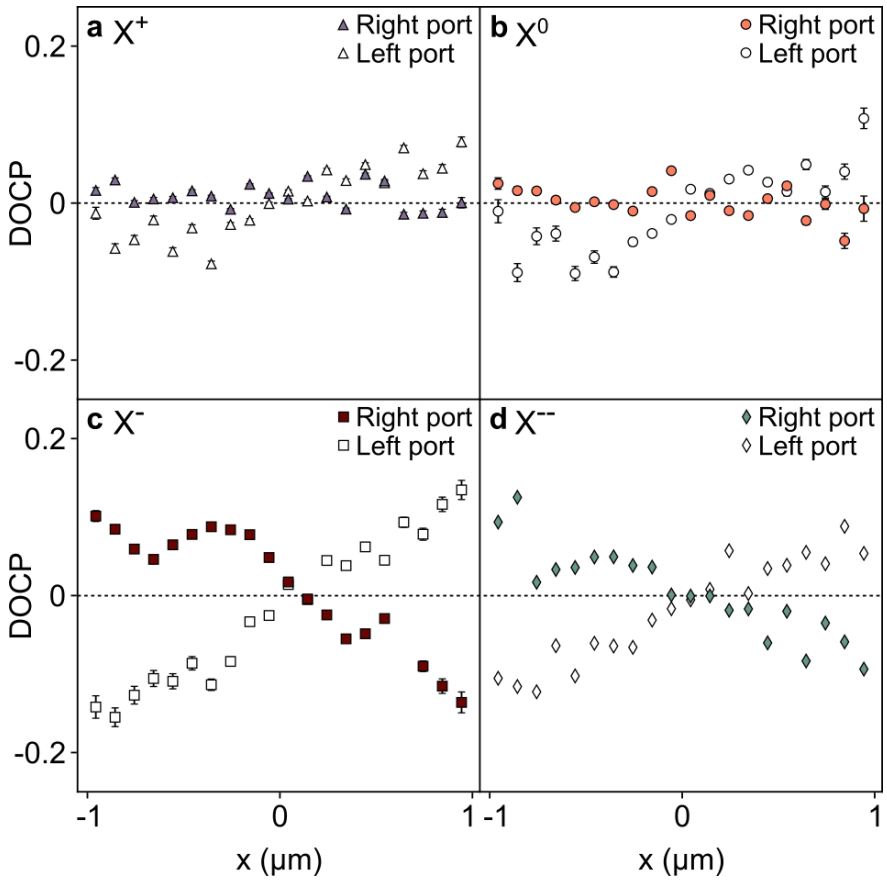

Figure 5.11: Valley-polarized exciton flux. Spatial distribution of DOCP for different excitonic states. Open (solid) circles correspond to rightward (leftward) propagating waveguide excitation in-coupled through the left (right) grating port. Data points are presented as mean values over the respective spectral ranges with error bars corresponding to 1SD of the background noise.

TMDCs with more complicated photonic structures where device geometry and size are limited only by the constraints of advanced lithography [246], enabling photonic ring modulators and inteferometers [271] and exciton–polaritons in photonic crystals [220]. Combined with recent advances in large-area growth [272], exfoliation [228, 273], and assembly [229] of two-dimensional materials, which will improve heterostructure yield and scalability beyond current limitations, this work establishes a universal platform for their deterministic, wafer-scale integration with nanophotonic circuitry. Importantly, this interface's tunable chirality, previously unavailable in other chiral optical interfaces, relies on the doping-dependent valley dynamics of exciton states in the TMDC monolayer. Multilayer and twisted van der Waals heterostructures display engineered, exotic valley properties [274–276] that can also be combined with this waveguide interface for additional chiral functionalities, such as gate-reversible emission routing [277], and offer new photonic logic and control schemes based on two-dimensional materials. In addition, nanophotonic driving of exciton diffusion in atomically thin semiconductors creates a bridge between distributed photonic elements and local excitonic circuits [111, 278, 279]. Moreover, near-field optical pumping through chiral TMDC–photonic interfaces can be used to generate the spin polarization of resident charge carriers in monolayers [96, 280]. Such optically prepared spin-polarized electronic states, which are sensitive to the carrier doping level, can break the time-reversal symmetry of the interface, enabling gate-activated all-optical non-reciprocity in integrated nanophotonic architectures [281].

CHAPTER 6

OPTICALLY STABILIZED MAGNETISM IN A 2D SEMICONDUCTOR

Adapted from: Kai Hao†, Robert Shreiner†, Andrew Kindseth, and Alexander A. High. Optically controllable magnetism in atomically thin semiconductors. *Science Advances* **8**, eabq765 (2022).

We report evidence that ferromagnetic order in electrostatically-doped, monolayer transition metal dichalcogenide (TMDC) semiconductors can be stabilized and controlled at zero magnetic field by local optical pumping. We use circular dichroism (CD) in reflectivity from excitonic states as a spatially-resolved probe of charge-carrier spin polarization. At electron densities $n_e \sim 10^{12}$ cm^{-2}, a diffraction-limited, circularly-polarized optical pump breaks symmetry between oppositely-polarized magnetic states and stabilizes long-range magnetic order, with carrier polarization exceeding 80% over an 8 µm by 5 µm extent. In time-resolved measurements with pulsed optical excitation, we observe that magnetic interactions amplify the initial pump-induced spin polarization by more than an order of magnitude. The optical control of magnetism with local optical pumps will unlock new spin and optical technologies and provide a versatile tool in the study of correlated phases in two-dimensional electron gases.

†. These authors contributed equally to this work.

6.1 Introduction

Interacting electrons in two-dimensional electron gases (2DEGs) can exhibit a remarkable variety of correlated phases including Wigner-crystals, Mott insulators, charge density waves, and magnetism [125, 134, 282–285]. Due to favorable material properties and tuning capabilities, TMDCs are a rapidly emerging platform for the study and manipulation of 2DEGs. The interaction strength is typically characterized by the dimensionless parameter $r_s \sim m/\varepsilon\sqrt{n}$, where ε is the permittivity, n is the electron density, and m is the effective mass. For free electrons in TMDCs, the combination of large effective mass $0.44\ m_0$ and reduced dielectric screening creates a Bohr-radius that is only slightly larger than the lattice constant, yielding rs values exceeding 20 at experimentally accessible densities of $10^{11} - 10^{12}$ cm^{-2} [28, 134–136]. As a result, the energy of Coulombic interactions can be appreciably larger than energies associated with phase-space filling, leading to collective ordering of electronic states dictated by long-range exchange interactions [101, 134, 137–143, 283–286]. In particular, exchange interactions are predicted to create a variety of spin- and valley-polarized itinerant magnetic phases [137, 139, 140].

Recently, experiments have shown that under applied magnetic fields and in certain doping regimes, electrons in molybdenum disulphide (MoS_2) and molybdenum diselenide ($MoSe_2$) exhibit magnetic order with near-complete spin-polarization far beyond the predictions of a simple thermal population model [101, 135, 136]. The spin polarization manifests as circular dichroism in reflectivity and photoluminescence measurements of the excitonic states and was initially attributed to either interaction-enhanced electronic g-factor (so-called giant paramagnetism) [101] or the emergence of ferromagnetic order [135, 136]. In the ferromagnetism model, the spin polarization is due to strong exchange interactions, which favor the formation of a spin-polarized state in both the K and K' valleys [135, 140]. Follow-up experiments demonstrated that the system transitions from a ferromagnetic to a paramagnetic phase with increased doping, suggesting direct electronic control over the electron-electron

interactions and correlated phases [136]. These studies present compelling evidence that the magnetic ordering is ferromagnetic in nature. However, no net magnetization or spin polarization was observed at zero applied magnetic field. This absence was attributed to fluctuating nanoscale domains and the lack of a global symmetry breaking mechanism [136].

Optical pumping is a conceivable mechanism for breaking the symmetry between equivalent spin configurations in TMDCs. Recent studies have shown that pumping individual monolayers or heterostructures of TMDCs with circularly polarized light can generate spin imbalances with microsecond-long relaxation times [96, 287]. For WSe_2 monolayers in the electron doped region, which is the main focus of this work, resident electrons can be dynamically spin/valley-polarized by continuous pumping with circular light [280]. Photo-generated electrons excited in a selected valley by the circularly polarized pump will preferentially relax to the opposite valley due to fast spin-conserving intervalley scattering. Additionally, the intravalley recombination of conduction electrons with photo-generated holes forming dark excitons can enhance the asymmetry of the valley populations [287]. The resulting spin-polarization is maintained in the presence of the continuous pump as these processes occur on timescales faster than the spin relaxation rate [280, 287]. Moreover, due to the relatively low free charge carrier densities $n \sim 10^{12}$ cm^{-2}, a significant population of resident carriers may be spin-polarized, potentially sufficient to break the symmetry between ground-state spin configurations and stabilize magnetic order in alignment with the pumped spins (see Appendix B.10).

6.2 Long-range spin polarization

Here, we study the impact of above-bandgap, circularly polarized optical pumping on hexagonal boron nitride (h-BN) encapsulated monolayers of WSe_2, showing evidence of optically stabilized, nonlocal magnetic order. The heterostructure layout and optical image of the sample D1 are presented in Figures 6.1a and 6.1b. The doping level in the monolayer can

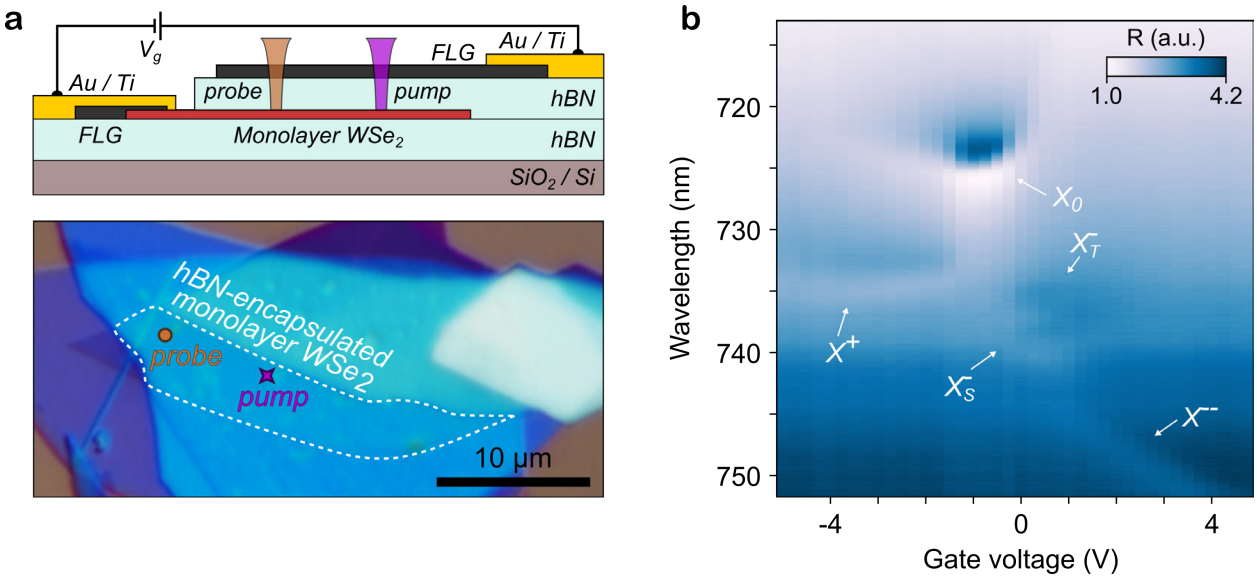

Figure 6.1: Sample under study. **a**, Schematic of hBN-encapsulated WSe_2 monolayer with few-layer graphene top gate and contacts. The optical pump and probe are spatially separated. **b**, Optical microscope image of sample D1. **c**, Gate dependent reflection spectra of the WSe_2 sample. The excitonic resonance features are labeled correspondingly.

be controlled by applying gate voltage between the few-layer graphene contact and top gate and manifests in the appearance of neutral and charged excitonic resonances in the reflection spectra, Figure 6.1c. We first focus on low temperature measurements at T = 4 K within the moderately electron-doped region, where bound singlet (X_S^-) and triplet (X_T^-) trions are clearly observed [67, 253, 257, 258, 288–290]. Reflection from a circularly polarized supercontinuum laser provides a probe of the local, valley-selective optical response. In the absence of pumping, balanced reflection of $\sigma+$ and $\sigma-$ polarized light is observed (Fig. 6.2a). Next, we pump the sample with a 660 nm diffraction-limited continuous wave (CW) laser with a sub-micron spot size and a power of 7.8 µW. To demonstrate the nonlocality of pump-induced effects and to eliminate the influence of photoluminescence in detection, the probe spot is separated by nearly 8 µm from the pump (Fig. 6.1b). The reflection spectra under $\sigma+$ polarized pumping are markedly different – the triplet (singlet) trion dominates the probe signal co(cross)-polarized to the pump (Fig. 6.2b). This pump-induced circular dichroism is characterized by $CD = \Delta R^+ - \Delta R^-$, where $\Delta R^{+,-} = (R_{on}^{+,-}/R_{off}^{+,-}) - 1$ is

the differential reflectivity comparing the $\sigma+,-$ probed reflection in the presence ($R_{on}^{+;-}$) and absence ($R_{off}^{+;-}$) of the pump. The CD signal displays amplitudes approaching 10% and inverts with the sign of the pump polarization (Fig. 6.2c).

Circular dichroism is a direct signature of electron spin/valley-polarization and has been utilized to study spin imbalances in a range of materials and doping regimes [96, 101, 135, 291–293]. Here, CD emerges at moderate carrier densities when singlet and triplet trions (or, valley-resolved attractive polarons) preferentially form in opposite valleys (see Fig. 6.2b inset). We analyze their valley-dependent oscillator strengths to quantify the spin polarization (see Appendix B.4). Since the valley-dependent charge density correlates with the oscillator strength of the transition [84, 294], we estimate that 90% (10%) of charges reside in the valley cross(co)-polarized with the pump even at 8 µm pump-probe separation. This corresponds to a spin polarization $P_s = 0.77$, where $Ps = (A^+ - A^-)/(A^+ + A^-)$ and $^A+,-$ is the probe-polarization-selective oscillator strength of the trion state under optical pumping. For an electron doping density of $n \approx 1.8 \times 10^{12}$ cm^{-2} (Fig. B.3), this yields an estimated spin population imbalance of $\sim 1.4 \times 10^4$ µm^{-2}.

Remarkably, the optical pump generates a near-complete free carrier spin polarization that persists micrometers away from the pump location. We next study this spatial dependence in more detail. Figure 6.3a shows a photoluminescence (PL) map of the region of interest (ROI) of the monolayer flake. The central dark area corresponds to a bilayer region. Mapping the CD signal across the entirety of the ROI, Figure 6.3b depicts the CD associated with the singlet trion peak as the probe is scanned across the flake while the $\sigma+$ pump remains fixed. CD is clearly observed within the pristine portion of the ROI, except for in the bilayer region where no resonance peak nor CD signal are found. When the sign of the pump polarization is flipped to $\sigma-$ (Fig. 6.3c), the CD signal inverts everywhere. The spatial inhomogeneity of the sample is depicted in Figure 6.3d. The trion resonance energy varies by up to 30 meV within the ROI, which is typical even in high quality heterostructures

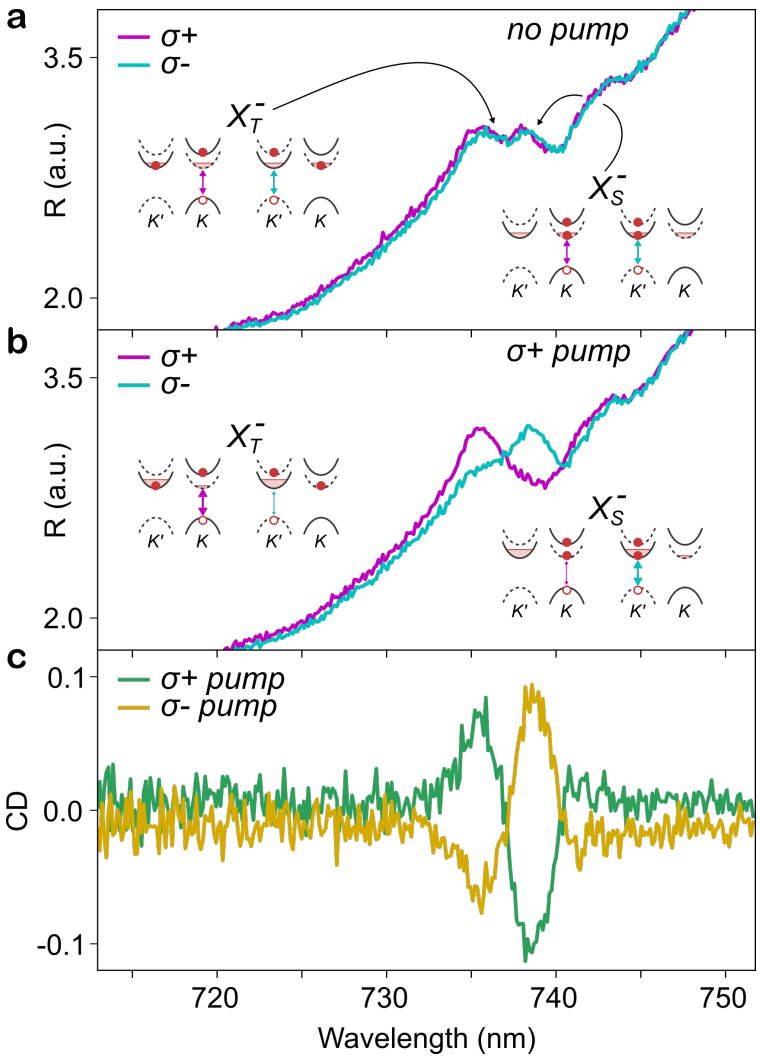

Figure 6.2: Circular dichroism. **a**, $\sigma+$ and $\sigma-$ reflection spectra at 0.5 V, where the singlet and triplet trion features are well resolved. Inset: Singlet and triplet trion configurations showing balanced valley populations. Solid and dashed bands indicate spin ordering. **b**, $\sigma+$ and $\sigma-$ reflection spectra at 0.5 V ($n_e \approx 2 \times 10^{12}\text{cm}^{-2}$) under $\sigma+$ pumping. Insert: Schematic of singlet and triplet trion in optically pumped spin/valley-polarized electron bath. **c**, Circular dichroism (CD) spectra under $\sigma+$ and $\sigma-$ pumping. Note: T = 4 K, pump power is 7.8 µW, and pump-probe offset is 8 µm.

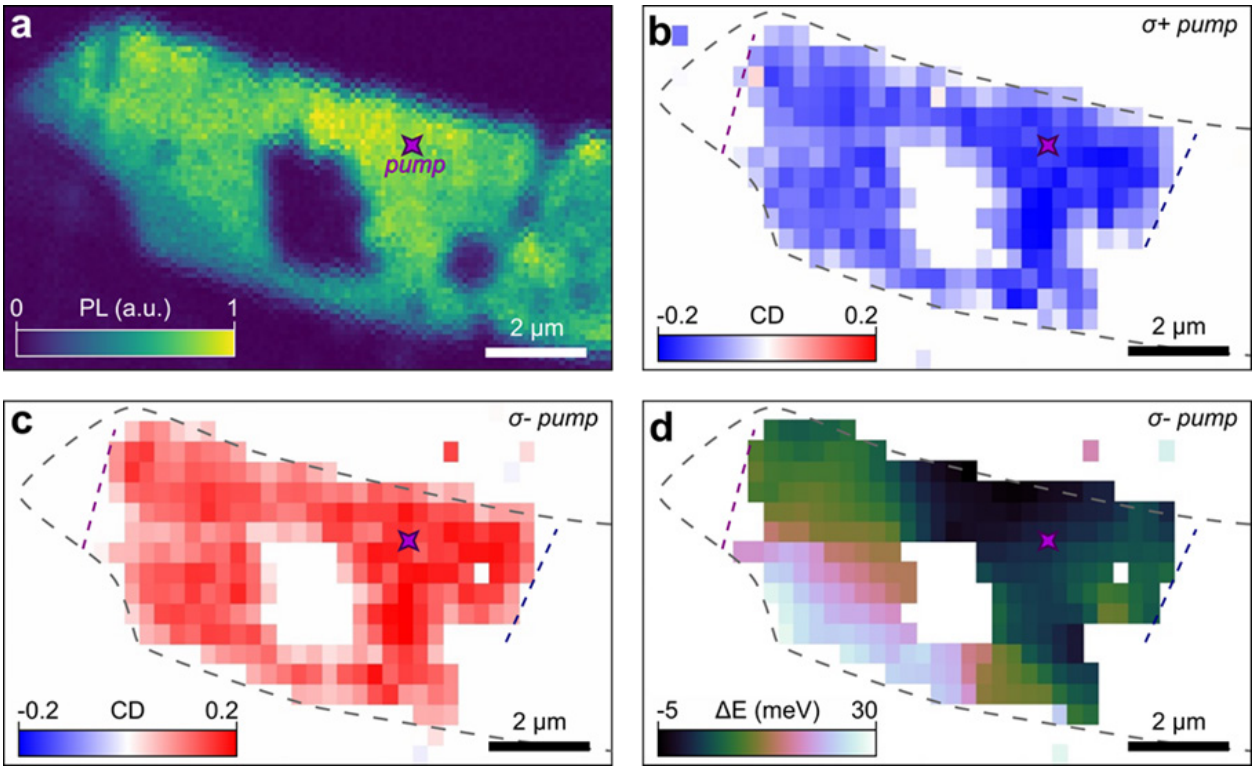

Figure 6.3: Spatial profile of the spin polarization. **a**, Sample D1: Photoluminescence (PL) map of the ROI. **b,c**, Map of the CD amplitude across the whole ROI under $\sigma+$(**b**) and $\sigma-$(**c**) pumping located at star in (**a**). **d**, Map of peak energy shifts of the singlet CD signal compared to the value at the pump location. Purple and blue dashed lines correspond to wrinkles on the sample. Note: T = 4 K, pump power is 7.8 μW, and gate voltage is 0.5 V ($n_e \approx 2 \times 10^{12}\text{cm}^{-2}$).

[295], while the CD signal is still robust. However, more prominent imperfections apparently destroy the spin polarization. The purple and blue dashed lines indicate wrinkles and residue in the heterostructure observed under microscope imaging, which correspond to observable dips in photoluminescence (Fig. 6.3a). The CD signal terminates upon crossing the noted defects.

6.3 Spin polarization dynamics

We also investigate the temporal dynamics of the spin polarization with different pump/probe separations (on a second sample D2). We use a local, 5 ns pulsed laser at 633 nm to

generate a spin imbalance under the pump and then measure spatially- and temporally-resolved changes to the spin polarization extracted from differential reflection (see Appendix B.5). We observe that as the system evolves in time, mesoscopic spin polarization emerges at micron length scales over a microsecond timescale (Fig. 6.4a). The peak spin polarization observed exhibits no systematic change with increasing pump/probe separation (Fig. 6.4b, red squares), agreeing with the spatially uniform CD under CW pumping (Fig. 6.3). The spin polarization at the pump location sets an upper bound for the optical spin polarization injection. After building up for hundreds of nanoseconds, the spin polarization detected away from the pump location exceeds that observed at the pump location. These results cannot be captured by a two-dimensional diffusion-decay model with pulsed excitation, which predicts at least an order of magnitude decay in polarization at three-micron separation regardless of the parameter estimates used for the carrier diffusion constant and relaxation time [264] (see Appendix B.5). These results indicate that after the spin injection from the initial excitation pulse, the spin polarization is appreciably amplified across the sample and persists for over 10 µs (Fig. 6.4c).

6.4 Doping, power, and temperature dependence of spin polarization

To gain further insight into the origin of the mesoscopic spin order, we vary the doping concentration. We observe that the macroscopic spin polarization strongly depends on electron density and vanishes above a threshold $n_c \approx 4 \times 10^{12}$ cm^{-2}. As depicted in Figure 6.1c, we can access the intrinsic, hole-doped and highly electron-doped region by varying the gate voltage. Here, we study the long-range CD (*i.e.*, pump-probe separation of 8 µm, Fig. 6.1b) within these different doping regions, where excitonic resonances are sensitive to underlying spin polarization [96, 101, 135, 291–293]. As shown in Figure 6.5a, no CD signal is observed in the intrinsic region, where the neutral exciton resonance is clearly observed in

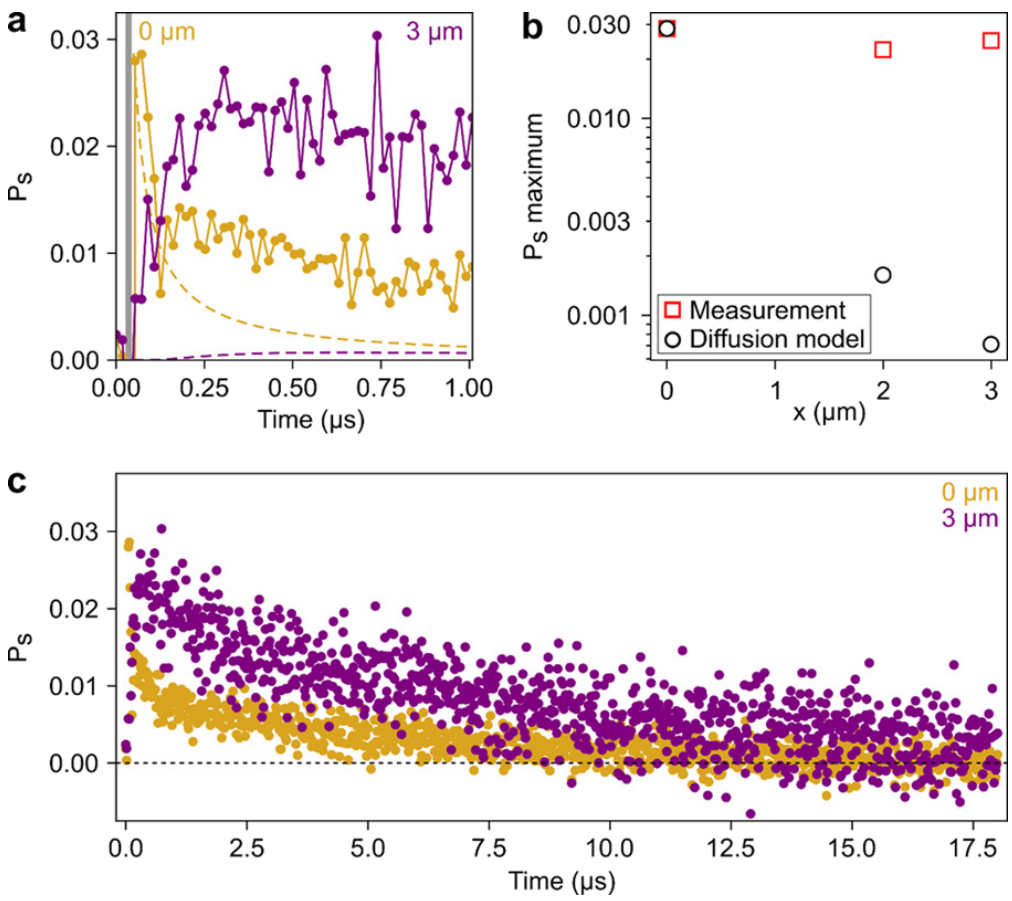

Figure 6.4: Spin polarization dynamics. **a**, Sample D2: Time-resolved spin polarization extracted from changes in reflection probed overlapping (yellow) and 3 µm (purple) from a pulsed circular pump with average power of 2 nW at a repetition rate of 50 kHz. Grey bar corresponds to the window of the pulsed pump. Dashed lines indicate the predicted profiles of a diffusion-decay model. **b**, Comparison of the maximum spin polarization as a function of pump-probe offset between the measured values and the simulated values of the diffusion-decay model. **c**, Extended dynamics of the time-resolved spin polarization. Note: T = 4 K and gate voltage is 0.5 V ($n_e \approx 2 \times 10^{12}\text{cm}^{-2}$).

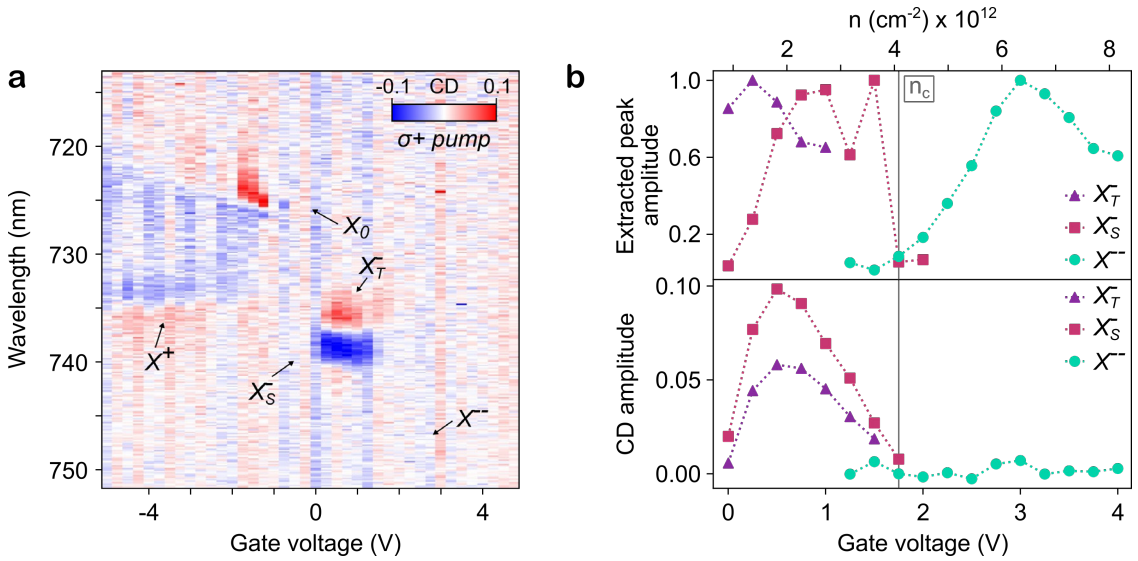

Figure 6.5: Gate dependence of spin polarization. **a**, Sample D1: Gate-dependent CD spectra probed 8 µm from the pump (Fig. 6.1b) under $\sigma+$ pumping. Excitonic states are labeled corresponding to the features in reflection spectra. **b**, Peak amplitude and CD amplitude extracted from (**a**) versus gate voltage (doping level). The critical electron density n_c is indicated. Note: Unless indicated otherwise, T = 4 K and pump power is 7.8 µW.

reflection, implying the optically induced CD is correlated with free carriers in the system. As in Figure 6.2c, we observe strong CD co(cross)-polarized to the pump from the triplet (singlet) features. At higher doping concentrations, while the heavily-doped charged exciton X^{--} [293, 296] is clearly observed in reflectivity, there is no observable CD. We further characterize this by plotting the extracted peak and CD amplitudes (Fig. 6.5b) against the estimated doping density for different species of excitonic states. We observe that at 1.75 V, $n_c \approx 4 \times 10^{12}$ cm^{-2}, where the Fermi energy is still within the spin-orbit gap in the conduction band [291], the system transitions from observable singlet and triplet trions with strong CD, to X^{--} exciton states with no observable CD. As the X^{--} exciton states are sensitive to spin polarization of the free carriers [135, 291, 293], the disappearance of CD in this doping regime indicates the free carriers are unpolarized, agreeing with previously reported first-order phase transitions in MoS_2 [136]. We also observe CD signal from the positive trion X^+ in the hole-doped regime.

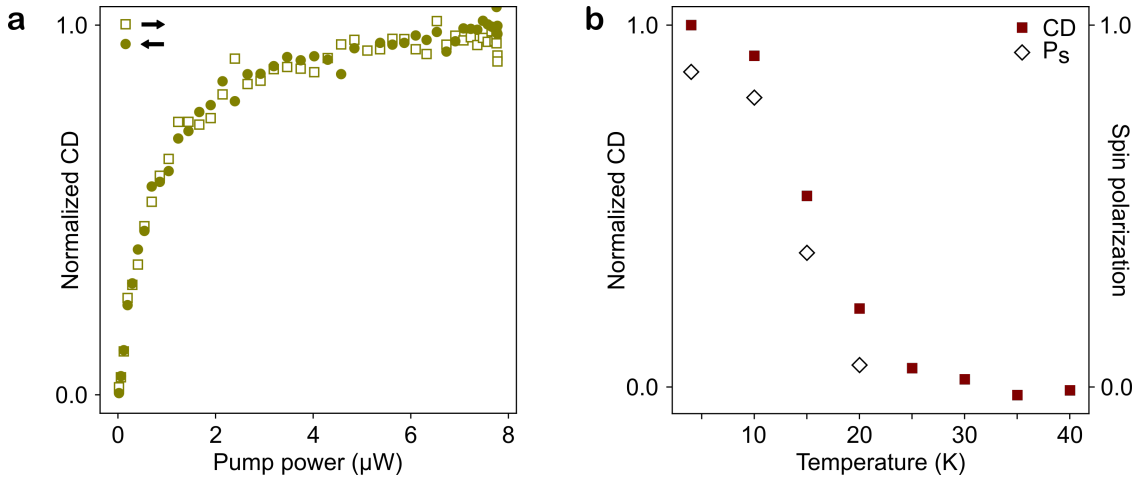

Figure 6.6: Pump power and temperature dependence of spin polarization. **a**, Sample D1: Power dependence of CD amplitude with pump-probe separation of 1.6 µm and gate voltage of 0.5 V ($n_e \approx 2 \times 10^{12}\text{cm}^{-2}$). Hollow squares (solid circles) correspond to increasing (decreasing) pump power. **b**, Sample D3: Temperature dependence of CD amplitude (red squares) with pump-probe separation of 2.2 µm and gate voltage of 1.2 V ($n_e \approx 2.8 \times 10^{12}\text{cm}^{-2}$). Corresponding spin polarizations (hollow diamond) are extracted from reflection spectra. Note: Unless indicated otherwise, T = 4 K and pump power is 7.8 µW.

Lastly, we investigate the spin polarization with respect to changes in pumping power and temperature (on a third sample D3). Long range spin polarization is generated with sub-µW pumping power and saturates quickly without displaying hysteresis effects (Fig. 6.6a). Figure 6.6b depicts the temperature dependence of the CD signal and calculated spin polarization. The CD signal vanishes at T = 30 K, even though reflection spectra still exhibit clear resonance features of singlet/triplet trions and X^{--} states (Fig. B.8). The rapid transition from an unpolarized ($Ps = 0.06$) to a polarized ($Ps = 0.87$) spin state as the temperature goes below T = 15 K evidences a phase transition.

6.5 Discussion

The key finding of this work is the optical generation of mesoscopic spin polarization in a TMDC monolayer. A possible explanation for long-range spin polarization is diffusion

of optically pumped resident carriers. In such a non-interacting spin diffusion picture, the spatial spread of an initial, conserved spin imbalance would yield a rapid decay in the maximum spin polarization away from the pump region. Our time-resolved measurements show a uniform maximum spin polarization microns away from the location of the pulsed pump. The corresponding excess of polarized spins – forty times larger than predicted by diffusion – necessitates interaction-driven amplification. Additionally, the complete disappearance of long-range spin polarization with small changes in carrier density is inconsistent with non-interacting models. Furthermore, in a diffusion model, reduction of spin lifetime with increased doping or temperature [96] could eventually quench the spin polarization, leading to shorter diffusion lengths and a spatial contraction in the CD profile. Such spatial contraction predicted by the diffusion model is not observed (Fig. B.10). In both the CW and pulsed pump measurements, the observed spin polarization behavior requires electron-electron interactions absent from a diffusion model.

However, our results show excellent agreement with recent theoretical and experimental work on magnetism in monolayer TMDCs. In theoretical models of electron-electron interactions in TMDCs [137–143], exchange inter- and intra-valley coupling lead to spin-polarized ferromagnetic phases at electron densities around $n_e \sim 10^{12}$ cm^{-2}. These models were validated by experimental studies of magnetic phases in electron-doped monolayer molybdenum disulphide (MoS_2) in an external magnetic field. In that case, strong exchange intervalley interactions – compared to the small spin-orbit splitting of the conduction bands in MoS_2 – lead to band inversion and the spin polarization of resident electrons across both K and K' valleys (*i.e.*, spin-polarized, but not valley-polarized electrons) [135, 140]. In contrast, WSe_2 monolayers exhibit an order of magnitude larger spin-orbit splitting in the conduction band [137]. The Fermi level in the electron-doped regime remains within this spin-orbit gap [291], implying that only the bottom two conduction bands are occupied by resident electrons. Consequently, the predicted ferromagnetic ground state consists of spin/valley-polarized res-

ident electrons [137], in agreement with our circular dichroism results. Moreover, the sudden disappearance of spin polarization with increased electron doping is consistent with a phase transition from a ferromagnetic to a paramagnetic phase, as found in previous experimental [136] and theoretical studies [137–143] of magnetic phase transitions in TMDCs. This phase transition was interpreted to be first-order [136]. As in these previous studies [135, 136], the magnetic phase transition in our data is accompanied by a sudden transition from trion states to X^{--} states. While the nature of this excitonic transition remains an ongoing topic of research – having been associated with abrupt changes in the internal correlations of the exitonic states [293] and in the electron effective mass [136] – its sharpness suggests a first-order transition. However, the CD magnitude does not show a distinct discontinuity, making it challenging to definitively conclude the order of the magnetic phase transition. Indeed, recent theory work has found that the transition may be first- or second-order depending on the interaction strength [142]. A transition also is observed in the temperature dependence of the CD signal, which represents the magnetization [297], displaying a trend qualitatively similar to other 2D ferromagnetic materials [298]. Criticality fits indicate a Curie temperature $T_c = 15$ K with a critical exponent of 0.113, close to the value of 0.125 for a 2D Ising model [299] (Fig. B.8). The consistency of our results with these ferromagnetic models suggests that the mesoscopic spin polarization is associated with ferromagnetic order in the monolayer TMDC.

An exact microscopic description of the ferromagnetic state and its optical control remain topics of ongoing interest. Current proposals picture a ground state of fluctuating, nanometer-scale ferromagnetic domains, which, averaged over space and time, show no net magnetization [136, 142]. The circularly polarized optical pump stabilizes the magnetic state against fluctuations by selectively valley-pumping spin-polarized electrons, thereby breaking the symmetry between degenerate magnetic states and preferentially favoring the formation of a co-polarized magnetic state. This mechanism is also fundamentally different from

previously reported all-optical control of magnetism, which is based on heating and inverse Faraday effects [300–303]. Further, while the optical pump acts locally, the magnetic order is stabilized mesoscopically, extending well beyond the sub-micron pumping region to the boundaries of the monolayer. Recent theoretical works have argued that spin-injection into an unstable, symmetric ferromagnetic state can yield spin amplification, similar to our observations [304]. Continued theoretical and experimental study is needed to better understand the microscopic nature of this itinerant ferromagnetism and its stabilization by light.

6.6 Doping evolution of spin polarization dynamics

In particular, more comprehensive study of the spin polarization dynamics may provide insight into the mechanisms governing the spread and stabilization of the magnetic order. As a first step, we performed time-resolved measurements at various doping concentrations on an additional sample D5 (Fig. 6.7). The range of electron doping spans the density regime where circular dichroism is observed under CW pumping. Surprisingly, while the temporal profiles of the differential reflection are identical at moderate electron doping ($n = 2.73 \times 10^{12}$ cm^{-2}), the offset signal disappears at low electron doping ($n \approx 1 \times 10^{12}$ cm^{-2}), even though it still appears in CW measurements (Fig. B.12). The emergence of offset signal from $n = 1.15 \times 10^{12}$ cm^{-2} to $n = 1.52 \times 10^{12}$ cm^{-2} coincides with a narrowing of the overlapped signal. Above $n = 1.52 \times 10^{12}$ cm^{-2}, the offset signal varies little, while the sharp initial decay in the overlapped signal recedes into the slower decay profile shared with the offset signal.

The transition revealed by the offset data at low doping density suggests a rapid change in the mobility of the electrons. We conjecture that this may originate from a phase transition from a ferromagnetic Wigner crystal to a ferromagnetic electron liquid. Wigner crystals have been reported in dilute electron gases ($n_e \approx 1 \times 10^{11}$ cm^{-2}) in $MoSe_2$ [134] and are suggested to have a ferromagnetic ground state [125, 305, 306]. In the insulating Wigner

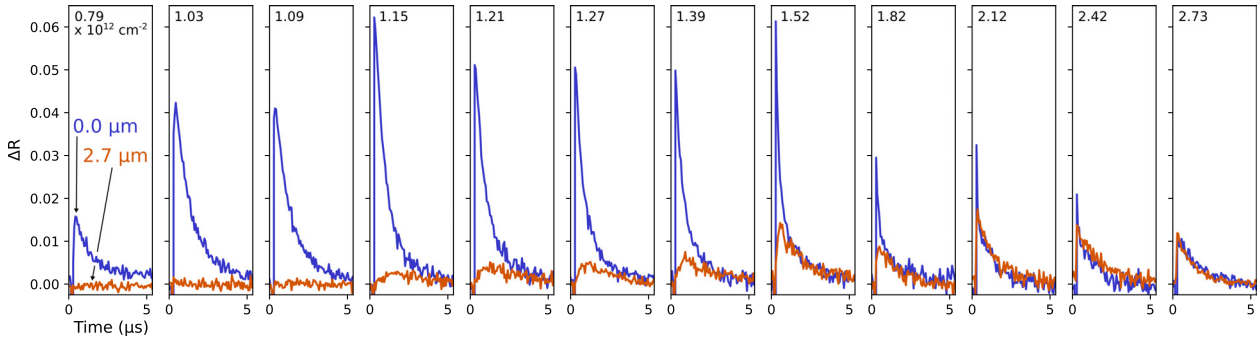

Figure 6.7: Doping dependence of spin polarization dynamics.

crystal state, the spatial correlation of electrons inhibits the propagation of injected spin-polarized carriers. As the density increases, and so the interaction strength decreases, the Wigner crystal melts and the injected spins are "released." The offset signal appears as the injected spin carriers propagate to the probe position. Within the density regime $n = 1.15 \times 10^{12}$ cm^{-2} to $n = 1.52 \times 10^{12}$ cm^{-2}, the relative profiles of the overlapped and offset signals look similar to the diffusion model, suggesting domain alignment to diffusing carriers may dominate here. However, as the electron density increases further, the overlapped signal shows two distinct decays. The narrow, short-time decay may be associated with the diffusion process. As the density is elevated, the ratio of injected to resident carriers decreases, and so the relative weight of the fast decay decreases. The slow, long-time decay may be due to cooperative domain alignment of the resident carriers and the "drag" of interaction-driven stabilization as the domains relax to the fractured ground state. Additional measurements of the temperature dependence, as well as direct observation of the Wigner crystal, may provide further clues.

6.7 Conclusion

We present evidence for optically controllable ferromagnetic order in TMDCs. The recent discovery of magnetic 2D materials has generated significant excitement due to their novel integration and heterostructure possibilities [307–309]. Our research establishes TMDCs as

a 2D magnetic material, albeit with very different physics and properties than more conventional 2D magnets – the magnetism originates from strongly correlated itinerant electrons, and critically, the magnetic configuration can be fully tuned non-locally with optical fields and electronic gating. Moreover, the local optical pump stabilizes the magnetic state, even at low sub-microwatt power, providing finer spatial resolution for the study and control of magnetic domain structure. These unique features open new avenues for probing the previously inaccessible physics of magnetic order in two-dimensional semiconductors, prompting future experimental investigations of the temporal dynamics with ultrafast spectroscopy [310] and spatial formation of domains with NV magnetic sensors [311–313] and Lorentz TEM [314] under optical pumping. Additionally, TMDCs are a prototypical platform for explorations of correlated phenomena in 2DEGs, and we show that optical pumps provide a powerful tool for understanding and controlling these systems. For instance, magnetic phases and their circular dichroism could be utilized to manipulate and probe Mott insulators and Wigner crystals [134, 283, 284].

Furthermore, our findings will accelerate technological developments utilizing TMDCs, already a leading material platform for investigating next-generation spin-, valley-, and optoelectronics [206, 207, 315, 316]. Specifically, the discovery of optically reconfigurable magnetism and circular dichroism in atomically thin semiconductors will stimulate the design of non-reciprocal optoelectronics and photonics [317, 318], such as on-chip all-optical isolators with built-in optical memory. Additionally, spin amplification enables fan-out, a necessary element in envisioned spintronic circuits [304]. Our research indicates that magnetic phases in TMDCs can fulfill this amplification criteria. Lastly, our research creates a bridge between magnetism and optical control in TMDCs, which can be leveraged for direct interfacing between integrated photonics and magnetic solid-state memories [303], suggesting new routes for neuromorphic optical computing [319].

CHAPTER 7

TOWARDS AN INTEGRATED, ALL-OPTICAL ISOLATOR

7.1 Integrated optical isolators

Optical isolators permit the flow of light in one direction and preclude it in the opposite [320]. Such "photonic diodes" are useful for preventing unwelcome back-reflections in laser systems and routing light in optical communication networks. On-chip optical isolators, however, have proved difficult to make due to lingering material and device challenges. The conventional approach to breaking Lorentz reciprocity [321, 322] relies on monolithic integration of thin film magneto-optical rare earth iron garnets with photonic structures (Fig. 7.1) [318, 323, 324]. Under external magnetic bias, the dielectric permittivity tensor of the magneto-optical film has a non-zero diagonal element proportional to the Faraday rotation, which introduces non-reciprocal phase shifts to the propagating photonic modes and can drive non-reciprocal mode conversion. High quality deposition of such garnets is difficult to achieve and their processing has poor compatibility with standard foundry techniques. Additionally, the external magnetic bias limits possibilities for hybrid device architectures [325].

Recent years have seen much creative work on devising alternative non-reciprocal device schemes for "magnet-free" optical isolators [326]. Two popular approaches utilize temporal modulation of the refractive index [327–338] and optical nonlinearity [339–345]. While impressive isolation performance has been demonstrated (Table 7.1), some limiting factors hinder large-scale implementation. Particularly for the time-modulated systems, the use of active radiofrequency/acoustic driving demands complex device geometries – and so challenging fabrication – and results in large power consumption. While the nonlinear optical isolators are admirably passive, they operate at large signal powers $\sim 10 - 100$ mW. Notably, while not on-chip and requiring either large optical drives or external magnetic bias,

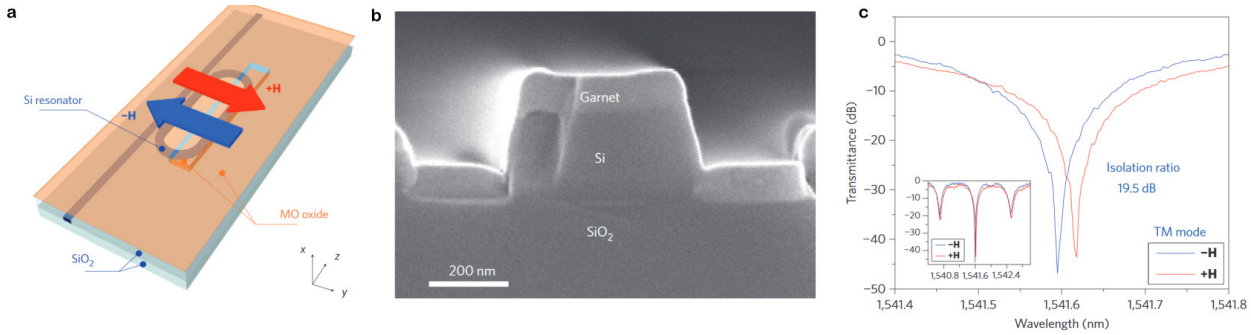

Figure 7.1: Magneto-optical on-chip isolator. Schematic (**a**) and cross-sectional SEM image (**b**) of magneto-optical garnet integrated with a photonic ring resonator. **c**, Under opposite magnetic bias, the transmission features shift, simulating isolation of nearly 20 dB. Figure adapted from source [318].

Year	Material	Isolation	Insertion loss	Bandwidth	Power
2020 [343]	Si	20 dB	1.3 dB	20 GHz	–
2014 [333]	Doped Si	2.4 dB	–	2.4 THz	34 dBm
2021 [347]	AlN	3 dB	9 dB	4 GHz	16 dBm
2021 [348]	Doped Si	13 dB	1 dB	2 GHz	-3 dBm
2012 [331]	Doped Si	3 dB	70 dB	200 GHz	25 dBm
2018 [336]	Si	39 dB	–	125 GHz	20 dBm
2018 [337]	AlN	15 dB	–	1 GHz	18 dBm
2021 [338]	Si + AlN	16 dB	–	100 GHz	21 dBm
2022 [328]	Si_3N_4 + AlN	10 dB	1 dB	0.7 GHz	25 dBm
This proposal	WSe_2	11 dB	6 dB	250 GHz	-30 dBm

Table 7.1: Magnet-free, on-chip optical isolators. A comparison of figures of merit from recent demonstrations of integrated, magnet-free optical isolators. Adapted from [328].

atomic ensembles have demonstrated isolation of optical signals at the microwatt [346] and single-photon level [196, 197].

Here, we have an optically controllable magnetic material – monolayer WSe_2 – which can be interfaced simply with nanophotonics. Optical spin-orbit coupling at the chiral nanophotonic interface maps the circular dichroism of the spin-polarized monolayer onto the propagation direction of the waveguide mode, breaking optical reciprocity [349]. No external magnetic bias is needed, as the magnetic order is generated *in situ* with microwatt power optical pumps, enabling the design of a low power, all-optical integrated isolator.

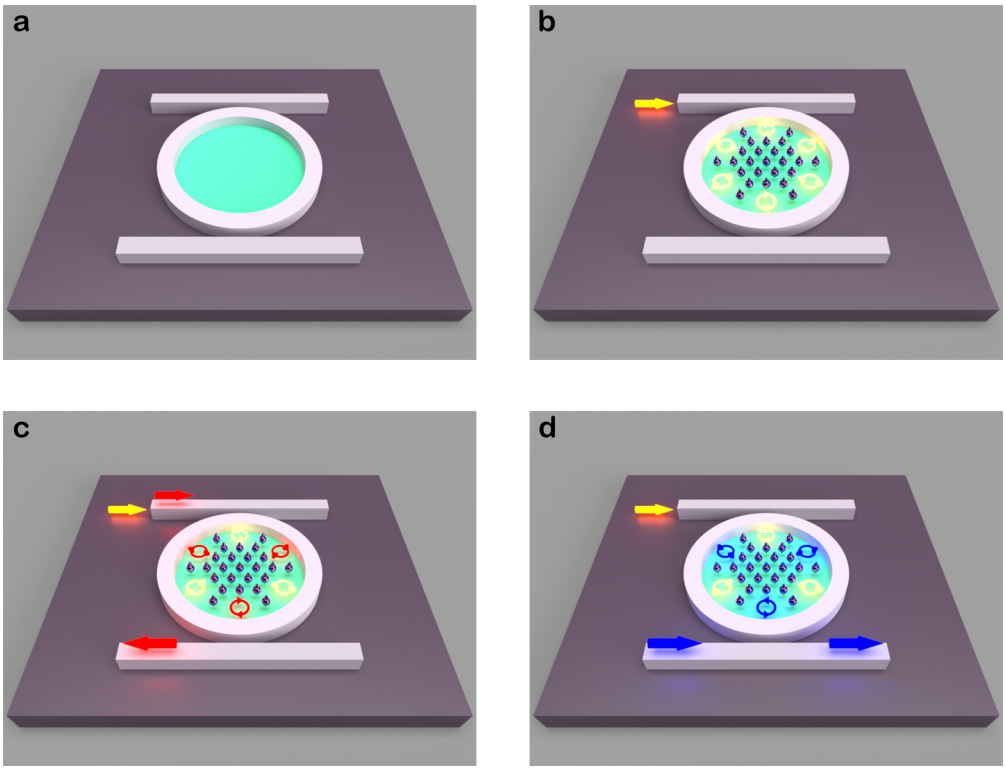

Figure 7.2: TMDC-based isolator. **a**, The chiral TMDC-nanophotonic interface is implemented in a ring resonator geometry (monolayer in green). **b**, Due to optical spin-orbit coupling in the evanescent field, a pump (yellow) generates spin polarization in the monolayer. The resulting circular dichroism modifies the transmission of co-propagating, forward (**c**) and counter-propagating, backward (**d**) modes.

7.2 TMDC monolayers for chiral nanophotonic isolation

The proposed isolator scheme is illustrated in Figure 7.2. A ring resonator structure is interfaced with a WSe_2 monolayer. Optical spin-orbit coupling locks the circular polarization of the evanescent field of the circulating resonator modes to their propagation direction. A pump mode generates spin polarization in the monolayer. Due to the resulting circular dichroism, subsequent probes show contrasting transmission depending on whether they co-propagate or counter-propagate with the pump.

The transmission response of the ring resonator device is determined by three parameters: the phase constant $\beta = 2\pi n_{eff}/\lambda$, which fixes the resonance location; the attenuation constant $\alpha = 2\pi k_{eff}/\lambda$, which reduces the transmitted power; and the waveguide self-coupling

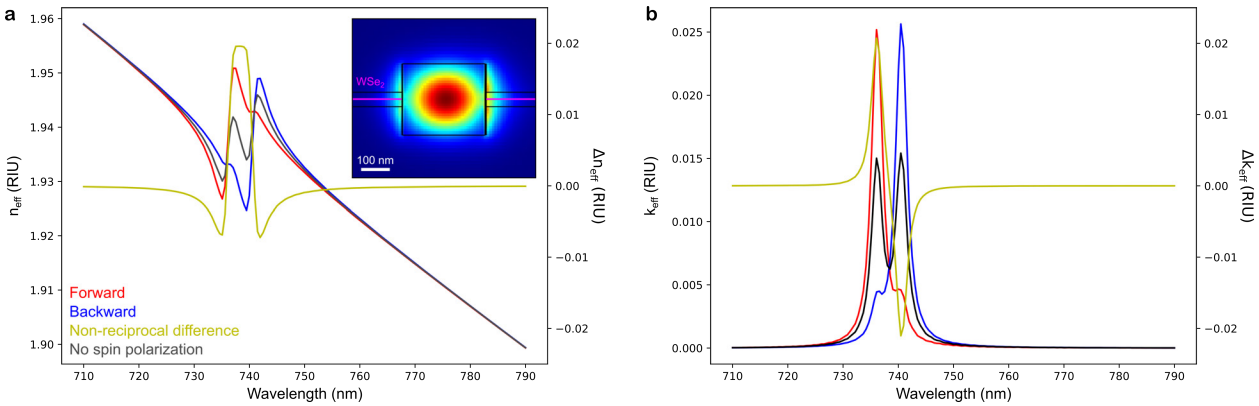

Figure 7.3: Non-reciprocal effective index. Real (**a**) and imaginary (**b**) effective indices of forward and backward modes given a spin polarization $P_s = 0.8$. Inset: cross-section of the simulated mode profile with the monolayer shown in pink.

constant τ, which influences the resonance width [350]. The complex effective mode index $n_{eff} + ik_{eff}$ is modified by the WSe_2 monolayer, and thus becomes non-reciprocal in the presence of spin polarization. The monolayer optical response can be modeled as a two-dimensional sheet with conductivity $\sigma_{\pm}(\nu) = ic\varepsilon_0(\frac{\gamma_r(1+P_s)}{\nu-\nu_1+i\gamma_{nr}/2} + \frac{\gamma_r(1-P_s)}{\nu-\nu_2+i\gamma_{nr}/2})$ [87], where $\nu_{1,2}$ correspond to the triplet and singlet trion resonances with radiative and non-radiative linewidths of $\gamma_r = 1$ meV and $\gamma_{nr} = 5$meV in the presence of a spin polarized Fermi sea $P_s = 0.8$. Using Ansys Lumerical's MODE solver, the effective indices of the TE-like forward ($P_s = +0.8$) and backward ($P_s = -0.8$) propagating modes are computed (Fig. 7.3). Here, the monolayer is positioned at the vertical center and on both sides of the waveguide to enhance the index contrast, which is on the order of 10^{-3} near the trion features, suitable for modulating transmission [271].

Without the WSe_2 monolayer, drop transmission is simulated for a 5 µm radius ring with cavity quality factors on the order of 1,000 (Fig. 7.4a), which are attainable with our TiO_2 photonics platform (Fig. 4.5a). Absorption losses introduced by the WSe_2 monolayer lead to undercoupling to cavity modes near the trion resonances, quenching their transmission (Fig. 7.4b). Nearby, the circular dichroism of the spin polarized WSe_2 shifts the relative energy and amplitude of transmission of forward and backward propagating modes, reaching

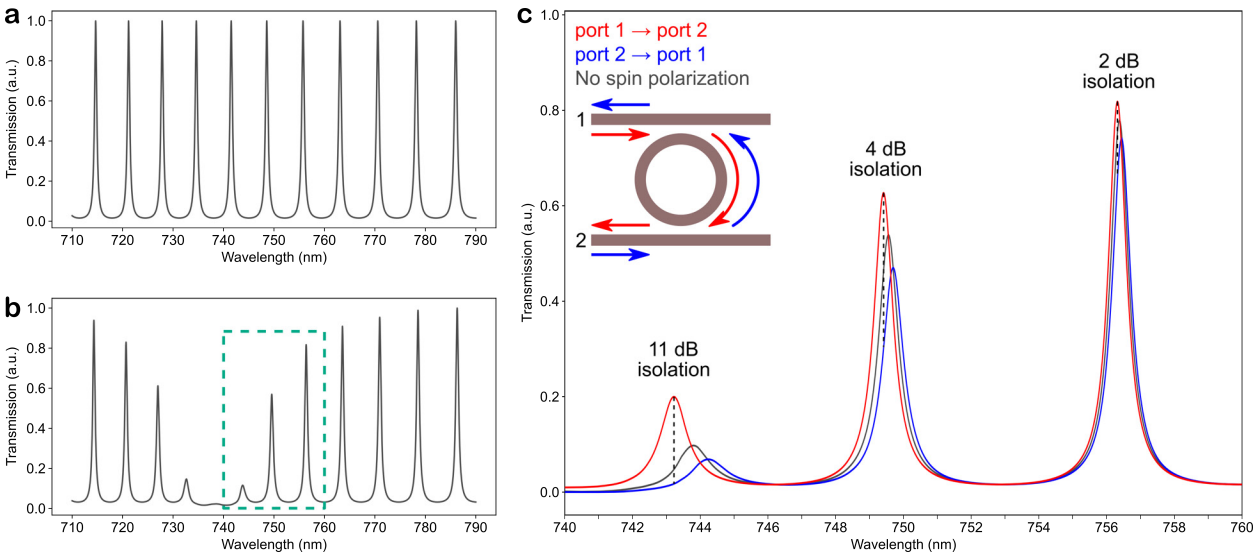

Figure 7.4: Simulated ring transmission. **a**, Drop transmission for a bare resonator device with a ring radius of 5 µm and self-coupling constant $\tau = 0.88$ showing qaulity factors $Q \approx 10^3$. **b**, Modified transmission with the addition of unpolarized WSe_2. **c**, Features highlighted from the dashed region in (**b**) displaying non-reciprocal transmission for $P_s = 0.8$.

isolation values of 10 dB over 250 GHz bandwidth with moderate insertion loss of 20% (Fig. 7.4c). Table 7.1 compares these simulated results with the experimental figures of merit from literature. The key advantage of this scheme is its potential low-power operation, nearly five orders of magnitude lower than in current stat-of-the-art devices.

7.3 Evanescent control of spin polarization

However, the observed microwatt pump power for generating spin polarization in Chapter 6 was performed with far-field excitation. Here, only the evanescent field is used for excitation (Fig. 7.5c), potentially requiring high compensating total waveguide powers. As a proof-of-principle demonstration, we fabricate a waveguide structure into a gated WSe_2 heterostructure (Fig. 7.5a). Note that the monolayer is etched during the fabrication process to ensure separation of contrasting spin polarization on either side of the waveguide. Estimating an in-coupled pumping power of 10 µW flowing through the waveguide, circular

dichroism of 0.1 is found at various probe positions offset from the waveguide by ~ 1 µm (Fig. 7.5d-g). Assuming the far-field $CD = 0.5$ is the saturated value (Fig. 7.5b), the observed circular dichroism corresponds to spin polarization of $P_s \approx 15\%$. Since the spin polarization saturates quickly with pump power (Fig. 6.6a), small adjustments to the interfacial coupling, such as centrally positioning the monolayer, could enable full spin polarization at 10 µW pump power. Additionally, the ring structure could enhance the power of the pump in the cavity mode by a factor of 15, potentially enabling sub-microwatt operation. Lastly, the inversion of circular dichroism with pump direction and probe position additionally confirms that the interface chirality is preserved.

While this near-field generation of spin polarization is promising – and, indeed, may be a useful technique for broader opto-spintronic technologies built on atomically thin semiconductors [316] – the proposed isolator device remains to be realized. Challenges include sample inhomogeneity, which topographically impedes large-scale device integration and spectrally blurs the TMDC optical response, and poor interface control, which results from the etching processes required for embedded photonic structures. Avenues for improvement include cleaning techniques for use in van der Waals assembly [227, 351] and refining the etching method [352, 353].

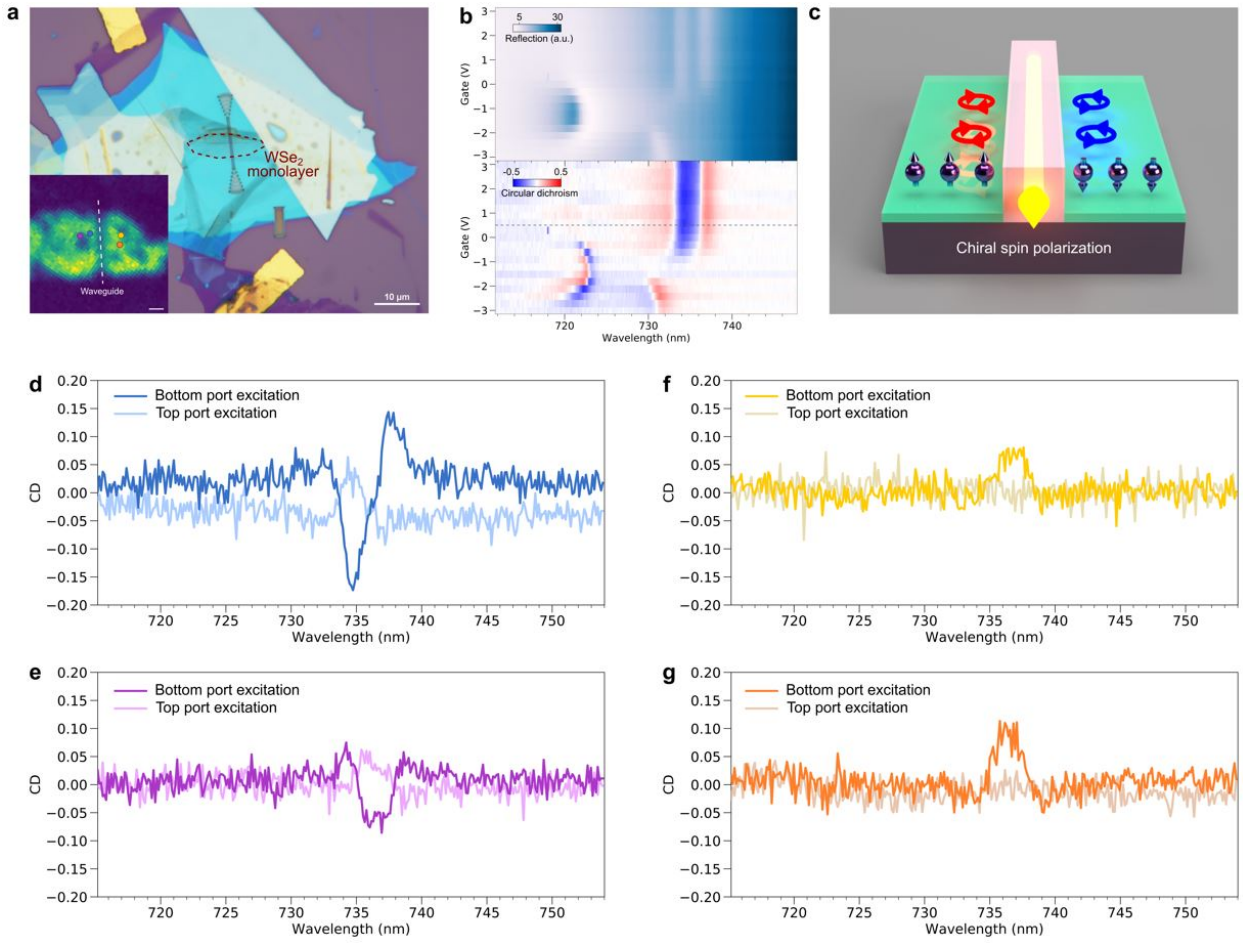

Figure 7.5: Evanescent control of spin polarization. **a**, Sample under study. Inset: Far-field probe positions indicated on the photoluminescence map. Scale bar is 1 µm. **b**, Representative far-field reflection spectra and circular dichroism under far-field pumping. **c**, Optical spin-orbit coupling of the evanescent field generates spin polarized electrons of opposite orientations on opposite sides of the waveguide. **d-g**, CD signal measured at the probe loactions shown in (**a**) under waveguide excitation with an estimated power of 10 µW.

CHAPTER 8

OUTLOOK

The body of work presented in this thesis pushes chiral TMDC-photonic interfaces towards more mature implementations with more advanced capabilities, opening new research directions in optoelectronics, optospintronics, and nanophotonics, as well as in the correlated electron physics of two-dimensional materials. Below, potential avenues building on these results are sketched out for future study.

First, the active emission routing demonstrated in Chapter 5 can be extended straightforwardly to include remote optical control. Long-range spin polarization in monolayer TMDCs can be generated through optical pumping, either with far-field circularly polarized light (Chapter 6) or with chiral near-field evanescent waves (Chapter 7). In the presence of the spin-polarized Fermi sea, excitons excited locally by even linearly polarized light will still emit circularly polarized light [280]. Here, the emission helicity is given by the underlying spin polarization rather than the excitation polarization, marking a truly non-reciprocal effect. By optically controlling the magnitude and orientation of the spin polarization, which can be performed many microns away from a TMDC-photonic interface, emission can be reconfigurably directed into the waveguide, realizing a comprehensive switching capability (*i.e.*, arbitrary left/right emission, not merely balanced/biased emission). Through localized strain engineering [354], arrays of chiral quantum emitters could be positioned in proximity to the chiral nanophotonic waveguide. By controlling their directional coupling to the shared photon reservoir – on-site and in time with tailored optical pulses – new cascaded quantum many-body sates potentially could be explored [205].

Additionally, the temporal measurements in Chapter 6 open interesting opportunities for exploring the dynamic freezing and thawing of Wigner crystals [134, 284] through *in situ*, time-dependent modulations of the electron density. With electrical gating, electron densities can be modulated on the timescale of a few nanoseconds [355, 356], much faster than

the measured lifetime of the magnetic phase. This allows dynamical tuning through phase transitions in 2DEGs. For instance, if the ground state begins in a Wigner crystal, and the electron density is rapidly increased, how quickly will the structure melt and diffuse? If the electron density is then lowered, will it uniformly re-freeze or frustrate into a Wigner glass [357]? This dynamic evolution can be watched by using local magnetic order as a probe for mobility. After locally stabilizing the magnetic order, the diffusive part of its propagation subsequently can be quenched or activated via quantum freezing and thawing of the underlying Wigner crystal. Monitoring the propagation of magnetic order thus could provide information about the Wigner crystal formation, answering fundamental questions about the temporal buildup of correlated phases under dynamic changes in interaction strength.

Beyond the non-reciprocal photonics proposed in Chapter 7, TMDC-photonic interfaces can be implemented in neuromorphic photonic circuits, which have garnered increasing interest as next generation technologies well-suited to parallel, adaptive computation [319, 358]. Demonstrations of neuromorphic networks with conventional silicon photonics have utilized microring weight banks for analog signal processing [359, 360]. In contrast to these architectures, which rely on electrically driven thermal tuning of resonator transmission, ring resonators integrated with WSe_2 will be continuously tunable with light. All-optical operation could improve processing efficiency, lowering power demands below the current milliwatt level, and increase processing accuracy, avoiding noisy thermal crosstalk. Moreover, interfacing nanoscale magnetic materials with photonic circuits enables integrated in-memory computing – where photonic synapses self-tailor signal transmission through plastic neural networks – which is an outstanding challenge for neuromorphic photonic processors [361, 362]. Lastly, introducing substitutional magnetic dopants, such as vanadium [363–365], may even stabilize the magnetic phase at room-temperature for optically reconfigurable, non-volatile memory storage.

BIBLIOGRAPHY

1. Alpha Molykote Corp. *Method of preparing lubricative crystalline molybdenum disulfide.* U.S. Patent US2892741A, June 30, 1959.
2. Polcar, T. in *Encyclopedia of Tribology* (eds Wang, Q. J. & Chung, Y.-W.) 3180–3186 (Springer, 2013).
3. Wilson, J. A. & Yoffe, A. D. The transition metal dichalcogenides: discussion and interpretation of the observed optical, electrical and structural properties. *Advances in Physics* **18,** 193–335 (1969).
4. Yoffe, A. D. Layer compounds. *Annual Review of Materials Science* **3,** 147–170 (1973).
5. Bromley, R. A., Murray, R. B. & Yoffe, A. D. The band structures of some transition metal dichalcogenides. III. Group VIA: trigonal prism materials. *Journal of Physics C: Solid State Physics* **5,** 759 (1972).
6. Kertesz, M. & Hoffmann, R. Octahedral vs. trigonal-prismatic coordination and clustering in transition-metal dichalcogenides. *Journal of the American Chemical Society* **106,** 3453–3460 (1984).
7. IUPAC. *Compendium of Chemical Terminology* 2nd ed. (eds McNaught, A. D. & Wilkinson, A.) (Blackwell Scientific Publications, 1997).
8. Kolobov, A. V. & Tominaga, J. *Two-Dimensional Transition-Metal Dichalcogenides* (Springer, 2016).
9. Katzke, H., Tolédano, P. & Depmeier, W. Phase transitions between polytypes and intralayer superstructures in transition metal dichalcogenides. *Physical Review B* **69,** 134111 (2004).
10. Ribeiro-Soares, J. *et al.* Group theory analysis of phonons in two-dimensional transition metal dichalcogenides. *Physical Review B* **90,** 115438 (2014).
11. Frindt, R. F. & Yoffe, A. D. Physical properties of layer structures: optical properties and photoconductivity of thin crystals of molybdenum disulphide. *Proceedings of the Royal Society of London. Series A. Mathematical and Physical Sciences* **273,** 69–83 (1963).
12. Frindt, R. F. Optical Absorption of a Few Unit-Cell Layers of MoS_2. *Phys. Rev.* **140,** A536–A539 (1965).
13. Frindt, R. F. Single crystals of MoS_2 several molecular layers thick. *Journal of Applied Physics* **37,** 1928–1929 (1966).
14. Splendiani, A. *et al.* Emerging photoluminescence in monolayer MoS_2. *Nano Letters* **10,** 1271–1275 (2010).
15. Mak, K. F., Lee, C., Hone, J., Shan, J. & Heinz, T. F. Atomically Thin MoS_2: A New Direct-Gap Semiconductor. *Physical Review Letters* **105,** 136805 (2010).
16. The Royal Swedish Academy of Science. *The Nobel Prize in Physics 2010: Graphene – the perfect atomic lattice.* Oct. 2010.

17. Novoselov, K. S. *et al.* Electric Field Effect in Atomically Thin Carbon Films. *Science* **306,** 666–669 (2004).

18. Novoselov, K. S. *et al.* Two-dimensional atomic crystals. *Proceedings of the National Academy of Sciences* **102,** 10451–10453 (2005).

19. Blake, P. *et al.* Making graphene visible. *Applied Physics Letters* **91,** 063124 (2007).

20. Abergel, D. S. L., Russell, A. & Fal'ko, V. I. Visibility of graphene flakes on a dielectric substrate. *Applied Physics Letters* **91,** 063125 (2007).

21. Castellanos-Gomez, A., Agraït, N. & Rubio-Bollinger, G. Optical identification of atomically thin dichalcogenide crystals. *Applied Physics Letters* **96,** 213116 (2010).

22. Novoselov, K. S. *et al.* Two-dimensional gas of massless Dirac fermions in graphene. *Nature* **438,** 197–200 (2005).

23. Zhang, Y., Tan, Y.-W., Stormer, H. L. & Kim, P. Experimental observation of the quantum Hall effect and Berry's phase in graphene. *Nature* **438,** 201–204 (2005).

24. Ramasubramaniam, A. Large excitonic effects in monolayers of molybdenum and tungsten dichalcogenides. *Physical Review B* **86,** 115409 (2012).

25. Li, T. & Galli, G. Electronic Properties of MoS_2 Nanoparticles. *The Journal of Physical Chemistry C* **111,** 16192–16196 (2007).

26. Lebègue, S. & Eriksson, O. Electronic structure of two-dimensional crystals from *ab initio* theory. *Physical Review B* **79,** 115409 (2009).

27. Wallace, P. R. The Band Theory of Graphite. *Phys. Rev.* **71,** 622–634 (1947).

28. Liu, G.-B., Xiao, D., Yao, Y., Xu, X. & Yao, W. Electronic structures and theoretical modelling of two-dimensional group-VIB transition metal dichalcogenides. *Chemical Society Reviews* **44,** 2643–2663 (2015).

29. Xiao, D., Yao, W. & Niu, Q. Valley-Contrasting Physics in Graphene: Magnetic Moment and Topological Transport. *Physical Review Letters* **99,** 236809 (2007).

30. Xiao, D., Liu, G.-B., Feng, W., Xu, X. & Yao, W. Coupled Spin and Valley Physics in Monolayers of MoS_2 and Other Group-VI Dichalcogenides. *Physical Review Letters* **108,** 196802 (2012).

31. Xiao, D., Chang, M.-C. & Niu, Q. Berry phase effects on electronic properties. *Reviews of Modern Physics* **82,** 1959–2007 (2010).

32. Zhu, Z. Y., Cheng, Y. C. & Schwingenschlögl, U. Giant spin-orbit-induced spin splitting in two-dimensional transition-metal dichalcogenide semiconductors. *Physical Review B* **84,** 153402 (2011).

33. Kośmider, K., González, J. W. & Fernández-Rossier, J. Large spin splitting in the conduction band of transition metal dichalcogenide monolayers. *Physical Review B* **88,** 245436 (2013).

34. Liu, G.-B., Shan, W.-Y., Yao, Y., Yao, W. & Xiao, D. Three-band tight-binding model for monolayers of group-VIB transition metal dichalcogenides. *Physical Review B* **88,** 085433 (2013).

35. Kormányos, A. *et al.* k· p theory for two-dimensional transition metal dichalcogenide semiconductors. *2D Materials* **2,** 022001 (2015).

36. Gusakova, J. *et al.* Electronic Properties of Bulk and Monolayer TMDs: Theoretical Study Within DFT Framework (GVJ-2e Method). *physica status solidi (a)* **214,** 1700218 (2017).

37. Wang, G. *et al.* Colloquium: Excitons in atomically thin transition metal dichalcogenides. *Reviews of Modern Physics* **90,** 021001 (2018).

38. Xu, X., Yao, W., Xiao, D. & Heinz, T. F. Spin and pseudospins in layered transition metal dichalcogenides. *Nature Physics* **10,** 343–350 (2014).

39. Yao, W., Xiao, D. & Niu, Q. Valley-dependent optoelectronics from inversion symmetry breaking. *Physical Review B* **77,** 235406 (2008).

40. Cao, T. *et al.* Valley-selective circular dichroism of monolayer molybdenum disulphide. *Nature Communications* **3,** 887 (2012).

41. Zeng, H., Dai, J., Yao, W., Xiao, D. & Cui, X. Valley polarization in MoS_2 monolayers by optical pumping. *Nature Nanotechnology* **7,** 490–493 (2012).

42. Mak, K. F., He, K., Shan, J. & Heinz, T. F. Control of valley polarization in monolayer MoS_2 by optical helicity. *Nature Nanotechnology* **7,** 494–498 (2012).

43. Sallen, G. *et al.* Robust optical emission polarization in MoS_2 monolayers through selective valley excitation. *Physical Review B* **86,** 081301 (2012).

44. Jones, A. M. *et al.* Optical generation of excitonic valley coherence in monolayer WSe_2. *Nature Nanotechnology* **8,** 634–638 (2013).

45. Hao, K. *et al.* Direct measurement of exciton valley coherence in monolayer WSe_2. *Nature Physics* **12,** 677–682 (2016).

46. Ye, Z., Sun, D. & Heinz, T. F. Optical manipulation of valley pseudospin. *Nature Physics* **13,** 26–29 (2017).

47. Yang, L. *et al.* Long-lived nanosecond spin relaxation and spin coherence of electrons in monolayer MoS_2 and WS_2. *Nature Physics* **11,** 830–834 (2015).

48. Xie, L. & Cui, X. Manipulating spin-polarized photocurrents in 2D transition metal dichalcogenides. *Proceedings of the National Academy of Sciences* **113,** 3746–3750 (2016).

49. Chen, X., Yan, T., Zhu, B., Yang, S. & Cui, X. Optical control of spin polarization in monolayer transition metal dichalcogenides. *ACS Nano* **11,** 1581–1587 (2017).

50. Knox, R. S. *Theory of Excitons.* 207 (Academic Press, New York, 1963).

51. Qiu, D. Y., da Jornada, F. H. & Louie, S. G. Optical Spectrum of MoS_2: Many-Body Effects and Diversity of Exciton States. *Physical Review Letters* **111,** 216805 (2013).

52. Yoffe, A. Low-dimensional systems: quantum size effects and electronic properties of semiconductor microcrystallites (zero-dimensional systems) and some quasi-two-dimensional systems. *Advances in Physics* **42,** 173–262 (1993).

53. Zhang, C., Johnson, A., Hsu, C.-L., Li, L.-J. & Shih, C.-K. Direct imaging of band profile in single layer MoS_2 on graphite: quasiparticle energy gap, metallic edge states, and edge band bending. *Nano Letters* **14,** 2443–2447 (2014).

54. Ugeda, M. M. *et al.* Giant bandgap renormalization and excitonic effects in a monolayer transition metal dichalcogenide semiconductor. *Nature Materials* **13,** 1091–1095 (2014).

55. Chernikov, A. *et al.* Exciton Binding Energy and Nonhydrogenic Rydberg Series in Monolayer WS_2. *Physical Review Letters* **113,** 076802 (2014).

56. Ivanov, A., Haug, H. & Keldysh, L. Optics of excitonic molecules in semiconductors and semiconductor microstructures. *Physics Reports* **296,** 237–336. ISSN: 0370-1573 (1998).

57. Van Tuan, D., Yang, M. & Dery, H. Coulomb interaction in monolayer transition-metal dichalcogenides. *Physical Review B* **98,** 125308 (2018).

58. Shree, S., Paradisanos, I., Marie, X., Robert, C. & Urbaszek, B. Guide to optical spectroscopy of layered semiconductors. *Nature Reviews Physics* **3,** 39–54 (2021).

59. Glazov, M. M. *et al.* Exciton fine structure and spin decoherence in monolayers of transition metal dichalcogenides. *Physical Review B* **89,** 201302 (2014).

60. Selig, M. *et al.* Excitonic linewidth and coherence lifetime in monolayer transition metal dichalcogenides. *Nature Communications* **7,** 13279 (2016).

61. Robert, C. *et al.* Exciton radiative lifetime in transition metal dichalcogenide monolayers. *Physical Review B* **93,** 205423 (2016).

62. Raja, A. *et al.* Dielectric disorder in two-dimensional materials. *Nature Nanotechnology* **14,** 832–837 (2019).

63. Cadiz, F. *et al.* Excitonic Linewidth Approaching the Homogeneous Limit in MoS_2-Based van der Waals Heterostructures. *Physical Review X* **7,** 021026 (2017).

64. Ajayi, O. A. *et al.* Approaching the intrinsic photoluminescence linewidth in transition metal dichalcogenide monolayers. *2D Materials* **4,** 031011 (2017).

65. Mak, K. F. *et al.* Tightly bound trions in monolayer MoS_2. *Nature Materials* **12,** 207–211 (2013).

66. Ross, J. S. *et al.* Electrical control of neutral and charged excitons in a monolayer semiconductor. *Nature Communications* **4,** 1474 (2013).

67. Courtade, E. *et al.* Charged excitons in monolayer WSe_2: Experiment and theory. *Physical Review B* **96,** 085302 (2017).

68. Plechinger, G. *et al.* Identification of excitons, trions and biexcitons in single-layer WS_2. *physica status solidi (RRL) – Rapid Research Letters* **9,** 457–461 (2015).

69. You, Y. *et al.* Observation of biexcitons in monolayer WSe_2. *Nature Physics* **11,** 477–481 (2015).

70. Sie, E. J., Frenzel, A. J., Lee, Y.-H., Kong, J. & Gedik, N. Intervalley biexcitons and many-body effects in monolayer MoS_2. *Physical Review B* **92,** 125417 (2015).

71. Zhang, X.-X. *et al.* Magnetic brightening and control of dark excitons in monolayer WSe_2. *Nature Nanotechnology* **12,** 883–888 (2017).

72. Malic, E. *et al.* Dark excitons in transition metal dichalcogenides. *Physical Review Materials* **2,** 014002 (2018).

73. Robert, C. *et al.* Measurement of the spin-forbidden dark excitons in MoS_2 and $MoSe_2$ monolayers. *Nature Communications* **11,** 4037 (2020).

74. Zhou, Y. *et al.* Probing dark excitons in atomically thin semiconductors via near-field coupling to surface plasmon polaritons. *Nature Nanotechnology* **12,** 856–860 (2017).

75. Wang, G. *et al.* In-Plane Propagation of Light in Transition Metal Dichalcogenide Monolayers: Optical Selection Rules. *Physical Review Letters* **119,** 047401 (2017).

76. Li, Z. *et al.* Emerging photoluminescence from the dark-exciton phonon replica in monolayer WSe_2. *Nature Communications* **10,** 2469 (2019).

77. Liu, E. *et al.* Valley-selective chiral phonon replicas of dark excitons and trions in monolayer WSe_2. *Physical Review Research* **1,** 032007 (2019).

78. Liu, E. *et al.* Multipath Optical Recombination of Intervalley Dark Excitons and Trions in Monolayer WSe_2. *Physical Review Letters* **124,** 196802 (2020).

79. Srivastava, A. *et al.* Optically active quantum dots in monolayer WSe_2. *Nature Nanotechnology* **10,** 491–496 (2015).

80. Palacios-Berraquero, C. *et al.* Large-scale quantum-emitter arrays in atomically thin semiconductors. *Nature Communications* **8,** 15093 (2017).

81. Wang, Z., Zhao, L., Mak, K. F. & Shan, J. Probing the Spin-Polarized Electronic Band Structure in Monolayer Transition Metal Dichalcogenides by Optical Spectroscopy. *Nano Letters* **17,** 740–746 (2017).

82. Klingshirn, C. F. *Semiconductor Optics* (Springer, 2012).

83. Efimkin, D. K. & MacDonald, A. H. Many-body theory of trion absorption features in two-dimensional semiconductors. *Physical Review B* **95,** 035417 (2017).

84. Glazov, M. M. Optical properties of charged excitons in two-dimensional semiconductors. *The Journal of Chemical Physics* **153,** 034703 (2020).

85. Imamoğlu, A., Cotlet, O. & Schmidt, R. Exciton–polarons in two-dimensional semiconductors and the Tavis–Cummings model. *Comptes Rendus. Physique* **22,** 1–8 (2021).

86. Katsch, F. & Knorr, A. Excitonic theory of doping-dependent optical response in atomically thin semiconductors. *Physical Review B* **105,** 045301 (2022).

87. Scuri, G. *et al.* Large Excitonic Reflectivity of Monolayer $MoSe_2$ Encapsulated in Hexagonal Boron Nitride. *Physical Review Letters* **120,** 037402 (2018).

88. Back, P., Zeytinoglu, S., Ijaz, A., Kroner, M. & Imamoğlu, A. Realization of an Electrically Tunable Narrow-Bandwidth Atomically Thin Mirror Using Monolayer $MoSe_2$. *Physical Review Letters* **120,** 037401 (2018).

89. Moody, G., Schaibley, J. & Xu, X. Exciton dynamics in monolayer transition metal dichalcogenides. *J. Opt. Soc. Am. B* **33,** C39–C49 (2016).

90. Moody, G. *et al.* Intrinsic homogeneous linewidth and broadening mechanisms of excitons in monolayer transition metal dichalcogenides. *Nature Communications* **6,** 8315 (2015).

91. Hao, K. *et al.* Neutral and charged inter-valley biexcitons in monolayer $MoSe_2$. *Nature Communications* **8,** 15552 (2017).

92. Yu, T. & Wu, M. W. Valley depolarization due to intervalley and intravalley electron-hole exchange interactions in monolayer MoS_2. *Physical Review B* **89,** 205303 (2014).

93. Zhu, C. R. *et al.* Exciton valley dynamics probed by Kerr rotation in WSe_2 monolayers. *Physical Review B* **90,** 161302 (2014).

94. Wang, G. *et al.* Valley dynamics probed through charged and neutral exciton emission in monolayer WSe_2. *Physical Review B* **90,** 075413 (2014).

95. Singh, A. *et al.* Long-Lived Valley Polarization of Intravalley Trions in Monolayer WSe_2. *Physical Review Letters* **117,** 257402 (2016).

96. Li, J. *et al.* Valley relaxation of resident electrons and holes in a monolayer semiconductor: Dependence on carrier density and the role of substrate-induced disorder. *Physical Review Materials* **5,** 044001 (2021).

97. Li, Y. *et al.* Valley Splitting and Polarization by the Zeeman Effect in Monolayer $MoSe_2$. *Physical Review Letters* **113,** 266804 (2014).

98. MacNeill, D. *et al.* Breaking of Valley Degeneracy by Magnetic Field in Monolayer $MoSe_2$. *Physical Review Letters* **114,** 037401 (3 2015).

99. Aivazian, G. *et al.* Magnetic control of valley pseudospin in monolayer WSe_2. *Nature Physics* **11,** 148–152 (2015).

100. Srivastava, A. *et al.* Valley Zeeman effect in elementary optical excitations of monolayer WSe_2. *Nature Physics* **11,** 141–147 (2015).

101. Back, P. *et al.* Giant Paramagnetism-Induced Valley Polarization of Electrons in Charge-Tunable Monolayer $MoSe_2$. *Physical Review Letters* **118,** 237404 (2017).

102. Wang, Z., Mak, K. F. & Shan, J. Strongly Interaction-Enhanced Valley Magnetic Response in Monolayer WSe_2. *Physical Review Letters* **120,** 066402 (2018).

103. Kim, J. *et al.* Ultrafast generation of pseudo-magnetic field for valley excitons in WSe_2 monolayers. *Science* **346,** 1205–1208 (2014).

104. Sie, E. J. *et al.* Valley-selective optical Stark effect in monolayer WS_2. *Nature Materials* **14,** 290–294 (2015).

105. Geim, A. K. & Grigorieva, I. V. Van der Waals heterostructures. *Nature* **499,** 419–425 (2013).

106. Novoselov, K. S., Mishchenko, A., Carvalho, o. A. & Castro Neto, A. 2D materials and van der Waals heterostructures. *Science* **353,** aac9439 (2016).

107. Liu, Y. *et al.* Van der Waals heterostructures and devices. *Nature Reviews Materials* **1,** 1–17 (2016).

108. Rhodes, D., Chae, S. H., Ribeiro-Palau, R. & Hone, J. Disorder in van der Waals heterostructures of 2D materials. *Nature Materials* **18,** 541–549 (2019).

109. Jin, C. *et al.* Ultrafast dynamics in van der Waals heterostructures. *Nature Nanotechnology* **13,** 994–1003 (2018).

110. Rivera, P. *et al.* Interlayer valley excitons in heterobilayers of transition metal dichalcogenides. *Nature Nanotechnology* **13,** 1004–1015 (2018).

111. Jauregui, L. A. *et al.* Electrical control of interlayer exciton dynamics in atomically thin heterostructures. *Science* **366,** 870–875 (2019).

112. Unuchek, D. *et al.* Room-temperature electrical control of exciton flux in a van der Waals heterostructure. *Nature* **560,** 340–344 (2018).

113. Carr, S. *et al.* Twistronics: Manipulating the electronic properties of two-dimensional layered structures through their twist angle. *Physical Review B* **95,** 075420 (2017).

114. Huang, D., Choi, J., Shih, C.-K. & Li, X. Excitons in semiconductor moiré superlattices. *Nature Nanotechnology* **17,** 227–238 (2022).

115. Andrei, E. Y. *et al.* The marvels of moiré materials. *Nature Reviews Materials* **6,** 201–206 (2021).

116. Cao, Y. *et al.* Unconventional superconductivity in magic-angle graphene superlattices. *Nature* **556,** 43–50 (2018).

117. Cao, Y. *et al.* Correlated insulator behaviour at half-filling in magic-angle graphene superlattices. *Nature* **556,** 80–84 (2018).

118. Alexandradinata, A. *et al.* The Future of the Correlated Electron Problem. *arXiv* **arXiv:2010.00584** (2020).

119. Bloch, F. Bemerkung zur Elektronentheorie des Ferromagnetismus und der elektrischen Leitfähigkeit. *Zeitschrift für Physik* **57,** 545–555 (1929).

120. Wigner, E. On the interaction of electrons in metals. *Physical Review* **46,** 1002 (1934).

121. Mott, N. F. & Peierls, R. Discussion of the paper by de Boer and Verwey. *Proceedings of the Physical Society* **49,** 72 (1937).

122. Ando, T., Fowler, A. B. & Stern, F. Electronic properties of two-dimensional systems. *Reviews of Modern Physics* **54,** 437–672 (1982).

123. Spivak, B., Kravchenko, S. V., Kivelson, S. A. & Gao, X. P. A. Colloquium: Transport in strongly correlated two dimensional electron fluids. *Reviews of Modern Physics* **82,** 1743–1766 (2010).

124. Hwang, H. Y. *et al.* Emergent phenomena at oxide interfaces. *Nature Materials* **11,** 103–113 (2012).

125. Hossain, M. S. *et al.* Observation of spontaneous ferromagnetism in a two-dimensional electron system. *Proceedings of the National Academy of Sciences* **117,** 32244–32250 (2020).

126. Chung, Y. J. *et al.* Ultra-high-quality two-dimensional electron systems. *Nature Materials* **20,** 632–637 (2021).

127. Shayegan, M. *High Magnetic Fields: Science and Technology* (eds Herlach, F. & Miura, N.) 31–60 (World Scientific, 2006).

128. Jain, J. K. *Composite Fermions* (Cambridge University Press, 2007).

129. Attaccalite, C., Moroni, S., Gori-Giorgi, P. & Bachelet, G. B. Correlation Energy and Spin Polarization in the 2D Electron Gas. *Physical Review Letters* **88,** 256601 (2002).

130. Drummond, N. D. & Needs, R. J. Phase Diagram of the Low-Density Two-Dimensional Homogeneous Electron Gas. *Physical Review Letters* **102,** 126402 (2009).

131. Senatore, G. & March, N. H. Recent progress in the field of electron correlation. *Reviews of Modern Physics* **66,** 445–479 (1994).

132. Tanatar, B. & Ceperley, D. M. Ground state of the two-dimensional electron gas. *Physical Review B* **39,** 5005–5016 (1989).

133. Shi, Q. *et al.* Odd-and even-denominator fractional quantum Hall states in monolayer WSe_2. *Nature Nanotechnology* **15,** 569–573 (2020).

134. Smoleński, T. *et al.* Signatures of Wigner crystal of electrons in a monolayer semiconductor. *Nature* **595,** 53–57 (2021).

135. Roch, J. G. *et al.* Spin-polarized electrons in monolayer MoS_2. *Nature Nanotechnology* **14,** 432–436 (2019).

136. Roch, J. G. *et al.* First-Order Magnetic Phase Transition of Mobile Electrons in Monolayer MoS_2. *Physical Review Letters* **124,** 187602 (2020).

137. Van der Donck, M. & Peeters, F. M. Rich many-body phase diagram of electrons and holes in doped monolayer transition metal dichalcogenides. *Physical Review B* **98,** 115432 (2018).

138. Mukherjee, D. K., Kundu, A. & Fertig, H. A. Spin response and collective modes in simple metal dichalcogenides. *Physical Review B* **98,** 184413 (2018).

139. Braz, J. E. H., Amorim, B. & Castro, E. V. Valley-polarized magnetic state in hole-doped monolayers of transition-metal dichalcogenides. *Physical Review B* **98,** 161406 (2018).

140. Miserev, D., Klinovaja, J. & Loss, D. Exchange intervalley scattering and magnetic phase diagram of transition metal dichalcogenide monolayers. *Physical Review B* **100,** 014428 (2019).

141. Miserev, D., Klinovaja, J. & Loss, D. Magnetic phase transitions in two-dimensional two-valley semiconductors with in-plane magnetic field. *Physical Review B* **103,** 024401 (2021).

142. Fan, P. & Zhu, Z.-G. Magnetic order transition in monolayer MoS_2 induced by strong intervalley correlation. *Physical Review B* **104,** 195417 (2021).

143. Miserev, D., Loss, D. & Klinovaja, J. Instability of the ferromagnetic quantum critical point and symmetry of the ferromagnetic ground state in two-dimensional and three-dimensional electron gases with arbitrary spin-orbit splitting. *Physical Review B* **106,** 134417 (2022).

144. Knobel, M. *et al.* Superparamagnetism and Other Magnetic Features in Granular Materials: A Review on Ideal and Real Systems. *Journal of Nanoscience and Nanotechnology* **8,** 2836–2857 (2008).

145. Anahory, Y. *et al.* Emergent nanoscale superparamagnetism at oxide interfaces. *Nature Communications* **7,** 12566 (2016).

146. Kittel, C. Theory of the Structure of Ferromagnetic Domains in Films and Small Particles. *Phys. Rev.* **70,** 965–971 (1946).

147. Mermin, N. D. & Wagner, H. Absence of Ferromagnetism or Antiferromagnetism in One- or Two-Dimensional Isotropic Heisenberg Models. *Physical Review Letters* **17,** 1133–1136 (1966).

148. Loss, D., Pedrocchi, F. L. & Leggett, A. J. Absence of Spontaneous Magnetic Order of Lattice Spins Coupled to Itinerant Interacting Electrons in One and Two Dimensions. *Physical Review Letters* **107,** 107201 (2011).

149. Jenkins, S. *et al.* Breaking through the Mermin-Wagner limit in 2D van der Waals magnets. *Nature Communications* **13,** 6917 (2022).

150. Thiel, L. *et al.* Probing magnetism in 2D materials at the nanoscale with single-spin microscopy. *Science* **364,** 973–976 (2019).

151. Nolting, W. *Quantum Theory of Magnetism* (ed Ramakanth, A.) (Springer, 2008).

152. Heitler, W. & London, F. Wechselwirkung neutraler Atome und homöopolare Bindung nach der Quantenmechanik. *Zeitschrift für Physik* **44,** 455–472 (1927).

153. Auerbach, A. *Interacting Electrons and Quantum Magnetism* (Springer-Verlag, 1994).

154. Fazekas, P. *Lecture Notes on Electron Correlation and Magnetism* (World Scientific, 1999).

155. Stoner, E. C. Collective Electron Ferromagnetism. *Proceedings of the Royal Society of London. Series A. Mathematical and Physical Sciences* **165,** 372–414 (1938).

156. Yun, S. J. *et al.* Ferromagnetic Order at Room Temperature in Monolayer WSe_2 Semiconductor via Vanadium Dopant. *Advanced Science* **7,** 1903076 (2020).

157. Poynting, J. H. The wave motion of a revolving shaft, and a suggestion as to the angular momentum in a beam of circularly polarised light. *Proceedings of the Royal Society of London. Series A.* **82,** 560–567 (1909).

158. Beth, R. A. Mechanical Detection and Measurement of the Angular Momentum of Light. *Phys. Rev.* **50,** 115–125 (1936).

159. Allen, L., Beijersbergen, M. W., Spreeuw, R. J. C. & Woerdman, J. P. Orbital angular momentum of light and the transformation of Laguerre-Gaussian laser modes. *Physical Review A* **45,** 8185–8189 (1992).

160. He, H., Friese, M. E. J., Heckenberg, N. R. & Rubinsztein-Dunlop, H. Direct Observation of Transfer of Angular Momentum to Absorptive Particles from a Laser Beam with a Phase Singularity. *Physical Review Letters* **75,** 826–829 (1995).

161. *The Angular Momentum of Light* (eds Andrews, D. L. & Babiker, M.) (Cambridge University Press, 2012).

162. Bliokh, K. Y. Geometrodynamics of polarized light: Berry phase and spin Hall effect in a gradient-index medium. *Journal of Optics A: Pure and Applied Optics* **11,** 094009 (2009).

163. Bliokh, K. Y., Alonso, M. A., Ostrovskaya, E. A. & Aiello, A. Angular momenta and spin-orbit interaction of nonparaxial light in free space. *Physical Review A* **82,** 063825 (2010).

164. Bliokh, K. Y., Rodríguez-Fortuño, F. J., Nori, F. & Zayats, A. V. Spin–orbit interactions of light. *Nature Photonics* **9,** 796–808 (2015).

165. Aiello, A., Banzer, P., Neugebauer, M. & Leuchs, G. From transverse angular momentum to photonic wheels. *Nature Photonics* **9,** 789–795 (2015).

166. Lodahl, P. *et al.* Chiral quantum optics. *Nature* **541,** 473–480 (2017).

167. Banzer, P. *et al.* The photonic wheel-demonstration of a state of light with purely transverse angular momentum. *Journal of the European Optical Society – Rapid Publications* **8** (2013).

168. Bliokh, K. Y. & Nori, F. Transverse and longitudinal angular momenta of light. *Physics Reports* **592,** 1–38 (2015).

169. Bliokh, K. Y., Bekshaev, A. Y. & Nori, F. Dual electromagnetism: helicity, spin, momentum and angular momentum. *New Journal of Physics* **15,** 033026 (2013).

170. Bliokh, K. Y., Bekshaev, A. Y. & Nori, F. Extraordinary momentum and spin in evanescent waves. *Nature Communications* **5,** 3300 (2014).

171. Yang, N. & Cohen, A. E. Local geometry of electromagnetic fields and its role in molecular multipole transitions. *The Journal of Physical Chemistry B* **115,** 5304–5311 (2011).

172. Mathevet, R. & Rikken, G. L. J. A. Magnetic circular dichroism as a local probe of the polarization of a focused Gaussian beam. *Opt. Mater. Express* **4,** 2574–2585 (2014).

173. Neugebauer, M., Bauer, T., Aiello, A. & Banzer, P. Measuring the Transverse Spin Density of Light. *Physical Review Letters* **114,** 063901 (2015).

174. Maier, S. A. *et al. Plasmonics: Fundamentals and Applications* (Springer, 2007).

175. Bliokh, K. Y., Bliokh, Y. P., Freilikher, V., Savel'ev, S. & Nori, F. Colloquium: Unusual resonators: Plasmonics, metamaterials, and random media. *Reviews of Modern Physics* **80,** 1201–1213 (2008).

176. Bliokh, K. Y. & Nori, F. Transverse spin of a surface polariton. *Physical Review A* **85,** 061801 (2012).

177. Kim, K.-Y., Lee, I.-M., Kim, J., Jung, J. & Lee, B. Time reversal and the spin angular momentum of transverse-electric and transverse-magnetic surface modes. *Physical Review A* **86,** 063805 (2012).

178. Bliokh, K. Y., Smirnova, D. & Nori, F. Quantum spin Hall effect of light. *Science* **348,** 1448–1451 (2015).

179. Rodríguez-Fortuño, F. J. *et al.* Near-field interference for the unidirectional excitation of electromagnetic guided modes. *Science* **340,** 328–330 (2013).

180. O'Connor, D., Ginzburg, P., Rodríguez-Fortuño, F. J., Wurtz, G. A. & Zayats, A. V. Spin–orbit coupling in surface plasmon scattering by nanostructures. *Nature Communications* **5,** 5327 (2014).

181. Lin, J. *et al.* Polarization-controlled tunable directional coupling of surface plasmon polaritons. *Science* **340,** 331–334 (2013).

182. Mueller, J. P. B. & Capasso, F. Asymmetric surface plasmon polariton emission by a dipole emitter near a metal surface. *Physical Review B* **88,** 121410 (2013).

183. Brambilla, G. Optical fibre nanowires and microwires: a review. *Journal of Optics* **12,** 043001 (2010).

184. Joannopoulos, J. D., Villeneuve, P. R. & Fan, S. Photonic crystals: putting a new twist on light. *Nature* **386,** 143–149 (1997).

185. Petersen, J., Volz, J. & Rauschenbeutel, A. Chiral nanophotonic waveguide interface based on spin-orbit interaction of light. *Science* **346,** 67–71 (2014).

186. Le Feber, B., Rotenberg, N. & Kuipers, L. Nanophotonic control of circular dipole emission. *Nature Communications* **6,** 6695 (2015).

187. Kimble, H. J. The quantum internet. *Nature* **453,** 1023–1030 (2008).

188. Lodahl, P., Mahmoodian, S. & Stobbe, S. Interfacing single photons and single quantum dots with photonic nanostructures. *Reviews of Modern Physics* **87,** 347–400 (2015).

189. Reiserer, A. & Rempe, G. Cavity-based quantum networks with single atoms and optical photons. *Reviews of Modern Physics* **87,** 1379–1418 (2015).

190. Luxmoore, I. J. *et al.* Interfacing Spins in an InGaAs Quantum Dot to a Semiconductor Waveguide Circuit Using Emitted Photons. *Physical Review Letters* **110,** 037402 (2013).

191. Mitsch, R., Sayrin, C., Albrecht, B., Schneeweiss, P. & Rauschenbeutel, A. Quantum state-controlled directional spontaneous emission of photons into a nanophotonic waveguide. *Nature Communications* **5,** 5713 (2014).

192. Söllner, I. *et al.* Deterministic photon–emitter coupling in chiral photonic circuits. *Nature Nanotechnology* **10,** 775–778 (2015).

193. Coles, R. J. *et al.* Chirality of nanophotonic waveguide with embedded quantum emitter for unidirectional spin transfer. *Nature Communications* **7,** 11183 (2016).

194. Junge, C., O'Shea, D., Volz, J. & Rauschenbeutel, A. Strong Coupling between Single Atoms and Nontransversal Photons. *Physical Review Letters* **110,** 213604 (2013).

195. Shomroni, I. *et al.* All-optical routing of single photons by a one-atom switch controlled by a single photon. *Science* **345,** 903–906 (2014).

196. Sayrin, C. *et al.* Nanophotonic Optical Isolator Controlled by the Internal State of Cold Atoms. *Physical Review X* **5,** 041036 (2015).

197. Scheucher, M., Hilico, A., Will, E., Volz, J. & Rauschenbeutel, A. Quantum optical circulator controlled by a single chirally coupled atom. *Science* **354,** 1577–1580 (2016).

198. Lenferink, E. J., Wei, G. & Stern, N. P. Coherent optical non-reciprocity in axisymmetric resonators. *Opt. Express* **22,** 16099–16111 (2014).

199. Xia, K. *et al.* Reversible nonmagnetic single-photon isolation using unbalanced quantum coupling. *Physical Review A* **90,** 043802 (2014).

200. Chang, D. E., Douglas, J. S., González-Tudela, A., Hung, C.-L. & Kimble, H. J. Colloquium: Quantum matter built from nanoscopic lattices of atoms and photons. *Reviews of Modern Physics* **90,** 031002 (2018).

201. Gardiner, C. W. Driving a quantum system with the output field from another driven quantum system. *Physical Review Letters* **70,** 2269–2272 (1993).

202. Carmichael, H. J. Quantum trajectory theory for cascaded open systems. *Physical Review Letters* **70,** 2273–2276 (1993).

203. Stannigel, K., Rabl, P. & Zoller, P. Driven-dissipative preparation of entangled states in cascaded quantum-optical networks. *New Journal of Physics* **14,** 063014 (2012).

204. Ramos, T., Pichler, H., Daley, A. J. & Zoller, P. Quantum Spin Dimers from Chiral Dissipation in Cold-Atom Chains. *Physical Review Letters* **113,** 237203 (2014).

205. Pichler, H., Ramos, T., Daley, A. J. & Zoller, P. Quantum optics of chiral spin networks. *Physical Review A* **91,** 042116 (2015).

206. Wang, Q. H., Kalantar-Zadeh, K., Kis, A., Coleman, J. N. & Strano, M. S. Electronics and optoelectronics of two-dimensional transition metal dichalcogenides. *Nature Nanotechnology* **7,** 699–712 (2012).

207. Mak, K. F. & Shan, J. Photonics and optoelectronics of 2D semiconductor transition metal dichalcogenides. *Nature Photonics* **10,** 216–226 (2016).

208. Huang, L. *et al.* Enhanced light–matter interaction in two-dimensional transition metal dichalcogenides. *Reports on Progress in Physics* **85,** 046401 (2022).

209. Krasnok, A. & Alù, A. Valley-selective response of nanostructures coupled to 2D transition-metal dichalcogenides. *Applied Sciences* **8,** 1157 (2018).

210. Li, S., Wang, H., Wang, J., Chen, H. & Shao, L. Control of light–valley interactions in 2D transition metal dichalcogenides with nanophotonic structures. *Nanoscale* **13,** 6357–6372 (2021).

211. Deng, M. *et al.* Plasmonic Modulation of Valleytronic Emission in Two-Dimensional Transition Metal Dichalcogenides. *Advanced Functional Materials* **31,** 2010234 (2021).

212. Chervy, T. *et al.* Room temperature chiral coupling of valley excitons with spin-momentum locked surface plasmons. *ACS Photonics* **5,** 1281–1287 (2018).

213. Chen, P.-G. *et al.* Long-range directional routing and spatial selection of high-spin-purity valley trion emission in monolayer WS_2. *ACS Nano* **15,** 18163–18171 (2021).

214. Chen, Y. *et al.* Chirality-dependent unidirectional routing of WS_2 valley photons in a nanocircuit. *Nature Nanotechnology* **17,** 1178–1182 (2022).

215. Gong, S.-H., Alpeggiani, F., Sciacca, B., Garnett, E. C. & Kuipers, L. Nanoscale chiral valley-photon interface through optical spin-orbit coupling. *Science* **359,** 443–447 (2018).

216. Sun, L. *et al.* Separation of valley excitons in a MoS_2 monolayer using a subwavelength asymmetric groove array. *Nature Photonics* **13,** 180–184 (2019).

217. Yang, Z., Aghaeimeibodi, S. & Waks, E. Chiral light-matter interactions using spin-valley states in transition metal dichalcogenides. *Optics Express* **27,** 21367–21379 (2019).

218. Guo, Q. *et al.* Routing a chiral Raman signal based on spin-orbit interaction of light. *Physical Review Letters* **123,** 183903 (2019).

219. Gong, S.-H., Komen, I., Alpeggiani, F. & Kuipers, L. Nanoscale optical addressing of valley pseudospins through transverse optical spin. *Nano Letters* **20,** 4410–4415 (2020).

220. Liu, W. *et al.* Generation of helical topological exciton-polaritons. *Science* **370,** 600–604 (2020).

221. Wang, J. *et al.* Routing valley exciton emission of a WS_2 monolayer via delocalized Bloch modes of in-plane inversion-symmetry-broken photonic crystal slabs. *Light: Science & Applications* **9,** 148 (2020).

222. Woo, A., Sung, J. & Gong, S.-H. Long-range directional transport of valley information from transition metal dichalcogenides via a dielectric waveguide. *Opt. Express* **29,** 10688–10697 (2021).

223. Boriskina, S. V. *et al.* Losses in plasmonics: from mitigating energy dissipation to embracing loss-enabled functionalities. *Adv. Opt. Photon.* **9,** 775–827 (2017).

224. Castellanos-Gomez, A. *et al.* Van der Waals heterostructures. *Nature Reviews Methods Primers* **2,** 58 (2022).

225. Frisenda, R. *et al.* Recent progress in the assembly of nanodevices and van der Waals heterostructures by deterministic placement of 2D materials. *Chemical Society Reviews* **47,** 53–68 (2018).

226. Wang, L. *et al.* One-dimensional electrical contact to a two-dimensional material. *Science* **342,** 614–617 (2013).

227. Purdie, D. G. *et al.* Cleaning interfaces in layered materials heterostructures. *Nature Communications* **9,** 5387 (2018).

228. Liu, F. *et al.* Disassembling 2D van der Waals crystals into macroscopic monolayers and reassembling into artificial lattices. *Science* **367,** 903–906 (2020).

229. Mannix, A. J. *et al.* Robotic four-dimensional pixel assembly of van der Waals solids. *Nature Nanotechnology* **17,** 361–366 (2022).

230. Prasad, P. N. *Nanophotonics* (John Wiley & Sons, 2004).

231. Koenderink, A. F., Alù, A. & Polman, A. Nanophotonics: Shrinking light-based technology. *Science* **348,** 516–521 (2015).

232. O'Brien, J. L., Furusawa, A. & Vučković, J. Photonic quantum technologies. *Nature Photonics* **3,** 687–695 (2009).

233. Awschalom, D. D., Hanson, R., Wrachtrup, J. & Zhou, B. B. Quantum technologies with optically interfaced solid-state spins. *Nature Photonics* **12,** 516–527 (2018).

234. Wang, J., Sciarrino, F., Laing, A. & Thompson, M. G. Integrated photonic quantum technologies. *Nature Photonics* **14,** 273–284 (2020).

235. Baranov, D. G. *et al.* Nanophotonic engineering of far-field thermal emitters. *Nature Materials* **18,** 920–930 (2019).

236. Altug, H., Oh, S.-H., Maier, S. A. & Homola, J. Advances and applications of nanophotonic biosensors. *Nature Nanotechnology* **17,** 5–16 (2022).

237. Siew, S. Y. *et al.* Review of Silicon Photonics Technology and Platform Development. *J. Lightwave Technol.* **39,** 4374–4389 (2021).

238. Boes, A. *et al.* Lithium niobate photonics: Unlocking the electromagnetic spectrum. *Science* **379,** eabj4396 (2023).

239. Lukin, D. M., Guidry, M. A. & Vučković, J. Integrated Quantum Photonics with Silicon Carbide: Challenges and Prospects. *PRX Quantum* **1,** 020102 (2020).

240. Castelletto, S. *et al.* Silicon carbide photonics bridging quantum technology. *ACS Photonics* **9,** 1434–1457 (2022).

241. Atatüre, M., Englund, D., Vamivakas, N., Lee, S.-Y. & Wrachtrup, J. Material platforms for spin-based photonic quantum technologies. *Nature Reviews Materials* **3,** 38–51 (2018).

242. Bradac, C., Gao, W., Forneris, J., Trusheim, M. E. & Aharonovich, I. Quantum nanophotonics with group IV defects in diamond. *Nature Communications* **10,** 5625 (2019).

243. Choy, J. T. *et al.* Integrated TiO_2 resonators for visible photonics. *Optics Letters* **37,** 539–541 (2012).

244. Devlin, R. C., Khorasaninejad, M., Chen, W. T., Oh, J. & Capasso, F. Broadband high-efficiency dielectric metasurfaces for the visible spectrum. *Proceedings of the National Academy of Sciences* **113,** 10473–10478 (2016).

245. Aarik, J., Aidla, A., Kiisler, A.-A., Uustare, T. & Sammelselg, V. Effect of crystal structure on optical properties of TiO_2 films grown by atomic layer deposition. *Thin Solid Films* **305,** 270–273 (1997).

246. Butcher, A. *et al.* High-Q Nanophotonic Resonators on Diamond Membranes using Templated Atomic Layer Deposition of TiO_2. *Nano Letters* **20,** 4603–4609 (2020).

247. Pelton, M. Modified spontaneous emission in nanophotonic structures. *Nature Photonics* **9,** 427–435 (2015).

248. Kino, G. S. & Corle, T. R. *Confocal scanning optical microscopy and related imaging systems* (Academic Press, 1996).

249. Jonkman, J., Brown, C. M., Wright, G. D., Anderson, K. I. & North, A. J. Tutorial: guidance for quantitative confocal microscopy. *Nature Protocols* **15,** 1585–1611 (2020).

250. Kapitanova, P. V. *et al.* Photonic spin Hall effect in hyperbolic metamaterials for polarization-controlled routing of subwavelength modes. *Nature Communications* **5,** 3226 (2014).

251. High, A. A. *et al.* Visible-frequency hyperbolic metasurface. *Nature* **522,** 192–196 (2015).

252. Tang, L. *et al.* On-chip chiral single-photon interface: Isolation and unidirectional emission. *Physical Review A* **99,** 043833 (2019).

253. Barbone, M. *et al.* Charge-tuneable biexciton complexes in monolayer WSe_2. *Nature Communications* **9,** 3721 (2018).

254. Dey, P. *et al.* Gate-Controlled Spin-Valley Locking of Resident Carriers in WSe_2 Monolayers. *Physical Review Letters* **119,** 137401 (2017).

255. Rice, W. D. *et al.* Persistent optically induced magnetism in oxygen-deficient strontium titanate. *Nature Materials* **13,** 481–487 (2014).

256. Lalieu, M. L. M., Lavrijsen, R. & Koopmans, B. Integrating all-optical switching with spintronics. *Nature Communications* **10,** 110 (2019).

257. Ye, Z. *et al.* Efficient generation of neutral and charged biexcitons in encapsulated WSe_2 monolayers. *Nature Communications* **9,** 3718 (2018).

258. Li, Z. *et al.* Revealing the biexciton and trion-exciton complexes in BN encapsulated WSe_2. *Nature Communications* **9,** 3719 (2018).

259. Scuri, G. *et al.* Electrically Tunable Valley Dynamics in Twisted WSe_2/WSe_2 Bilayers. *Physical Review Letters* **124,** 217403 (2020).

260. Kulig, M. *et al.* Exciton Diffusion and Halo Effects in Monolayer Semiconductors. *Physical Review Letters* **120,** 207401 (2018).

261. Glazov, M. M. Quantum Interference Effect on Exciton Transport in Monolayer Semiconductors. *Physical Review Letters* **124,** 166802 (2020).

262. Zipfel, J. *et al.* Exciton diffusion in monolayer semiconductors with suppressed disorder. *Physical Review B* **101,** 115430 (2020).

263. Rivera, P. *et al.* Valley-polarized exciton dynamics in a 2D semiconductor heterostructure. *Science* **351,** 688–691 (2016).

264. Jin, C. *et al.* Imaging of pure spin-valley diffusion current in WS_2–WSe_2 heterostructures. *Science* **360,** 893–896 (2018).

265. Unuchek, D. *et al.* Valley-polarized exciton currents in a van der Waals heterostructure. *Nature Nanotechnology* **14,** 1104–1109 (2019).

266. Costache, M. V., Sladkov, M., Watts, S. M., van der Wal, C. H. & van Wees, B. J. Electrical Detection of Spin Pumping due to the Precessing Magnetization of a Single Ferromagnet. *Physical Review Letters* **97,** 216603 (2006).

267. Sanchez, O. L., Ovchinnikov, D., Misra, S., Allain, A. & Kis, A. Valley Polarization by Spin Injection in a Light-Emitting van der Waals Heterojunction. *Nano Letters* **16,** 5792–5797 (2016).

268. Žutić, I., Fabian, J. & Das Sarma, S. Spintronics: Fundamentals and applications. *Reviews of Modern Physics* **76,** 323–410 (2004).

269. Cadiz, F. *et al.* Exciton diffusion in WSe_2 monolayers embedded in a van der Waals heterostructure. *Applied Physics Letters* **112,** 152106 (2018).

270. Liu, E. *et al.* Gate Tunable Dark Trions in Monolayer WSe_2. *Physical Review Letters* **123,** 027401 (2019).

271. Datta, I. *et al.* Low-loss composite photonic platform based on 2D semiconductor monolayers. *Nature Photonics* **14,** 256–262 (2020).

272. Seol, M. *et al.* High-throughput growth of wafer-scale monolayer transition metal dichalcogenide via vertical ostwald ripening. *Advanced Materials* **32,** 2003542 (2020).

273. Huang, Y. *et al.* Universal mechanical exfoliation of large-area 2D crystals. *Nature Communications* **11,** 2453 (2020).

274. Seyler, K. L. *et al.* Signatures of moiré-trapped valley excitons in $MoSe_2/WSe_2$ heterobilayers. *Nature* **567,** 66–70 (2019).

275. Tran, K. *et al.* Evidence for moiré excitons in van der Waals heterostructures. *Nature* **567,** 71–75 (2019).

276. Jin, C. *et al.* Observation of moiré excitons in WSe_2/WS_2 heterostructure superlattices. *Nature* **567,** 76–80 (2019).

277. Ciarrocchi, A. *et al.* Polarization switching and electrical control of interlayer excitons in two-dimensional van der Waals heterostructures. *Nature Photonics* **13,** 131–136 (2019).

278. High, A. A., Novitskaya, E. E., Butov, L. V., Hanson, M. & Gossard, A. C. Control of Exciton Fluxes in an Excitonic Integrated Circuit. *Science* **321,** 229–231 (2008).

279. Liu, Y. *et al.* Electrically controllable router of interlayer excitons. *Science Advances* **6,** eaba1830 (2020).

280. Robert, C. *et al.* Spin/valley pumping of resident electrons in WSe_2 and WS_2 monolayers. *Nature Communications* **12,** 5455 (2021).

281. Guddala, S. *et al.* All-optical nonreciprocity due to valley polarization pumping in transition metal dichalcogenides. *Nature Communications* **12,** 3746 (2021).

282. Kim, K.-S. & Kivelson, S. A. Discovery of an insulating ferromagnetic phase of electrons in two dimensions. *Proceedings of the National Academy of Sciences* **118** (2021).

283. Regan, E. C. *et al.* Mott and generalized Wigner crystal states in WSe_2/WS_2 moiré superlattices. *Nature* **579,** 359–363 (2020).

284. Zhou, Y. *et al.* Bilayer Wigner crystals in a transition metal dichalcogenide heterostructure. *Nature* **595,** 48–52 (2021).

285. Wu, F., Lovorn, T., Tutuc, E. & MacDonald, A. H. Hubbard model physics in transition metal dichalcogenide moiré bands. *Physical Review Letters* **121,** 026402 (2018).

286. Knörzer, J. *et al.* Wigner crystals in two-dimensional transition-metal dichalcogenides: Spin physics and readout. *Physical Review B* **101,** 125101 (2020).

287. Ersfeld, M. *et al.* Unveiling valley lifetimes of free charge carriers in monolayer WSe_2. *Nano Letters* **20,** 3147–3154 (2020).

288. Plechinger, G. *et al.* Trion fine structure and coupled spin–valley dynamics in monolayer tungsten disulfide. *Nature Communications* **7,** 12715 (2016).

289. Chen, S.-Y., Goldstein, T., Taniguchi, T., Watanabe, K. & Yan, J. Coulomb-bound four-and five-particle intervalley states in an atomically-thin semiconductor. *Nature Communications* **9,** 3717 (2018).

290. Yu, H., Liu, G.-B., Gong, P., Xu, X. & Yao, W. Dirac cones and Dirac saddle points of bright excitons in monolayer transition metal dichalcogenides. *Nature Communications* **5,** 3876 (2014).

291. Wang, Z., Shan, J. & Mak, K. F. Valley-and spin-polarized Landau levels in monolayer WSe_2. *Nature Nanotechnology* **12,** 144–149 (2017).

292. Li, J. *et al.* Spontaneous valley polarization of interacting carriers in a monolayer semiconductor. *Physical Review Letters* **125,** 147602 (2020).

293. Li, J., Goryca, M., Choi, J., Xu, X. & Crooker, S. A. Many-body exciton and intervalley correlations in heavily electron-doped WSe_2 monolayers. *Nano Letters* **22,** 426–432 (2021).

294. Zhang, C., Wang, H., Chan, W., Manolatou, C. & Rana, F. Absorption of light by excitons and trions in monolayers of metal dichalcogenide MoS_2: Experiments and theory. *Physical Review B* **89,** 205436 (2014).

295. Wang, J. *et al.* Disorder of excitons and trions in monolayer $MoSe_2$. *The Journal of Chemical Physics* **157,** 211101 (2022).

296. Van Tuan, D., Shi, S.-F., Xu, X., Crooker, S. A. & Dery, H. Six-Body and Eight-Body Exciton States in Monolayer WSe_2. *Physical Review Letters* **129,** 076801 (2022).

297. Rousset, J.-G. *et al.* Relation between exciton splittings, magnetic circular dichroism, and magnetization in wurtzite $Ga_{1-x}Fe_xN$. *Physical Review B* **88,** 115208 (2013).

298. Fei, Z. *et al.* Two-dimensional itinerant ferromagnetism in atomically thin Fe_3GeTe_2. *Nature Materials* **17,** 778–782 (2018).

299. Huang, K. *Statistical Mechanics.* 470 (Wiley, 1963).

300. Stanciu, C. D. *et al.* All-optical magnetic recording with circularly polarized light. *Physical review letters* **99,** 047601 (2007).

301. Kirilyuk, A., Kimel, A. V. & Rasing, T. Ultrafast optical manipulation of magnetic order. *Reviews of Modern Physics* **82,** 2731 (2010).

302. Lambert, C.-H. *et al.* All-optical control of ferromagnetic thin films and nanostructures. *Science* **345,** 1337–1340 (2014).

303. Kimel, A. V. & Li, M. Writing magnetic memory with ultrashort light pulses. *Nature Reviews Materials* **4,** 189–200 (2019).

304. Kawakami, R. K. Spin amplification by controlled symmetry breaking for spin-based logic. *2D Materials* **2,** 034001 (2015).

305. Kim, K.-S., Murthy, C., Pandey, A. & Kivelson, S. A. Interstitial-Induced Ferromagnetism in a Two-Dimensional Wigner Crystal. *Physical Review Letters* **129,** 227202 (2022).

306. Calvera, V., Kivelson, S. A. & Berg, E. Pseudo-spin order of Wigner crystals in multivalley electron gases. *arXiv* **arXiv:2210.09326** (2022).

307. Huang, B. *et al.* Layer-dependent ferromagnetism in a van der Waals crystal down to the monolayer limit. *Nature* **546,** 270–273 (2017).

308. Gong, C. *et al.* Discovery of intrinsic ferromagnetism in two-dimensional van der Waals crystals. *Nature* **546,** 265–269 (2017).

309. Mak, K. F., Shan, J. & Ralph, D. C. Probing and controlling magnetic states in 2D layered magnetic materials. *Nature Reviews Physics* **1,** 646–661 (2019).

310. Liu, F. *et al.* Ultrafast time-resolved Faraday rotation in EuO thin films. *Physical Review Letters* **108,** 257401 (2012).

311. Sun, Q.-C. *et al.* Magnetic domains and domain wall pinning in atomically thin $CrBr_3$ revealed by nanoscale imaging. *Nature Communications* **12,** 1989 (2021).

312. Maletinsky, P. *et al.* A robust scanning diamond sensor for nanoscale imaging with single nitrogen-vacancy centres. *Nature Nanotechnology* **7,** 320–324 (2012).

313. Song, T. *et al.* Direct visualization of magnetic domains and moiré magnetism in twisted 2D magnets. *Science* **374,** 1140–1144 (2021).

314. Yu, X. *et al.* Real-space observation of a two-dimensional skyrmion crystal. *Nature* **465,** 901–904 (2010).

315. Schaibley, J. R. *et al.* Valleytronics in 2D materials. *Nature Reviews Materials* **1,** 1–15 (2016).

316. Sierra, J. F., Fabian, J., Kawakami, R. K., Roche, S. & Valenzuela, S. O. Van der Waals heterostructures for spintronics and opto-spintronics. *Nature Nanotechnology* **16,** 856–868 (2021).

317. Figotin, A. & Vitebsky, I. Nonreciprocal magnetic photonic crystals. *Physical Review E* **63,** 066609 (2001).

318. Bi, L. *et al.* On-chip optical isolation in monolithically integrated non-reciprocal optical resonators. *Nature Photonics* **5,** 758–762 (2011).

319. Shastri, B. J. *et al.* Photonics for artificial intelligence and neuromorphic computing. *Nature Photonics* **15,** 102–114 (2021).

320. Jalas, D. *et al.* What is–and what is not–an optical isolator. *Nature Photonics* **7,** 579–582 (2013).

321. Potton, R. J. Reciprocity in optics. *Reports on Progress in Physics* **67,** 717 (2004).

322. Asadchy, V. S., Mirmoosa, M. S., Díaz-Rubio, A., Fan, S. & Tretyakov, S. A. Tutorial on Electromagnetic Nonreciprocity and its Origins. *Proceedings of the IEEE* **108,** 1684–1727 (2020).

323. Dötsch, H. *et al.* Applications of magneto-optical waveguides in integrated optics. *JOSA B* **22,** 240–253 (2005).

324. Srinivasan, K. & Stadler, B. J. H. Review of integrated magneto-optical isolators with rare-earth iron garnets for polarization diverse and magnet-free isolation in silicon photonics. *Opt. Mater. Express* **12,** 697–716 (2022).

325. Elshaari, A. W., Pernice, W., Srinivasan, K., Benson, O. & Zwiller, V. Hybrid integrated quantum photonic circuits. *Nature Photonics* **14,** 285–298 (2020).

326. Fan, S., Shi, Y. & Lin, Q. Nonreciprocal photonics without magneto-optics. *IEEE Antennas and Wireless Propagation Letters* **17,** 1948–1952 (2018).

327. Sounas, D. L. & Alù, A. Non-reciprocal photonics based on time modulation. *Nature Photonics* **11,** 774–783 (2017).

328. Tian, H. *et al.* Magnetic-free silicon nitride integrated optical isolator. *Nature Photonics* **15,** 828–836 (2021).

329. Sohn, D. B., Örsel, O. E. & Bahl, G. Electrically driven optical isolation through phonon-mediated photonic Autler–Townes splitting. *Nature Photonics* **15,** 822–827 (2021).

330. Herrmann, J. F. *et al.* Mirror symmetric on-chip frequency circulation of light. *Nature Photonics* **16,** 603–608 (2022).

331. Lira, H., Yu, Z., Fan, S. & Lipson, M. Electrically driven nonreciprocity induced by interband photonic transition on a silicon chip. *Physical Review Letters* **109,** 033901 (2012).

332. Fang, K., Yu, Z. & Fan, S. Realizing effective magnetic field for photons by controlling the phase of dynamic modulation. *Nature Photonics* **6,** 782–787 (2012).

333. Tzuang, L. D., Fang, K., Nussenzveig, P., Fan, S. & Lipson, M. Non-reciprocal phase shift induced by an effective magnetic flux for light. *Nature Photonics* **8,** 701–705 (2014).

334. Kim, J., Kuzyk, M. C., Han, K., Wang, H. & Bahl, G. Non-reciprocal Brillouin scattering induced transparency. *Nature Physics* **11,** 275–280 (2015).

335. Fang, K. *et al.* Generalized non-reciprocity in an optomechanical circuit via synthetic magnetism and reservoir engineering. *Nature Physics* **13,** 465–471 (2017).

336. Kittlaus, E. A., Otterstrom, N. T., Kharel, P., Gertler, S. & Rakich, P. T. Non-reciprocal interband Brillouin modulation. *Nature Photonics* **12,** 613–619 (2018).

337. Sohn, D. B., Kim, S. & Bahl, G. Time-reversal symmetry breaking with acoustic pumping of nanophotonic circuits. *Nature Photonics* **12,** 91–97 (2018).

338. Kittlaus, E. A. *et al.* Electrically driven acousto-optics and broadband non-reciprocity in silicon photonics. *Nature Photonics* **15,** 43–52 (2021).

339. Shi, Y., Yu, Z. & Fan, S. Limitations of nonlinear optical isolators due to dynamic reciprocity. *Nature Photonics* **9,** 388–392 (2015).

340. Hua, S. *et al.* Demonstration of a chip-based optical isolator with parametric amplification. *Nature Communications* **7,** 13657 (2016).

341. Sounas, D. L., Soric, J. & Alù, A. Broadband passive isolators based on coupled nonlinear resonances. *Nature Electronics* **1,** 113–119 (2018).

342. Del Bino, L. *et al.* Microresonator isolators and circulators based on the intrinsic nonreciprocity of the Kerr effect. *Optica* **5,** 279–282 (2018).

343. Yang, K. Y. *et al.* Inverse-designed non-reciprocal pulse router for chip-based LiDAR. *Nature Photonics* **14,** 369–374 (2020).

344. Cao, Q.-T. *et al.* Reconfigurable symmetry-broken laser in a symmetric microcavity. *Nature Communications* **11,** 1136 (2020).

345. White, A. D. *et al.* Integrated passive nonlinear optical isolators. *Nature Photonics* **17,** 143–149 (2023).

346. Hu, X.-X. *et al.* Noiseless photonic non-reciprocity via optically-induced magnetization. *Nature Communications* **12,** 2389 (2021).

347. Kim, S., Sohn, D. B., Peterson, C. W. & Bahl, G. On-chip optical non-reciprocity through a synthetic Hall effect for photons. *APL Photonics* **6,** 011301 (2021).

348. Dostart, N., Gevorgyan, H., Onural, D. & Popović, M. A. Optical isolation using microring modulators. *Optics Letters* **46,** 460–463 (2021).

349. Kawaguchi, Y. *et al.* Optical isolator based on chiral light-matter interactions in a ring resonator integrating a dichroic magneto-optical material. *Applied Physics Letters* **118,** 241104 (2021).

350. Bogaerts, W. *et al.* Silicon microring resonators. *Laser & Photonics Reviews* **6,** 47–73 (2012).

351. Rosenberger, M. R. *et al.* Nano-"squeegee" for the creation of clean 2D material interfaces. *ACS Applied Materials & Interfaces* **10,** 10379–10387 (2018).

352. Khelifa, R. *et al.* Coupling interlayer excitons to whispering gallery modes in van der Waals heterostructures. *Nano Letters* **20,** 6155–6161 (2020).

353. Son, J. *et al.* Atomically precise graphene etch stops for three dimensional integrated systems from two dimensional material heterostructures. *Nature Communications* **9,** 3988 (2018).

354. Li, X. *et al.* Proximity Induced Chiral Quantum Light Generation in Strain-Engineered $WSe_2/NiPS_3$ Heterostructures. *arXiv* **arXiv:2203.00797** (2022).

355. Andersen, T. I. *et al.* Beam steering at the nanosecond time scale with an atomically thin reflector. *Nature Communications* **13,** 3431 (2022).

356. Peterson, E. *et al.* In-Vivo Control of Excitons in TMDs. *Bulletin of the American Physical Society* **67** (2022).

357. Chakravarty, S., Kivelson, S., Nayak, C. & Voelker, K. Wigner glass, spin liquids and the metal-insulator transition. *Philosophical Magazine B* **79,** 859–868 (1999).

358. Peng, H.-T., Nahmias, M. A., De Lima, T. F., Tait, A. N. & Shastri, B. J. Neuromorphic photonic integrated circuits. *IEEE Journal of Selected Topics in Quantum Electronics* **24,** 1–15 (2018).

359. Tait, A. N. *et al.* Microring weight banks. *IEEE Journal of Selected Topics in Quantum Electronics* **22,** 312–325 (2016).

360. Tait, A. N. *et al.* Neuromorphic photonic networks using silicon photonic weight banks. *Scientific Reports* **7,** 1–10 (2017).

361. Ríos, C. *et al.* In-memory computing on a photonic platform. *Science Advances* **5,** eaau5759 (2019).

362. Sebastian, A. *et al.* Tutorial: Brain-inspired computing using phase-change memory devices. *Journal of Applied Physics* **124,** 111101 (2018).

363. Duong, D. L., Yun, S. J., Kim, Y., Kim, S.-G. & Lee, Y. H. Long-range ferromagnetic ordering in vanadium-doped WSe_2 semiconductor. *Applied Physics Letters* **115,** 242406 (2019).

364. Zhang, F. *et al.* Monolayer vanadium-doped tungsten disulfide: a room-temperature dilute magnetic semiconductor. *Advanced Science* **7,** 2001174 (2020).

365. Tiwari, S., Van de Put, M. L., Sorée, B. & Vandenberghe, W. G. Magnetic order and critical temperature of substitutionally doped transition metal dichalcogenide monolayers. *npj 2D Materials and Applications* **5,** 54 (2021).

366. Zomer, P. J., Guimarães, M. H. D., Brant, J. C., Tombros, N. & van Wees, B. J. Fast pick up technique for high quality heterostructures of bilayer graphene and hexagonal boron nitride. *Applied Physics Letters* **105,** 013101 (2014).

367. Laturia, A., Van de Put, M. L. & Vandenberghe, W. G. Dielectric properties of hexagonal boron nitride and transition metal dichalcogenides: from monolayer to bulk. *npj 2D Materials and Applications* **2,** 6 (2018).

368. Kataura, H. *et al.* Optical properties of single-wall carbon nanotubes. *Synthetic Metals* **103,** 2555–2558 (1999).

369. Hasdeo, E. H., Nugraha, A. R., Dresselhaus, M. S. & Saito, R. Breit-Wigner-Fano line shapes in Raman spectra of graphene. *Physical Review B* **90,** 245140 (2014).

370. Reding, J., Zhang, W. & Allam, J. Imaging excited-state dynamics in two-dimensional semiconductors with emerging ultrafast measurement techniques. *Accounts of Materials Research* **2,** 75–85 (2021).

APPENDIX A

SUPPLEMENTARY INFORMATION: ELECTRICAL CONTROL OF NANOPHOTONIC CHIRALITY

A.1 Device fabrication

Monolayer WSe_2 was mechanically exfoliated from bulk crystal (2D Semiconductors) onto SiO_2-Si substrates with 285 nm oxide thickness. Few-layer graphene (FLG) and thin hexagonal boron nitride (hBN) flakes were similarly exfoliated from bulk materials (HQ Graphene). Optical contrast and atomic force microscopy were used to verify that each flake was smooth and of appropriate thickness. After exfoliation, the hBN flakes were annealed in an inert argon atmosphere at 350 C for 30 minutes to release strain and remove tape residue.

Flakes were assembled into the gated monolayer WSe_2 heterostructure by a dry transfer technique [366]. Using a stamp of polycarbonate (PC) film on polydimethylsiloxane (PDMS), the top hBN layer (11 nm thick), FLG contact gate, monolayer WSe_2, and bottom hBN layer (17 nm thick) were picked up in sequence. The PC film with the heterostructure then was stamped onto the exfoliated FLG back gate on the Si/SiO_2 substrate. The PC film was dissolved in chloroform for 15 minutes at room temperature, leaving the bare heterostructure.

Ti/Au contacts were patterned on the exposed FLG flakes by photolithography and deposited by electron beam evaporation (5 nm/95 nm, respectively). Subsequently, a 10 nm encapsulation layer of Al2O3 was deposited by electron beam evaporation to protect the heterostructure and ensure a uniform surface for the photonics fabrication. The waveguide and grating couplers were patterned on top of the heterostructure using electron beam lithography [246]. A conformal TiO_2 layer was grown by atomic layer deposition into the device template. After etching the excess TiO_2 and stripping the PMMA template with NMP (heated to 80 C and soaking the sample overnight), the TiO_2 waveguide was left on top of the heterostructure. The sample then was annealed in ambient atmosphere at 250 C for 2 hr.

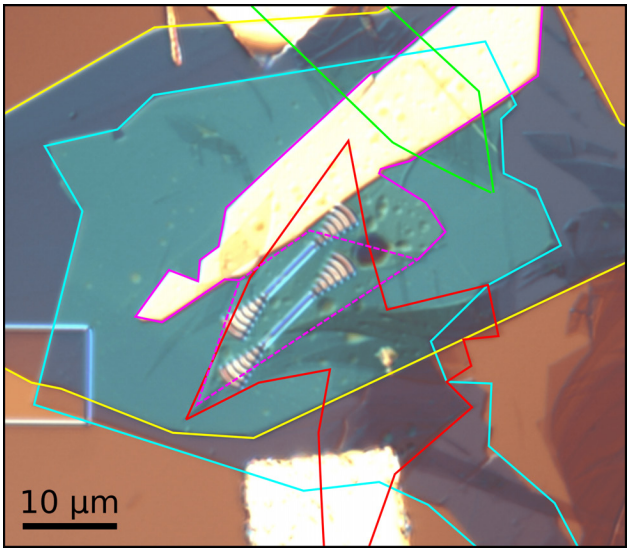

Figure A.1: Optical image of fabricated device. From top to bottom of the heterostructure: Top hBN layer (blue box), few-layer graphene contact (green box), WSe_2 monolayer (dashed purple box), bottom hBN layer (yellow box) and few-layer graphene back-gate (red box).

Lastly, a layer of PMMA (1.4 µm thick) was spin-coated onto the chip. The presented data were collected from the device shown in Fig. A.1. Measurements on an additional sample yield consistent results.

A.2 Optical measurements

The sample was kept in a closed-loop cryostat (Montana Instruments) running at 4 K for low temperature measurements in a reflection geometry using a 100X objective with an NA of 0.75. The spot size on the sample is measured with a CCD camera for a 660 nm excitation (Fig. A.2a). Fitting radial linecuts with gaussian profiles gives an average spot diameter of w = 495 ± 8 nm. A corresponding effective NA of 0.62 is found by comparing the spot profiles with that of a simulated focused gaussian beam (FDTD Solutions by Lumerical) (Fig. A.2b). Figure A.3 depicts the optical experimental configuration, where P1 and P2 are two fiber launch setups. They are used as excitation or collection channels depending on the experimental requirement. Two dual-axis galvanometers (GM1, GM2) are used to

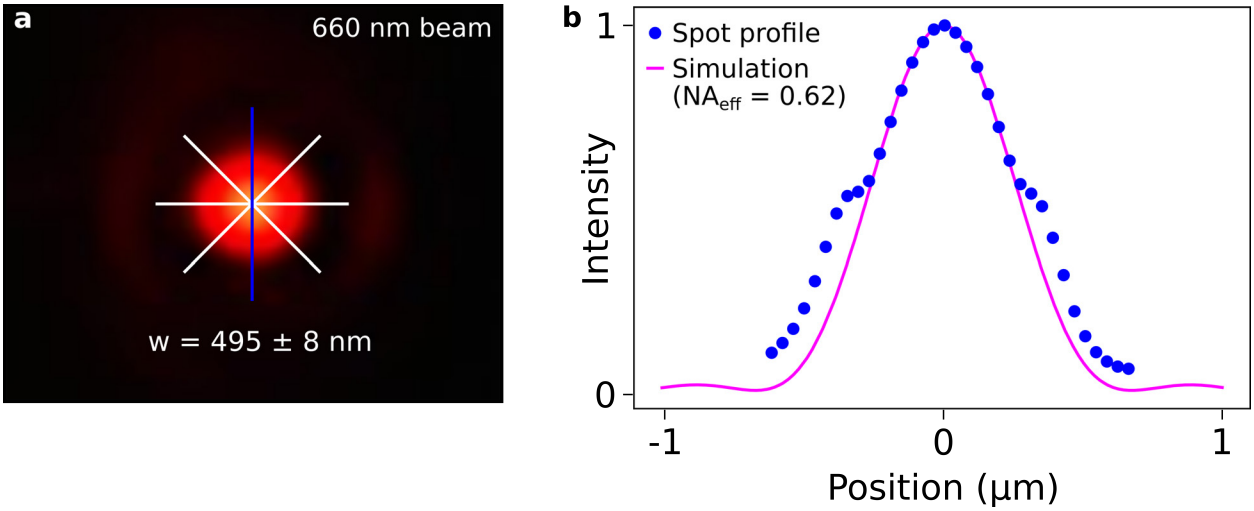

Figure A.2: Spot size calibration. a, Image of 660 nm excitation beam spot focused on the sample substrate. Intensity profiles extracted from the drawn linecuts are fitted to find a spot diameter of $w = 495 \pm 8$ nm. **b**, Overlay of a measured intensity profile (blue vertical linecut in **a**) with the simulated intensity profile of a focused gaussian source with NA = 0.62.

position the excitation and detection spots on the sample. A linear polarizer (LP) and quarter waveplate (QWP) after GM1 are used to realize circularly polarized excitation or detection. A single LP after GM2 is used to align the beam polarization to the grating coupler axis corresponding to the TE mode of the waveguide. For all experiments, a 660 nm diode laser was used for excitation. A 680 nm long-pass filter blocks the laser scattered into the detection channel. The detection channel is fiber-coupled to an APD (Excelitas) for spatial mapping measurements and to a spectrometer equipped with a deep cooling CCD (Princeton Instruments) for spectrally resolved measurements.

A.3 Simulations

Using a finite-difference-time-domain solver (FDTD Solutions by Lumerical), we simulated the electric field distribution for the fundamental TE mode of the waveguide. Figure A.4a illustrates the electric field intensity $|\boldsymbol{E}|^2$ over a cross-section of the waveguide-TMDC interface. The field is decomposed into in-plane $\sigma+$ circular $\boldsymbol{E_{\sigma+}} = (\boldsymbol{E_x} + i\boldsymbol{E_y})/\sqrt{2}$, in-plane $\sigma-$

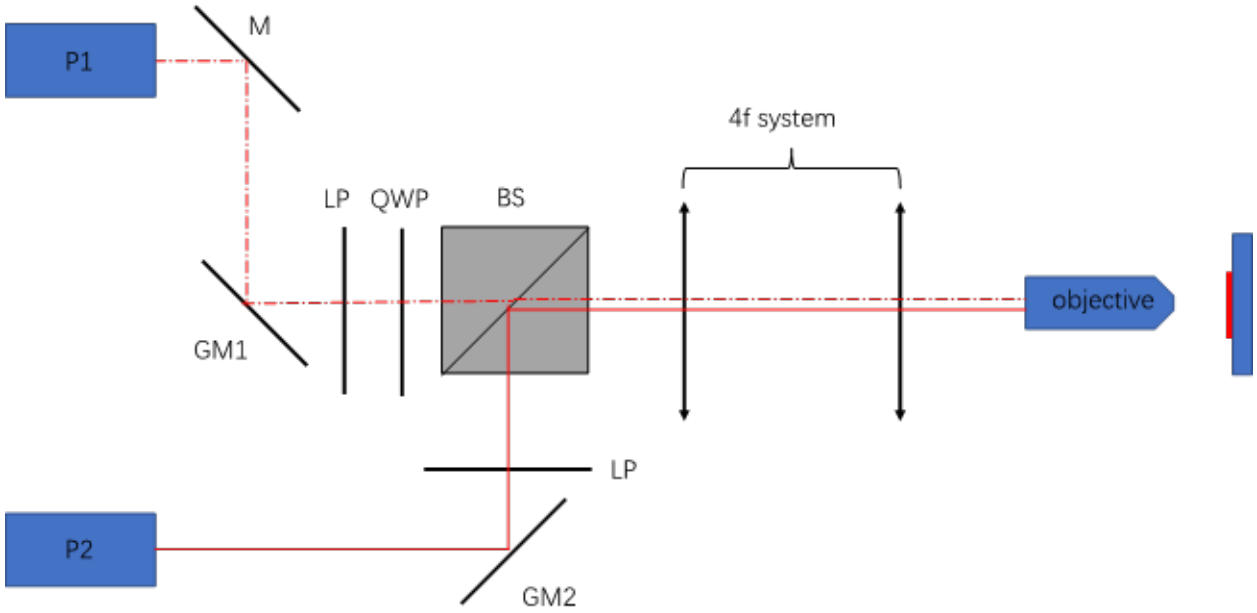

Figure A.3: Optical measurement configuration. For the chiral-directional coupling measurements, P1 is used as excitation, pumping the monolayer with circularly polarized light. P2 collects the out coupled PL. For the generation of diffusive valley(spin)-polarized excitonic states, P2 acts as excitation, coupling the pump laser into the waveguide. P1 collects the circularly polarized PL emission from the monolayer.

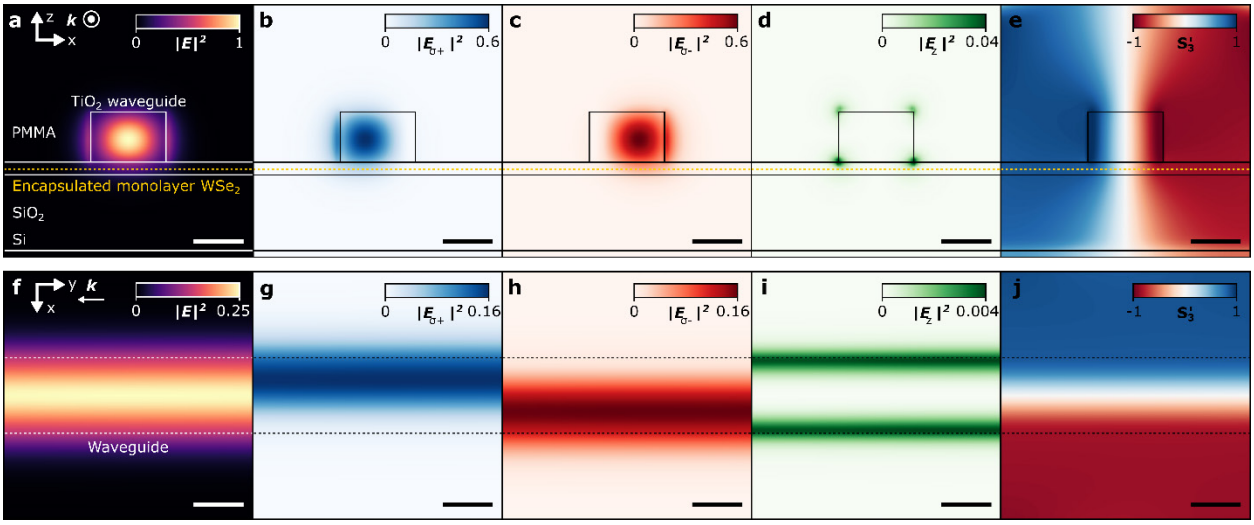

Figure A.4: Electric field distribution of waveguide mode. **a**, Electric field intensity for a cross-section of the propagating TE mode (wavevector k points out of the page). Intensity of field components projected along (**b**) $\sigma+$, (**c**) $\sigma-$, and (**d**) z basis directions. **e**, Reverse Stokes parameter S_3' shows localized, spatially separated regions of nearly circular polarization. **f-j**, Respective top-down views of TE mode (propagating leftward) in the monolayer plane. Dotted lines indicate the waveguide edges. All scale bars are 200 nm.

circular $\boldsymbol{E_{\sigma-}} = (\boldsymbol{E_x} - i\boldsymbol{E_y})/\sqrt{2}$, and out-of-plane linear $\boldsymbol{E_z}$ polarization components. The intensities of the corresponding field components are shown in Figs. A.4b-d, respectively. The mode polarization is characterized by the reverse Stokes parameter:

$$S_3' = 2\mathrm{Im}(\boldsymbol{E_x} \cdot \boldsymbol{E_y^*})/(|\boldsymbol{E_x}|^2 + |\boldsymbol{E_y}|^2) \tag{A.1}$$

$$= (|\boldsymbol{E_{\sigma+}}|^2 - |\boldsymbol{E_{\sigma-}}|^2)/(|\boldsymbol{E_{\sigma+}}|^2 + |\boldsymbol{E_{\sigma-}}|^2) \tag{A.2}$$

which is plotted in Fig. A.4e. Figures A.4f-j illustrate the field distribution in the plane of the monolayer WSe_2.

By simulating the electric field distributions both for the waveguide mode corresponding to our sample and for the focused far-field gaussian mode corresponding to our optical setup, we estimate the chiral-directional coupling at the interface. The approach we follow is detailed in reference [219] and discussed only briefly here. First, we estimate the maximum achievable CDCE. A focused gaussian source with NA = 0.62 is injected normal to the

device model with a global circular polarization (either $\sigma+$ or $\sigma-$), representing the far-field excitation of the TMDC monolayer. In the plane of the monolayer, we simulate the field intensity distribution as well as the $\sigma+/-$ component of the field with the existence of the waveguide (Fig. A.5). The intensity spatial distributions $|\boldsymbol{E_{\sigma+}}|^2$ and $|\boldsymbol{E_{\sigma-}}|^2$ are proportional to the exciton concentrations excited in the K and K' valleys, respectively. Directional collection of emission into the waveguide depends on the local intensity of the matching circular field polarization of the propagating waveguide modes (Figs. A.4g,h). Therefore, by integrating the point-by-point product of the circular excitation and collection intensities across the monolayer, we can compute the CDCE for a fixed perpendicular displacement of the excitation from the waveguide. Sweeping this displacement enables a complete mapping of the chiral-directional coupling. Assuming perfect valley polarization ($P_v = 1$), the simulated CDCE reaches a maximum of $\sim$0.4 with only minor dependence on the dispersive broadening of the field distribution of the waveguide mode (Fig. A.6).

An advantage of this simulation approach is that it considers fully the near-field polarization profile of the far-field excitation, which varies non-trivially from its global circular polarization due to the finite NA of the objective and the device architecture. A disadvantage, particularly in the context of our results, is that it does not consider the effect of exciton diffusion – *i.e.*, the spatial distributions of the valley excitons will evolve between their excitation and emission, which is neglected in this analysis. With this limitation in mind, fitting our measured CDCE data to the simulated spatially varying results will provide a lower bound of the isolated interface performance. Additionally, we consider the effect of the imperfect valley polarizations of the excitonic states on the computed CDCE. Following the fitting method in reference [215] (Fig. A.7), we extract, for the negative trion state, an interface fidelity as high as $90 \pm 2\%$, comparable to those of previously reported interfaces [215, 218].

This simulation approach also yields the exciton spatial profile excited by the waveguide

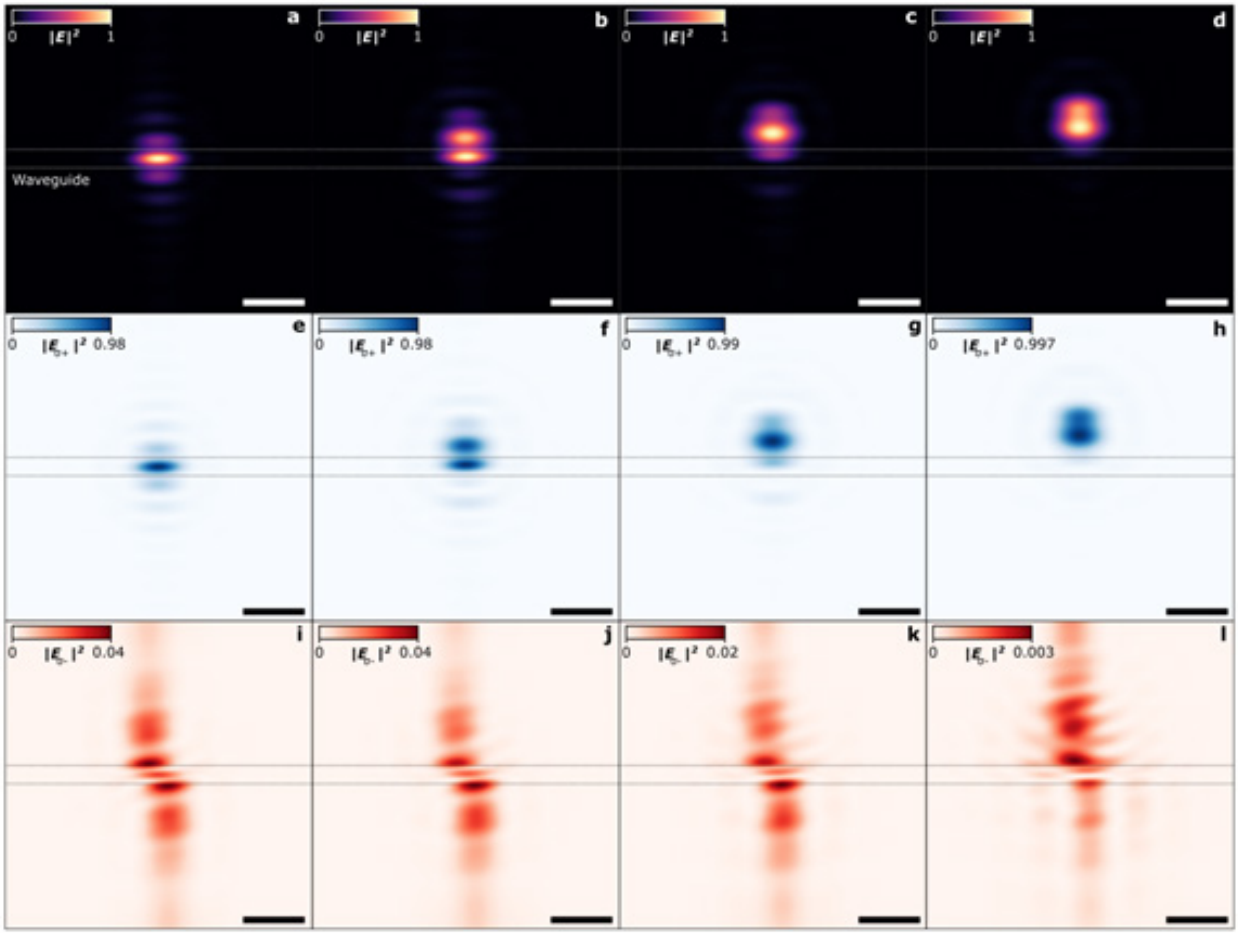

Figure A.5: Electric field distribution of far-field excitation. The electric field distribution of the focused far-field excitation laser is displayed in the plane of the monolayer for varying displacements from the waveguide center: (**a,e,i**) 0 nm, (**b,f,j**) 200 nm, (**c,g,k**) 400 nm, and (**d,h,l**) 600 nm. The polarization of the excitation is $\sigma+$. The total field intensity (**a-d**), $\sigma+$ component (**e-h**), and $\sigma-$ component (**i-l**) are shown. Scale bars are 1 µm.

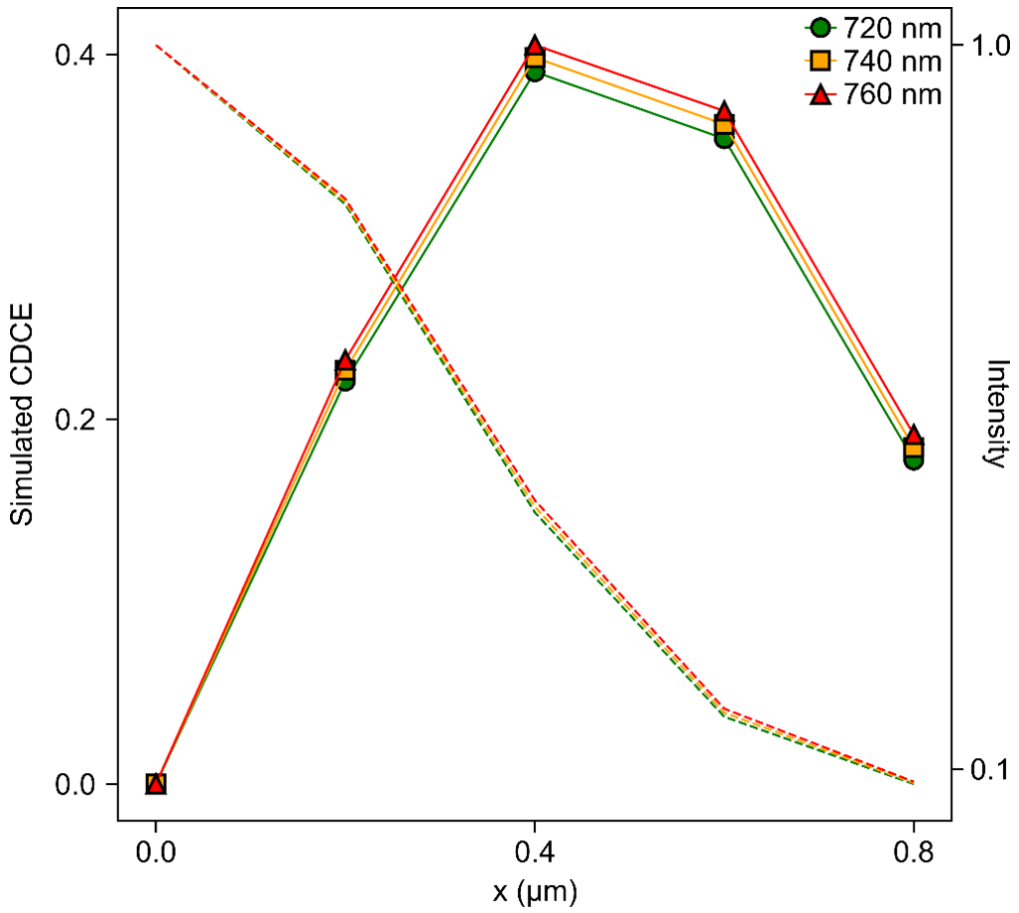

Figure A.6: Simulated CDCE considering dispersion of waveguide mode. CDCE (solid with markers) and total intensity (dashed) profiles calculated from simulations with waveguide modes at varying wavelengths and with $P_v = 1$.

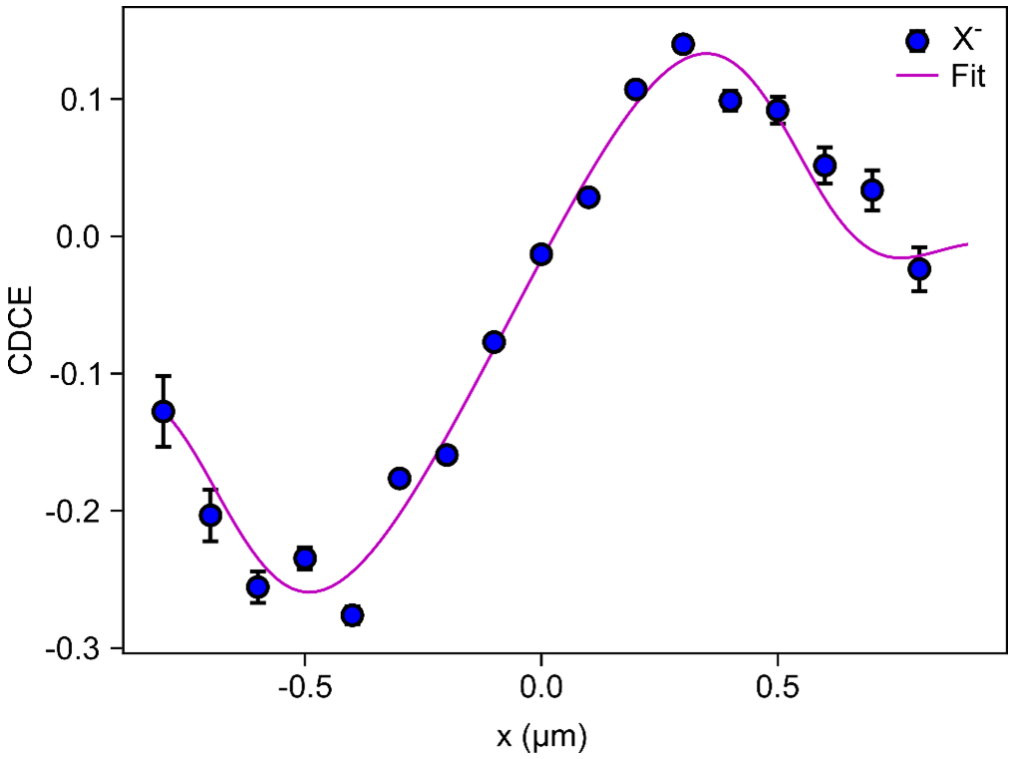

Figure A.7: Comparing negative trion CDCE to simulation. By fitting the measured CDCE profile of the negative trion state with the predicted profile from the simulated field distributions, an isolated interface fidelity as high as 90% is found. Data points are presented as mean values over the negative trion spectral range with error bars corresponding to 1SD of the background noise.

mode. By Lorentz reciprocity [215], we can repeat the analysis described above when we consider the case in which the waveguide mode excites the monolayer exciton populations and the focused far-field gaussian mode is used to collect the emission. The only necessary change is assigning the correct wavelengths to the excitation and collection modes, 660 nm and 740 nm respectively, to account for mild dispersion effects on the field distributions. As this model does not consider diffusion of excitons, its results offer a reference profile against which we can compare our measured excitonic spatial distributions (Fig. 5.9).

A.4 Interface Chiral-Directional Coupling

For reference, we include here the complete data set for the spatial and spectral characterizations of the chiral-directional coupling efficiency measurements discussed in the main text. Figure A.8 shows how CDCE maps are calculated from PL maps measured under different excitation polarizations. Figure A.9 demonstrates the directional collection of circularly polarized emission into the waveguide under no gate bias. Figure A.10 illustrates the electrical control of this chiral-directional coupling. The observed spatial variations in the PL and CDCE maps can be attributed to sample inhomogeneity across the monolayer material, distortions in the waveguide mode profile, and asymmetry of the excitation beam shape. Figure A.11 shows the spectrally resolved coupling for excitation linecuts across the waveguide.

A.5 Waveguide-driven Valley Polarization

For reference, we include here the complete data set for the spatial and spectral characterizations of the degree of circular polarization measurements discussed in the main text. Figure A.12 demonstrates circular emission from excitons directionally excited by the waveguide under no gate bias. Figure A.13 illustrates the electrical control of this circular emission. Figure A.14 shows the spectrally resolved circular emission for collection linecuts across the waveguide.

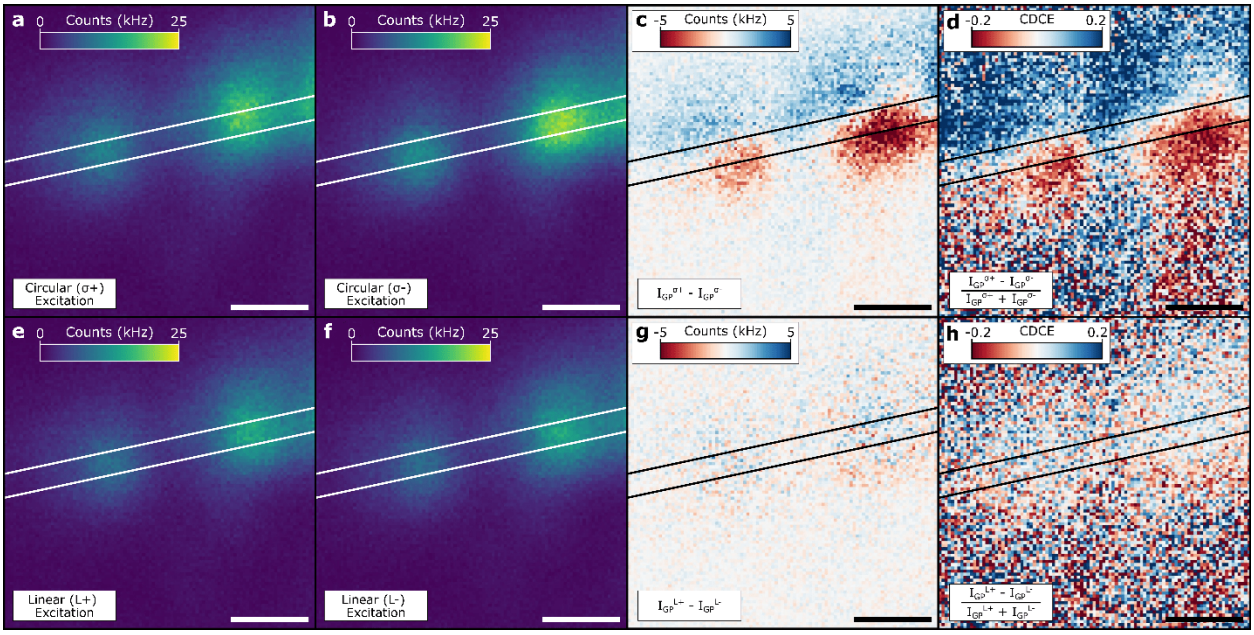

Figure A.8: Computing CDCE spatial maps from measured PL maps. a,b(e,f) PL intensity collected through the left grating port under far-field circular (linear) excitations scanned around the waveguide. Linear excitations L+ and L- are obtained with QWP angles 45 ° offset from those corresponding to $\sigma+$ and $\sigma-$ polarizations, respectively. **c(g)** Difference in collected intensity between $\sigma+$(L+) and $\sigma-$(L-) excitations. **d(h)** Computed chiral-directional coupling efficiencies under circular (linear) excitations. All scale bars are 1 µm.

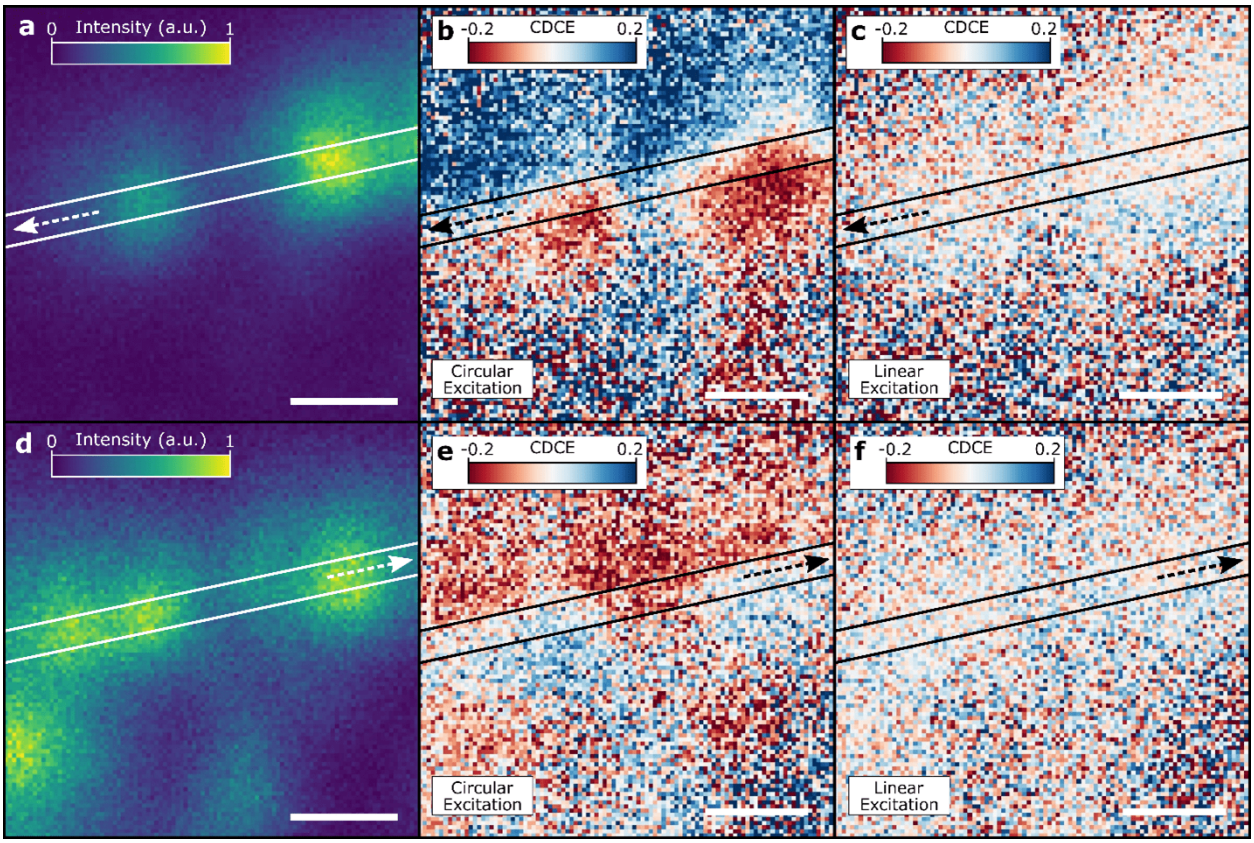

Figure A.9: Spatial maps of chiral-directional coupling. **a**(**d**) PL intensity collected through the left (right) grating port under far-field linear excitation scanned around the waveguide. **b**(**e**) Chiral-directional coupling efficiency measured from PL collected through the left (right) grating port under far-field circular excitations. **c**(**f**) Chiral-directional coupling efficiency measured from PL collected through the left (right) grating port under far-field linear excitations – i.e., excitation with QWP angles 45 ° offset from those corresponding to $\sigma+$ and $\sigma-$ polarizations. All scale bars are 1 µm.

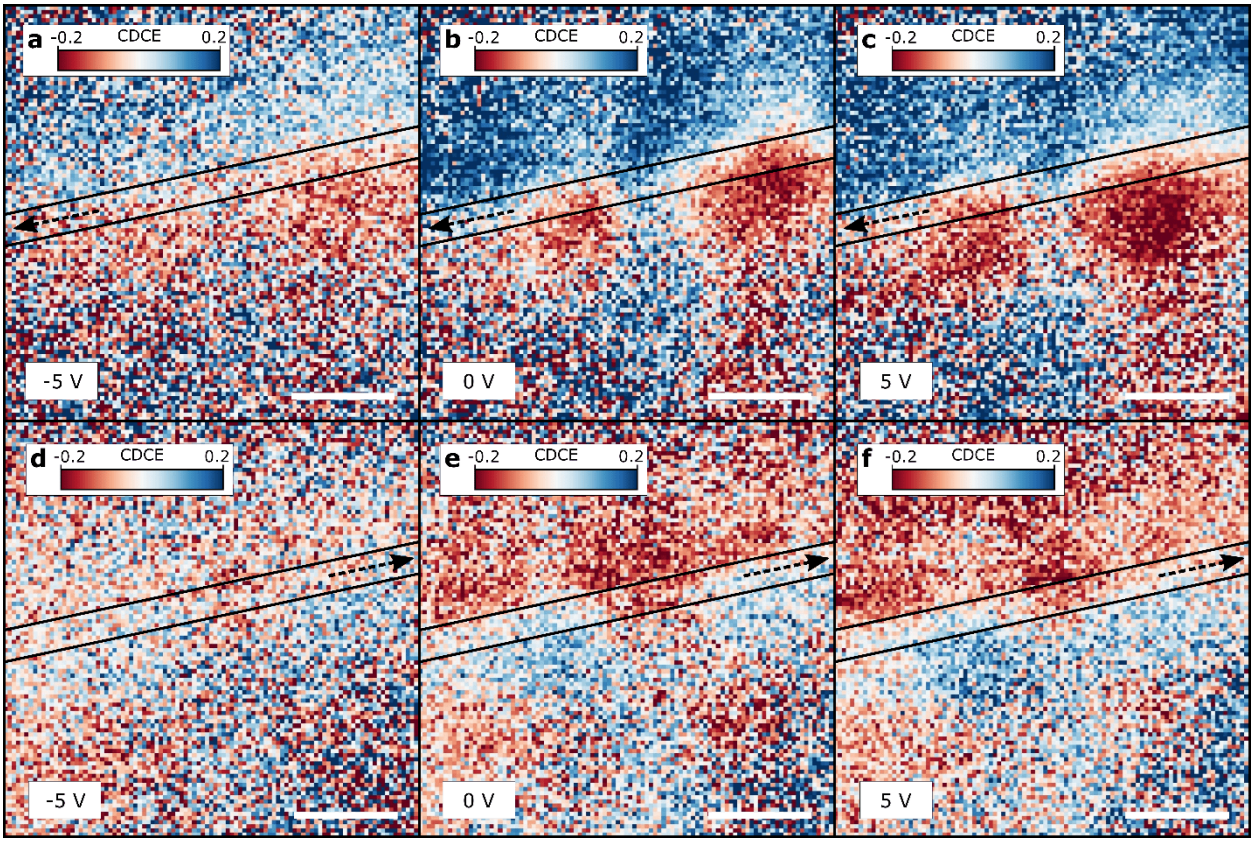

Figure A.10: Gate-tuned CDCE spatial maps. a-c(**d-f**), CDCE measured at left (right) port under gate biases of -5 V, 0 V, and +5 V, respectively. All scale bars are 1 µm.

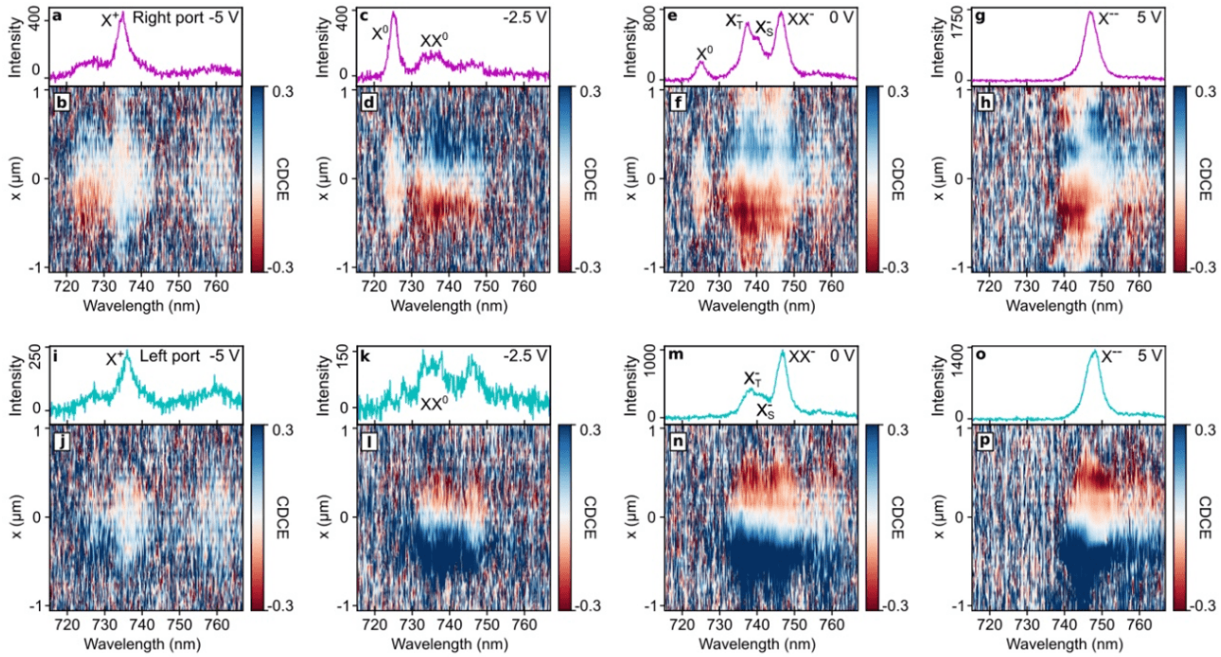

Figure A.11: Spectrally resolved CDCE. Columns correspond to spectral data collected under gate biases of (**a,b,i,j**) -5 V, (**c,d,k,l**) -2.5 V, (**e,f,m,n**) 0 V, and (**g,h,o,p**) 5 V. The top (bottom) row shows representative PL spectra collected through the right (left) port for on-waveguide excitation with relevant exciton peaks labeled, below which are displayed the wavelength-dependent CDCE as a function of excitation position.

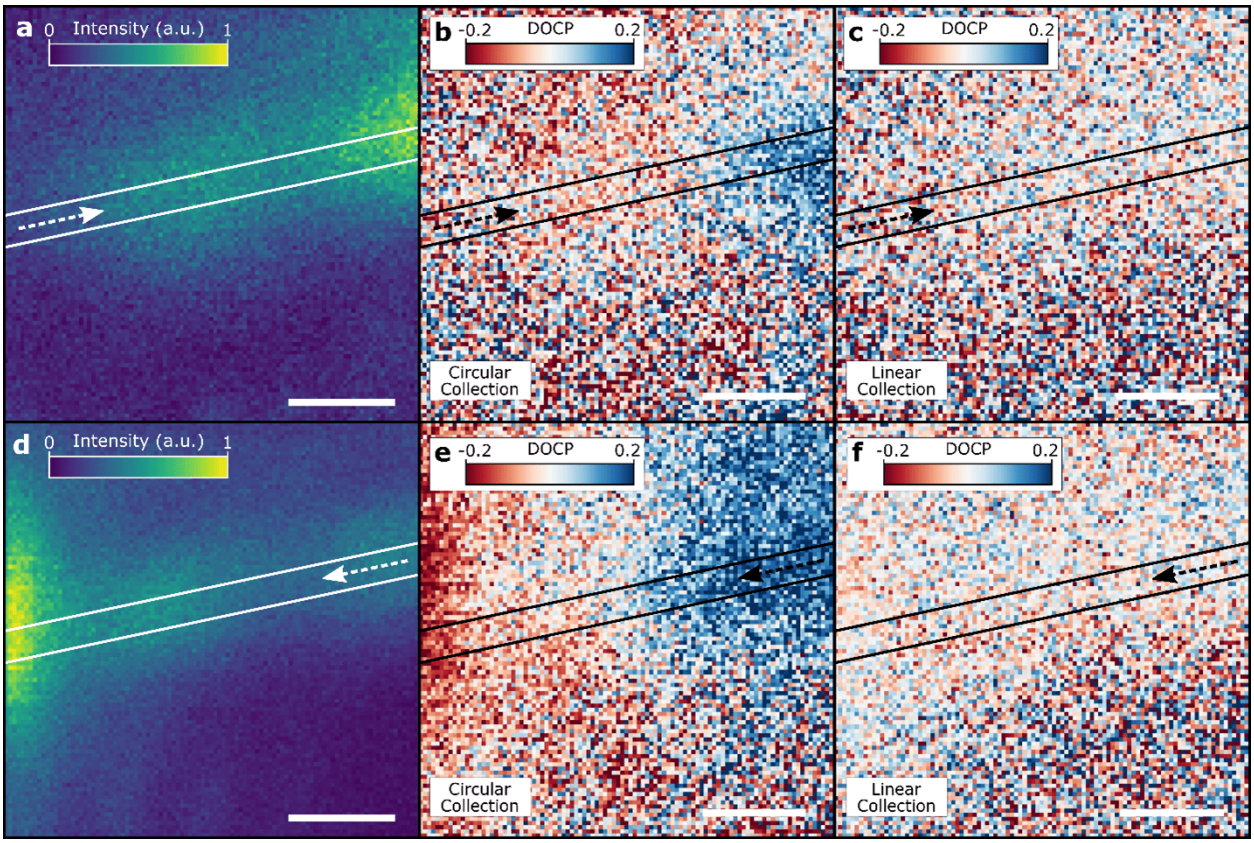

Figure A.12: Spatial maps of waveguide-pumped degree of circular polarization. **a**(**d**) Far-field PL intensity under linear collection for waveguide excitation through the left (right) grating port. **b**(**e**) Degree of circular polarization of far-field PL under circular collection for waveguide excitation through the left (right) grating port. **c**(**f**) Degree of circular polarization of far-field PL under linear collection for waveguide excitation through the left (right) grating port – *i.e.*, collection with QWP angles 45 ° offset from those corresponding to $\sigma+$ and $\sigma-$ polarizations. All scale bars are 1 µm.

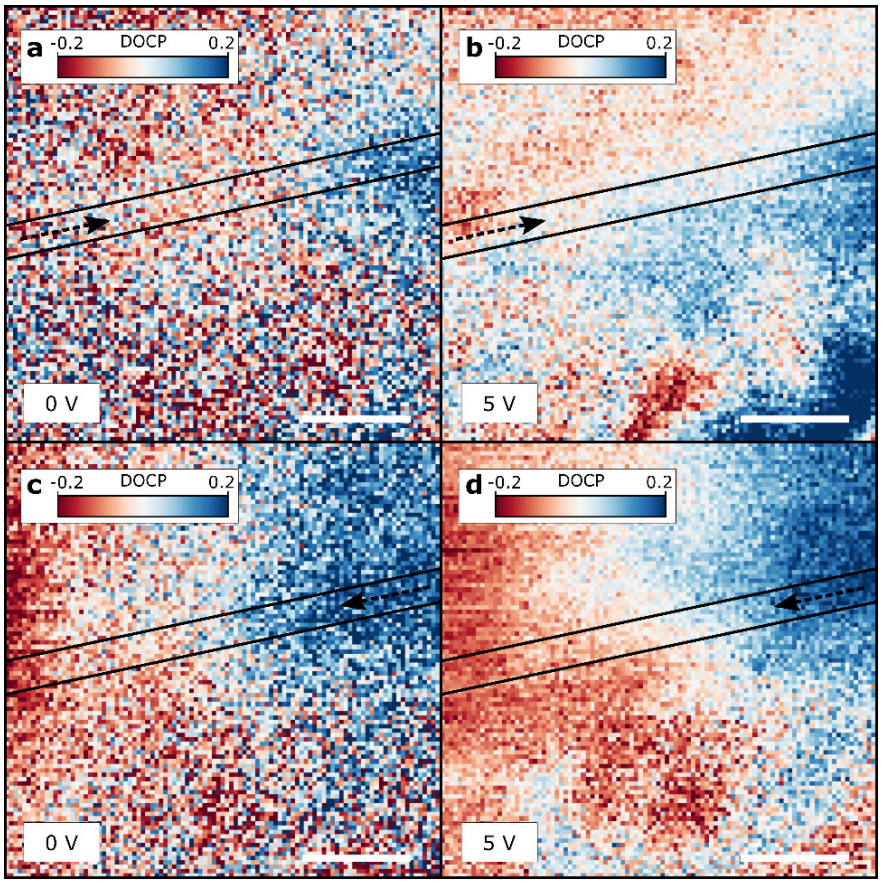

Figure A.13: Gated-tuned DOCP spatial maps. **a,b**(**c,d**), DOCP measured under left (right) port excitation for gate biases of 0 V and +5 V, respectively. All scale bars are 1 µm.

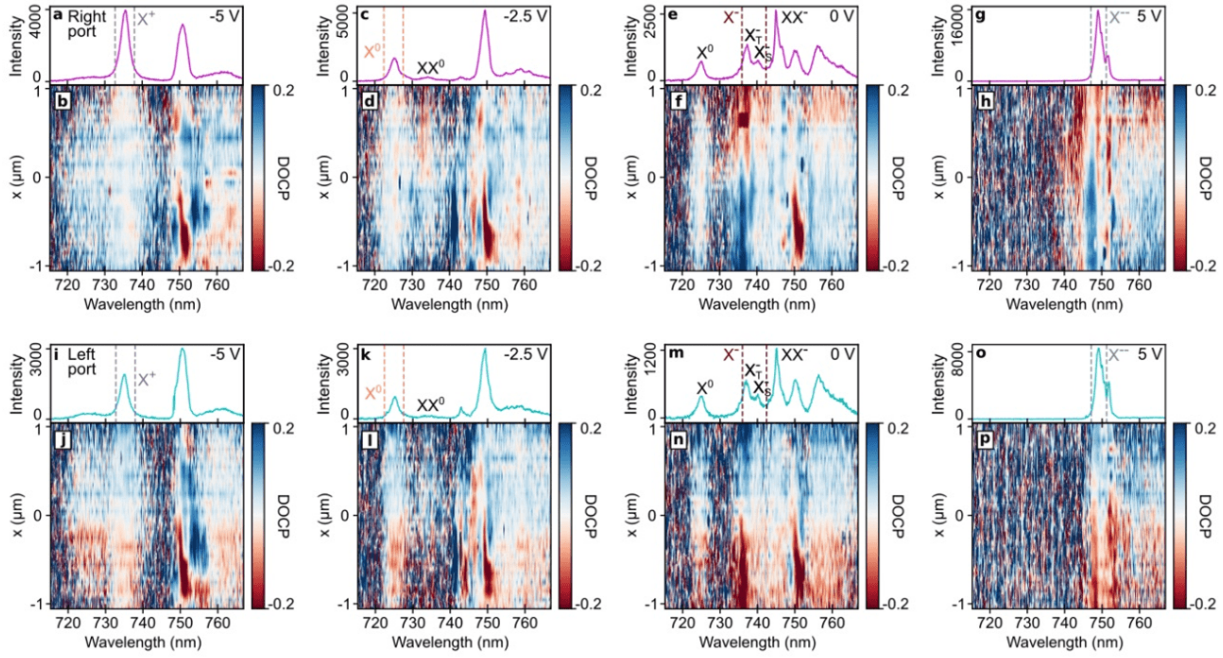

Figure A.14: Spectrally resolved DOCP. Columns correspond to spectral data collected under gate biases of (**a,b,i,j**) -5 V, (**c,d,k,l**) -2.5 V, (**e,f,m,n**) 0 V, and (**g,h,o,p**) 5 V. The top (bottom) row shows representative PL spectra collected on-waveguide when exciting through the right (left) port with relevant exciton peaks labeled, below which are displayed the wavelength-dependent DOCP as a function of collection position.

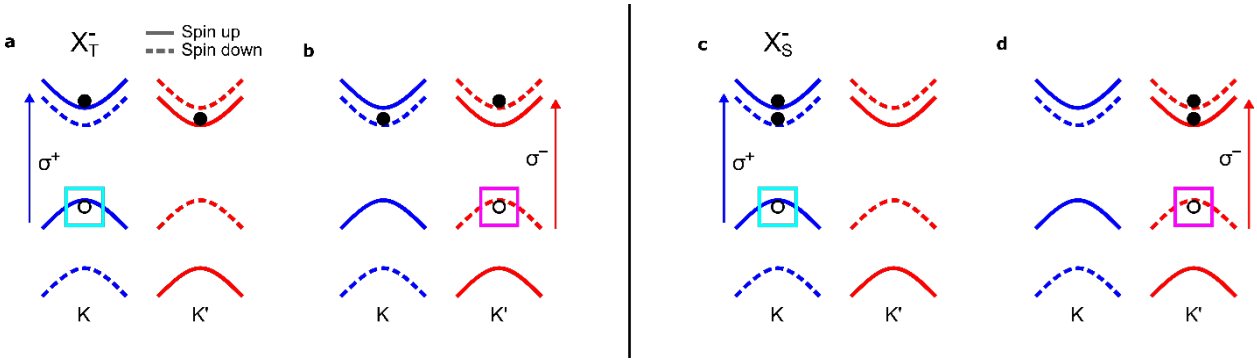

Figure A.15: Trion spin configurations. **a**, and **b**, Trion triplet in K and K' valleys. **c**, and **d**, Trion singlet in K and K' valleys. Dashed and solid lines indicate the electronic spin orientation. Valley-polarized holes are highlighted by the squares.

A.6 Trion Spin Configurations

For valley-polarized negative trions, there are two configurations, the so-called spin singlet and spin triplet states [290]. For both species, the electron-hole pair is polarized in one valley as the result of valley polarization. The excess electron of the triplet (singlet) trion is in the opposite (same) valley as the electron-hole pair, its spin aligning with (opposing) that of the paired electron, as shown in Fig. SA.15a,b(c,d). Since both trion species coexist in our sample, the electrons thus are not spin-polarized. In contrast, the paired holes are spin-polarized.

APPENDIX B

SUPPLEMENTARY INFORMATION: OPTICALLY STABILIZED MAGNETISM IN A 2D SEMICONDUCTOR

B.1 Sample fabrication

The monolayer tungsten diselenide (WSe_2), hexagonal boron nitride (hBN) and few-layer graphene (FLG) flakes are mechanically exfoliated from commercial bulk crystal (WSe_2 – 2D Semiconductor; hBN and FLG - HQGraphene) onto Si/SiO_2 chips. The thickness and cleanliness of the flakes are first examined with optical microscopy and then by atomic force microscopy (AFM) (Fig. B.1a). We used an all-dry transfer method1 to fabricate the hBN-encapsulated WSe_2 stack with FLG top gate and contact. Electrodes are patterned via photolithography, and then deposited by e-beam physical deposition with 5 nm Ti and 95 nm Au (Fig. B.1b). We also note that sample D2 has a layer of PMMA on top of the completed heterostructure.

B.2 Capacitor model of charge density estimation

To estimate the charge carrier density under electrostatic gating, we model the heterostructure as a parallel plate capacitor [135]: the FLG and monolayer WSe_2 flakes are the electrodes separated by the dielectric top hBN flake. The capacitance per unit area is given by $C = (\varepsilon_{hBN}\varepsilon_0)/d_{hBN}$. Using the relative permittivity of hBN $\varepsilon_{hBN} = 3.76$ [367] and the hBN thickness $d_{hBN} = 11.5$ nm, we find $C \approx 290$ nF cm^{-2}. The carrier density as a function of gate voltage is given by $n(V_g) = C \times (V_g - V_0)$, where V_0 is the gate voltage corresponding to the intrinsic regime with no carrier doping. By comparison with the neutral exciton feature in reflection (Fig. 6.1c), we approximate $V_0 = -0.5$ V.

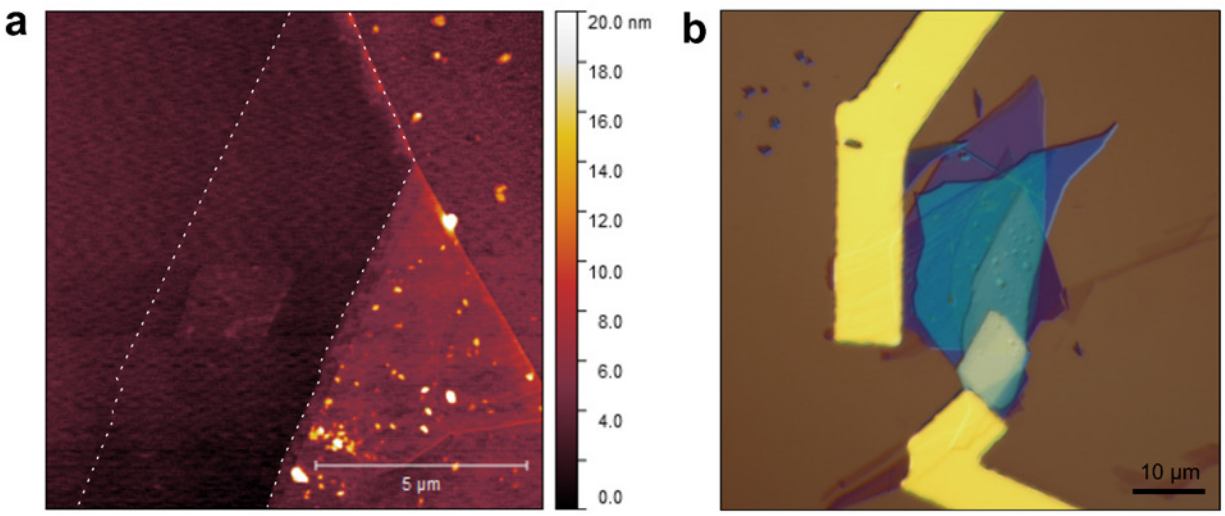

Figure B.1: Sample fabrication. **a**, AFM image of the WSe_2 flake on Si/SiO_2 chip with monolayer region outlined. **b**, Optical microscope image of the full heterostructure D1 with patterned contacts.

B.3 Optical measurement setup

The samples were kept in a closed loop cryostat (Montana Instruments) at 4 K during the experiment unless otherwise claimed. The optical setup is depicted in Fig. B.2. The two galvo mirrors control the pump and probe beam independently to realize spatial scans. We use a 660 nm diode laser (Thorlabs) as the optical pump exciting through port 3 with a band pass filter to spectrally clean the pump laser. A supercontinuum laser (YSL Photonics) is deployed as the broadband probe sent through port 1. The reflection of the supercontinuum from the sample is collected by port 2 and fiber coupled to a spectrometer with CCD (Teledyne Princeton Instruments) to realize spectrally resolved reflection measurements. The polarizations of each beam are independently controlled by linear polarizers and half-wave plates to allow different pump/probe polarization combinations.

To map the photoluminescence (PL) from the sample (Fig. 6.3a), we use ports 1 and 2 as the pump and collection channels, respectively. The same 660 nm diode laser is used for pumping. The PL signal is collected from port 2 and detected by an APD (Excelitas).

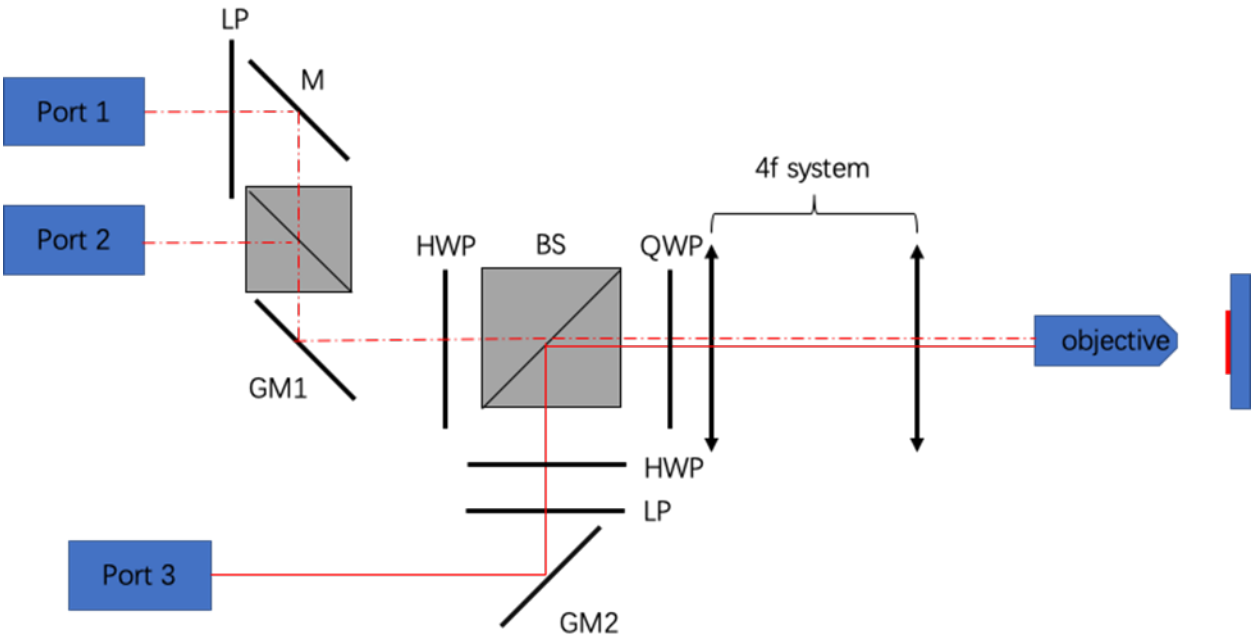

Figure B.2: Optical setup. Setup components are: Port – fiber launcher, M – mirror, GM – Galvo mirror, LP – linear polarizer, HWP – half-wave plate, QWP – quarter-wave plate, BS – beam splitter, 4f system – lens pair, objective – NA = 0.75.

By scanning galvo mirror 1, the co-localized pump and collection are simultaneously moved across the sample, realizing the PL mapping.

In time resolved measurements, we use a 633 nm pulsed diode laser with pulse duration of 5 ns and repetition rate of 50 kHz as the pump at port 3 and a tunable CW Ti:sapphire laser as the probe at port 1 with sub-nW power. The probe is tuned to the triplet trion resonance and the reflection is collected at port 2 with an APD (Excelitas). Time correlation between the probe and pump is measured by a time tagger (Qutag).

B.4 Line shape analysis

To estimate the valley/spin polarization of the free carriers, we extract the total oscillator strength of the trions in the two valleys. By comparing the oscillator strengths, we approximate the relative density of states in each valley, which give an estimation of the polarization

of the free carriers [84, 294].

The reflection contrast corresponding to the two trion features from Figure 6.2b is depicted in Figure B.3, which shows an asymmetric Fano-like line shape. The reflection contrast is given by $RC = R/R_{ref} - 1$, where R is the bare reflectivity (Fig. 6.2b) and R_{ref} is a reference reflectivity where the trion oscillator strengths disappear, under large gate bias or in the intrinsic region [101]. Such spectra can be captured by a two-peak Breit-Wigner-Fano (BWF) line shape fitting:

$$I(\omega) = I_1 \frac{(1 + (\omega - \omega_1)/q_1\Gamma_1)^2}{1 + ((\omega - \omega_1)/\Gamma_1)^2} + I_2 \frac{(1 + (\omega - \omega_2)/q_2\Gamma_2)^2}{1 + ((\omega - \omega_2)/\Gamma_2)^2} + C \tag{B.1}$$

where $q_{1/2}$ is the parameter which captures the asymmetry of the line shape. When $1/q \to 0$, the function converges to the Lorentzian line shape, where $I_{1/2}$ is the amplitude, $\omega_{1/2}$ is the center energy, and $\Gamma_{1/2}$ is the linewidth [368, 369].

By fitting the RC to a superposition of BWF line shapes with two resonances corresponding to the singlet and triplet trions (Fig. B.3 lines), we extract the fitting parameters shown in table B.1. The oscillator strength of each resonance is proportional to the area of the Lorentzian line shape $A = I_0\Gamma$. By comparing the relative oscillator strengths for each state under co- and cross-circular pumping, we can estimate the ratio of the density of states in each valley. We take this ratio, 90:10 for the triplet trion, as the ratio between the valley-polarized spin states of the resident electrons. By similarly fitting pump-off RC spectra, balanced detection gives a polarization sensitivity as low as 3%.

B.5 Sample D2 characterization and comparison of temporal dynamics with diffusion

The temporal dynamics are measured on a different sample D2. Characteristic reflection spectra and CD spectra are shown in Figure B.4, which show similar features as sample

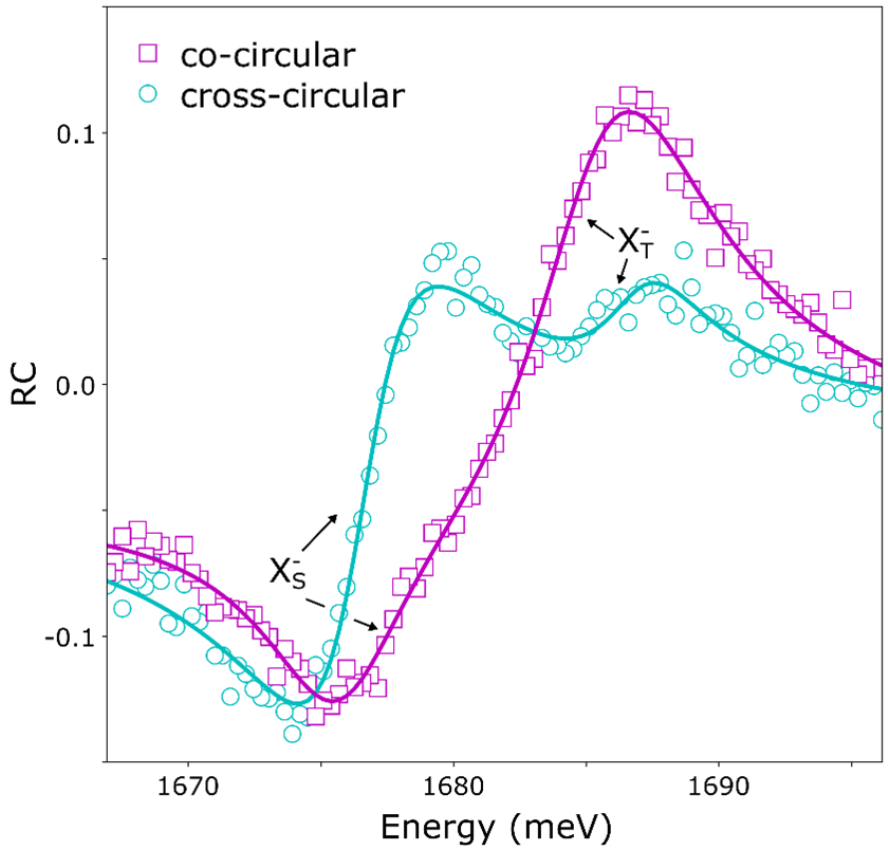

Figure B.3: Line shape fitting. Polarized reflection contrast spectra showing singlet (X_S^-) and triplet (X_T^-) trion features under optical pumping. The pink (blue) dots correspond to the probe being polarized co- (cross-) circular to the pump. BWF fittings are plotted. Note: T = 4 K, pump power is 7.8 µW, and pump-probe offset is 8 µm.

	Triplet					**Singlet**					
	I_1	ω_1 (meV)	Γ_1 (meV)	q_1	$A_1 = I_1\Gamma_1$	I_2	ω_2 (meV)	Γ_2 (meV)	q_2	$A_2 = I_2\Gamma_2$	C
Co-circular	0.151	1685.4	4.1	3.5	0.62	0.0005	1675.8	3.3	0.08	0.0016	-0.13
Cross-circular	0.035	1687.0	2.3	2.8	0.08	0.075	1676.5	2.7	0.9	0.20	-0.13
Ratio	~90:10					~99:1					
P_s	0.77					-0.98					

Table B.1: BWF fitting parameters.

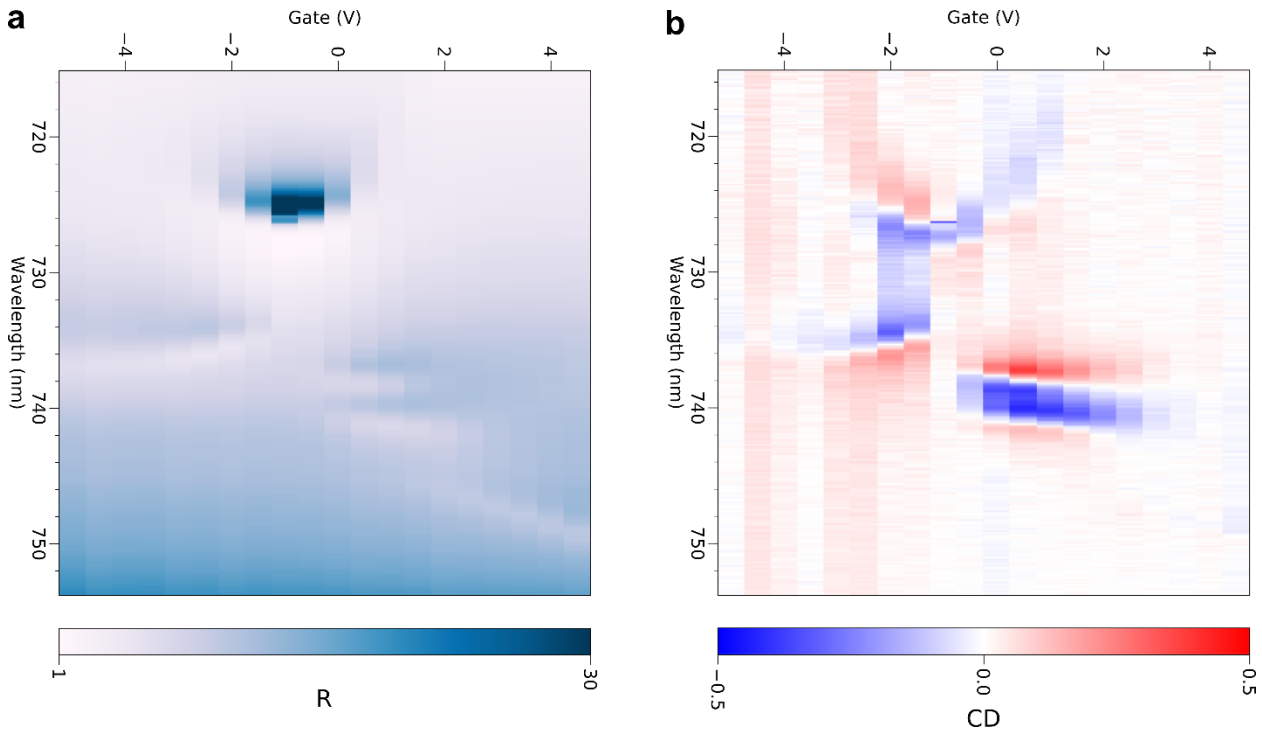

Figure B.4: Sample D2 characterization. Gate-dependent reflection (**a**) and CD spectra (**b**) at 4 K with a pump-probe separation of 3 µm and pump power of 7.8 µW.

D1 in main text Fig. 6.1. Using the time-resolved, circularly polarized differential reflection measurement results at selected positions with different distances from the pump, we compare the temporal profile with that predicted in a diffusion picture. Here the analysis is performed on an additional dataset taken from different pump and probe positions than presented in main text Figure 6.4.

The spin polarization under pulsed pumping is extracted from the differential reflection in the CW pumping case:

$$P_s^{pulse}(t) = \frac{\Delta R^{pulse}(\lambda, t)}{\Delta R^{cw}(\lambda)} P_s^{cw} \tag{B.2}$$

P_s^{cw} is the spin polarization found from the line shape analysis of the oscillator strength transfer under CW pumping. $\Delta R^{pulse/cw}$ is the differential reflection at wavelength of interest λ under pulsed/CW pumping. A clear build-up process is measured as a rising edge in the time resolved measurements as shown in Figure B.5a for a pump-probe separation of

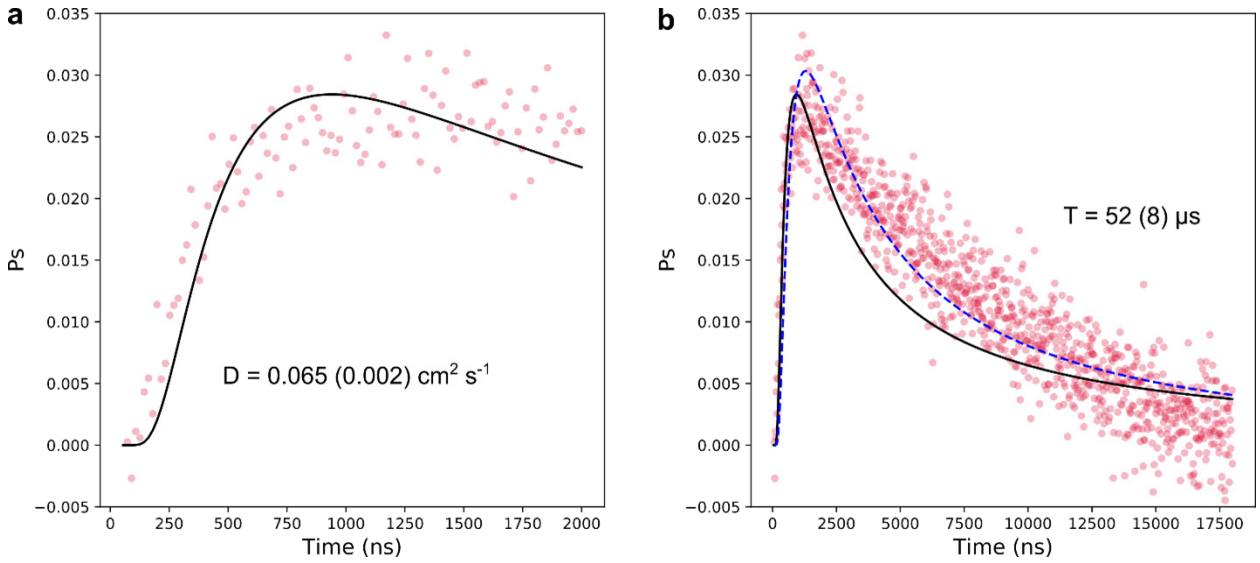

Figure B.5: Time resolved measurement for point 4.78 μm away from pump. a, Sample D2: Rising edge profile with two-dimensional diffusion-decay model fitting (black line). **b**, Fitting the full-time range with $D = 0.065$ cm^{2}s^{-1} from the rising edge (black solid line) fitting yields lifetimes beyond a second (*i.e.*, no decay). Fitting both D and T (blue dashed line) yields $D = 0.045$ cm^{2}s^{-1} and $T = 52$ μs. Fitting uncertainties are in parentheses. Note: T = 4 K, average pump power is 2 nW at a repetition rate of 50 kHz, and gate voltage is 0.5 V ($n_e \approx 2 \times 10^{12}$cm^{-2}).

4.87 μm. Thus, we tentatively fit the temporal profile with a two-dimensional diffusion-decay model [264]:

$$P_s(x,t) = \frac{\sigma_0^2\ P_s^0}{\sigma_0^2 + 4Dt} \exp\left\{\frac{-x^2}{\sigma_0^2 + 4Dt}\right\} \exp\left\{\frac{-t}{T}\right\} \tag{B.3}$$

where D is the diffusion constant, T is the spin polarization lifetime, and $\sigma_0 = 0.78$ μm is the spatial convolution of the pump and probe beam sizes.

While the fitting cannot accurately capture the full temporal evolution of the spin profile (Fig. B.5b), the diffusion constant extracted by fitting the rising edge (Fig. B.5a) provides an estimate of $D \approx 0.065$ cm^{2}s^{-1} for the propagation speed of the spin order formation. This value is significantly lower than the measured diffusion constant in previous research [264], indicating a different mechanism behind the spin order propagation. The decay trend gives a spin lifetime of $T \approx 52$ μs (Fig. B.5b).

Following the analysis in the main text (Fig. 6.4), we compare the measured temporal

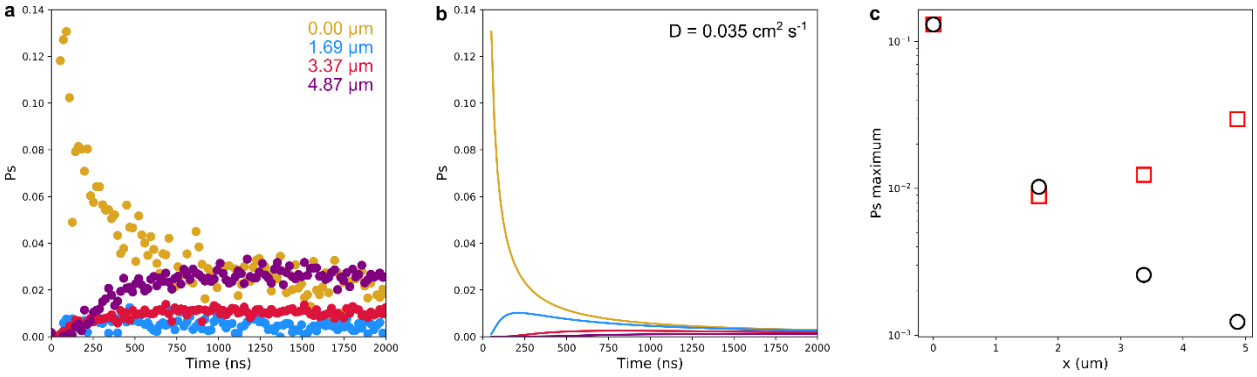

Figure B.6: Additional time resolved data. **a**, Sample D2: Time resolved measurement for different pump-probe separations. **b**, Simulation of diffusion model with diffusion constant $D = 0.035$ cm^{2}s^{-1} for different separations. **c**, Comparison between the measured (red squares) and simulated (black circles) maximum spin polarization. Note: T = 4 K, average pump power is 2 nW at a repetition rate of 50 kHz, and gate voltage is 0.5 V ($n_e \approx 2 \times 10^{12}$cm^{-2}).

profiles for various pump-probe separations with those of the diffusion model (Fig. B.6). Ignoring decay, diffusive transport of a fixed number of spins away from a local source should lead to an approximately $1/r^2$ dependence in the peak polarization measured a distance r from the source. This geometric constraint suggests a rapid fall off in the maximum spin polarization away from the pump, as seen in Figure B.6b for a diffusion model with representative $D = 0.035$ cm^{2}s^{-1} and infinite lifetime. In contrast, the measured maximum polarization shows no systematic change as the offset varies, even increasing at larger distances (Fig. B.6a). As in Figure 6.4, the measured spin polarization is amplified by almost an order of magnitude compared to purely diffusive propagation (Fig. B.6c). The variations in maximum polarization can be attributed to local deviations in the dielectric environment or defects distributed across the sample [295]. The strength of the electron-electron interactions, which creates the ferromagnetic state, will vary throughout the sample due to these inhomogeneities. Correspondingly, the maximum spin polarization will also vary.

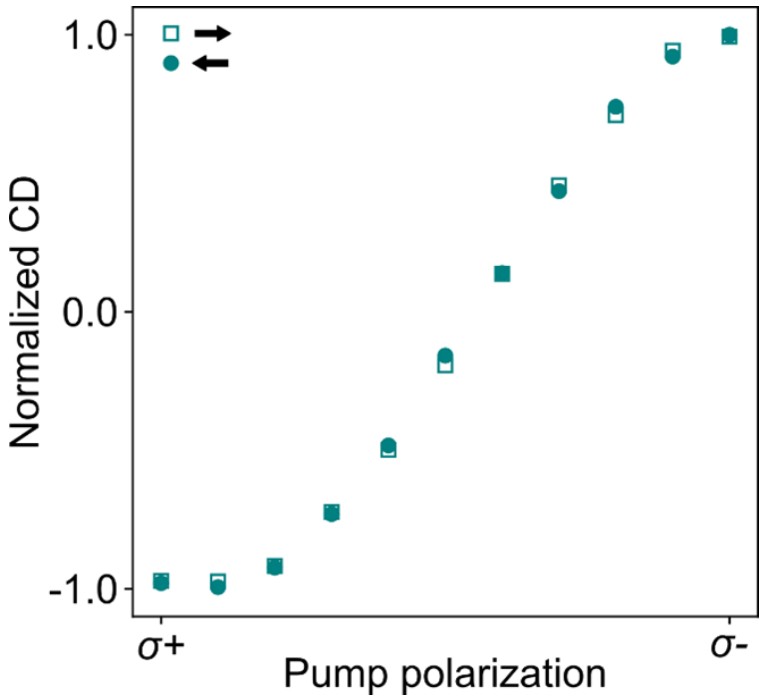

Figure B.7: Pump polarization sweep. Sample D1: Polarization dependence of singlet CD amplitude. Hollow squares (solid circles) correspond to sweeping the polarization from $\sigma+$ to $\sigma-$ ($\sigma-$ to $\sigma+$). Note: T = 4 K, pump power is 7.8 µW, pump-probe offset is 1.6 µm, and gate voltage is 0.5 V ($n_e \approx 2 \times 10^{12}\text{cm}^{-2}$).

B.6 Hysteresis check

In addition to sweeping the pump power (Fig. 6.6a), we test magnetic hysteresis in D1 by continuously varying the pump polarization in opposite directions. No observable hysteresis loop is observed (Fig. B.7). Similarly, previous measurements in monolayer MoS_2 do not observe hysteresis under an applied magnetic field [135].

B.7 Sample D3 characterization and temperature dependence

The temperature-dependent measurements (Fig. B.8) are performed on a third sample (D3). Figure B.8a shows gate-dependent reflection spectra at 4 K with a pump-probe separation of 2.2 µm, which display similar doping regimes as sample D1 (Fig. 6.1c). In the electron-doped region, strong CD signal is observed. Figure B.8b depicts the reflection and CD

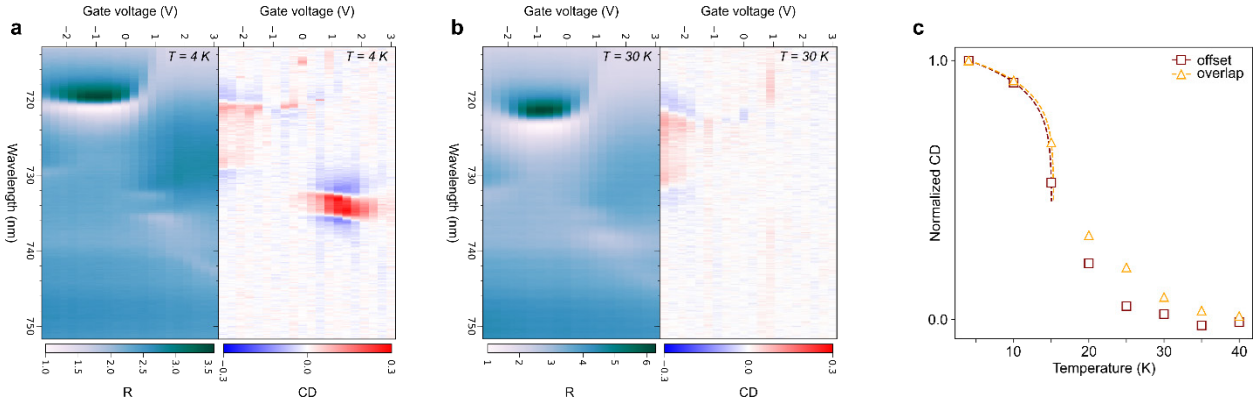

Figure B.8: Sample D3 characterization and temperature dependence. **a**, Gate-dependent reflection (left) and CD (right) spectra at 4 K with a pump-probe separation of 2.2 µm. **b**, Gate-dependent reflection (left) and CD (right) spectra at 30 K. **c**, Temperature dependence of triplet CD amplitude selected from gate-dependent CD spectra at gate voltage of 1.2 V ($n_e \approx 2.8 \times 10^{12}\text{cm}^{-2}$). Hollow squares (triangles) correspond to experimental data for offset (overlapping) pump and probe with respective fittings (dashed lines). Note: Pump power is 7.8 µW.

spectra at 30 K. While the electron-doped CD vanishes at this elevated temperature, the singlet and triplet trion features remain, confirming that the temperature dependence of the CD signal probes that of the spin polarization. Temperature dependent data was also taken with overlapped pump and probe. The CD amplitude shows a very similar trend as that with a 2.2 µm pump-probe offset (Fig. B.8c). The criticality fit $\alpha(T_c - T)^\beta$ is applied to the CD data [298], extracting a critical temperature $T_c = 15.0$ K (15.3 K) and a critical exponent $\beta = 0.113$ (0.106) for the offset (overlapping) pump-probe configuration. For the 2D Ising model, the expected critical exponent is $\beta = 0.125$.

B.8 Sample D4 characterization and comparison of temperature- and gate-dependent results with steady-state diffusion

Here, we test predictions of the spin diffusion model under CW pumping against additional experimental data taken from a fourth sample (D4) (Fig. B.9). In previous research [96], the spin lifetime of electrons is strongly dependent on the temperature and doping level. In a

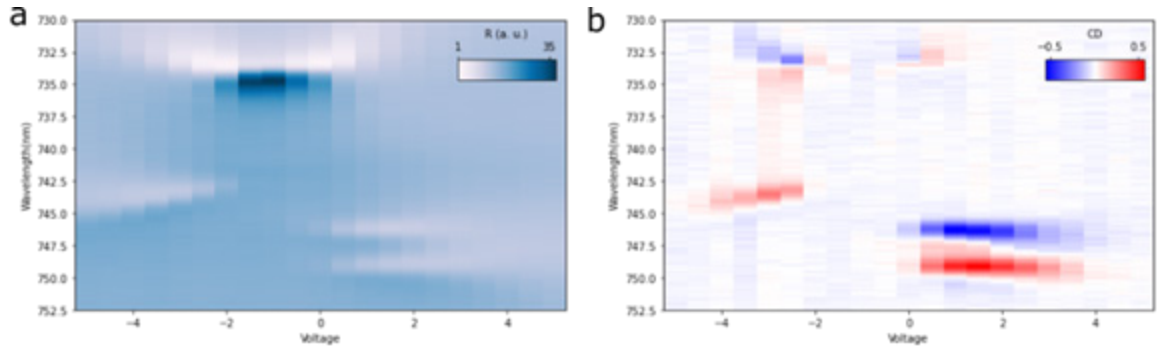

Figure B.9: Sample D4 characterization. Gate-dependent reflection (**a**) and CD spectra (**b**) at 4 K with a pump-probe separation of 2.5 µm and pump power of 7.8 µW.

simple diffusion model the spin diffusion length is directly correlated with the spin lifetime. Thus, within the diffusion model, the spatial profile of the CD signal would have a strong temperature and doping dependence. In FigureB.10, the spatial profiles of the CD signal at varying temperatures and doping levels are shown. The CD profiles uniformly decrease by an order of magnitude with no observable spatial contraction at elevated temperatures or increased doping. Thus, our observation is in stark contrast to the predictions of the diffusion model.

In a spin pumping model with a CW laser, the steady state spin polarization results from competition between the spin pumping rate and the spin decay rate. Within this model, if the spin decay rate increases at increasing temperature, the loss of spin polarization could be compensated by increasing the pumping rate. This can be understood with simple rate equations for a single pump in the K valley:

$$\frac{dN_+}{dt} = -GN_+ - \gamma(N_+ - N_-) \tag{B.4}$$

$$\frac{dN_-}{dt} = GN_+ - \gamma(N_- - N_+) \tag{B.5}$$

Where $N_{+(-)}$ are the number of electrons in the K (K') valley, G is the spin pumping rate which is linear to the pumping power, and γ is the intervalley scattering (spin decay) rate.

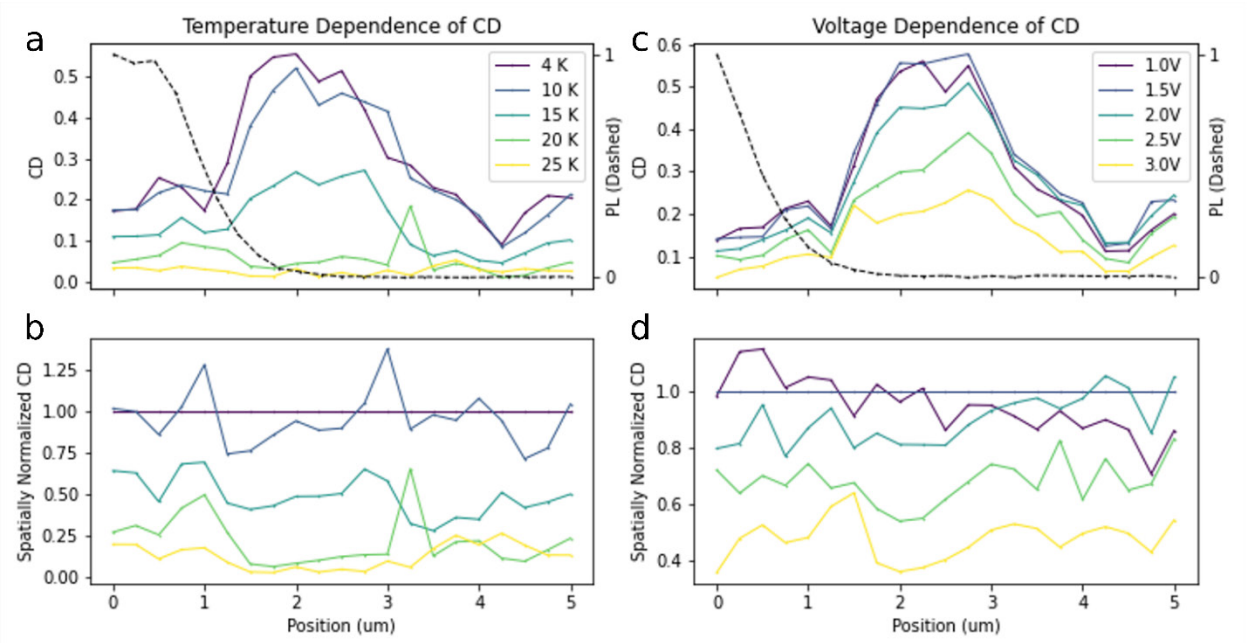

Figure B.10: Temperature and gate dependence of CD spatial profiles. Sample D4: Measured (**a**) and normalized (to 4 K) (**b**) CD spatial profiles observed at various temperatures with a fixed gate voltage of 1.5 V ($n_e \approx 2.8 \times 10^{12}\text{cm}^{-2}$). Measured (**c**) and normalized (to 1.5 V) (**d**) CD spatial profiles observed at various gate biases ($n_e \approx 2 \times 10^{12}\text{cm}^{-2}$ to $4 \times 10^{12}\text{cm}^{-2}$) with a fixed temperature of 4 K. Dashed line indicates the PL intensity, as guidance of pumping spot profile. Note: pump power is 7.8 µW.

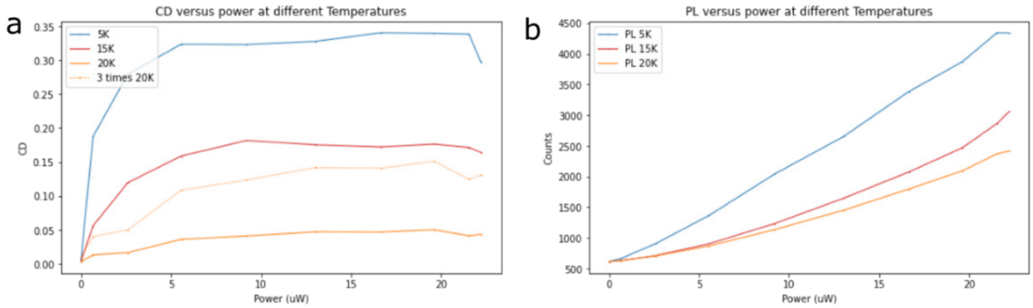

Figure B.11: Power dependence of CD and PL amplitudes under different temperatures. Sample D4: Power-dependent CD with a pump-probe separation of 1.8 µm (**a**) and PL (**b**) amplitudes. Note: Gate voltage is 1.5 V ($n_e \approx 2.8 \times 10^{12}\text{cm}^{-2}$), and pump power is 7.8 µW.

The steady state under CW pumping will have a spin polarization of:

$$\frac{N_+ - N_-}{N_+ + N_-} = \frac{-1}{1 + 2\gamma/G} \tag{B.6}$$

Within this model, the spin polarization should always saturate at a value of 1, as increases in the spin decay rate can always be offset by increasing the pump power – in other words, the saturated spin polarization should be largely temperature independent. To test this prediction, we measure power-dependent CD signal under different temperatures. As depicted in Figure B.11a, the CD signal saturates at similar powers, while the saturated CD amplitude decreases by an order of magnitude. The photoluminescence (PL) power dependence (Fig. B.11b) indicates that the pumping is within the linear absorption regime, meaning the simple rate model should still hold. The saturated CD, then, is solely determined by the temperature. This directly contradicts the predictions of a simple spin pumping model. Such phenomena, on the other hand, is predicted by the temperature curve with a 2D magnetic order as discussed in the main text.

To summarize, a spin diffusion picture predicts dramatically decreasing of spin polarization under pulse pumping away from the pump and the spatial distribution should strongly depend on temperature and doping level. In contrast, our measurements show spin po-

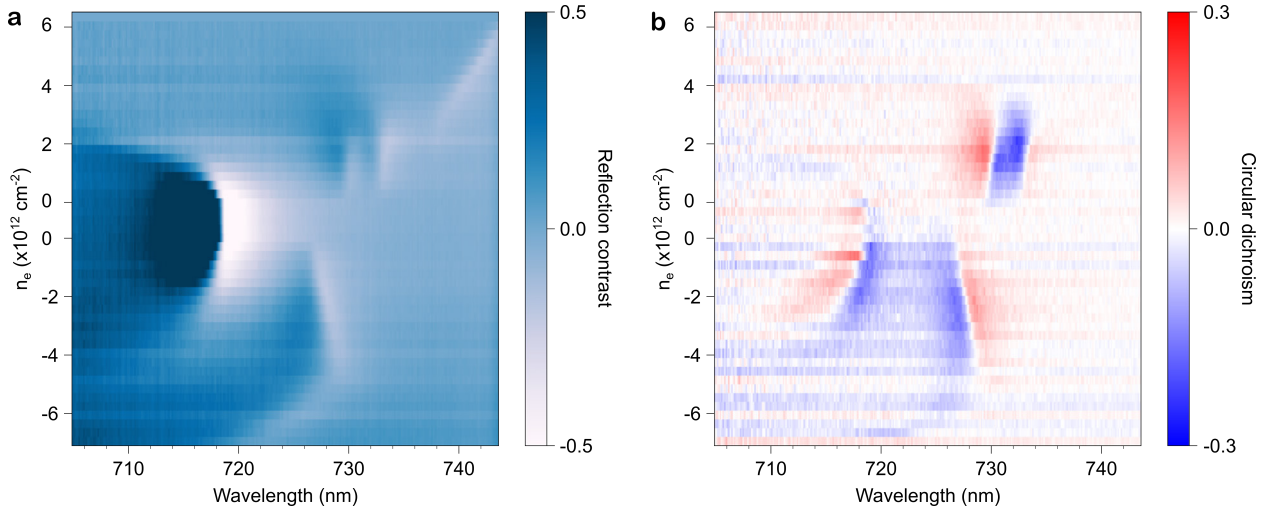

Figure B.12: Sample D5 characterization. Reflection contrast (**a**) and circular dichroism (**b**) signal probed at a distance 2.7 µm from the pump location.

larization significantly larger than the prediction, and with no observable temperature and doping dependence of the spatial profile, only the magnitude of the CD. Also, the power dependent CD amplitude curve under different temperatures significantly deviates from the prediction of the spin pumping/diffusion picture. Given the inadequacy of such a spin pumping/diffusion model to explain the complete dataset, magnetic interactions must account for the observation of long-range spin polarization generated by an optical pump.

B.9 Sample D5 characterization

Figure B.12 shows the reflection contrast and circular dichroism signal at the so-called offset position on sample D5. Time-resolved data are taken within the density region $n = 0.79 \times 10^{12}$ cm^{-2} to $n = 2.73 \times 10^{12}$ cm^{-2} (Fig. 6.7).

B.10 Spin injection estimate

In the simple two-band picture above, the intervalley pumping rate is given by GN_+. This term is an effective pumping rate that captures a variety of underlying dynamic processes.

While the rates of some of these processes can be estimated, others are not well established, making it difficult to compute a precise spin imbalance injected by optical pumping. For example, we can estimate the steady-state number of electrons optically excited in the K valley from the valance band to the upper conduction band $N_+^u = P\alpha\tau/E_{ph} \approx 3\times10^6$ cm^{-2} [280], where $P \approx$ 10 µW µm^{-2} is the power density of the pump laser, $\alpha \approx 1\%$ is the above band-gap absorption, $\tau \lesssim 0.1$ ps is the effective lifetime of the photo-excited electron, and $E_{ph} = 1.96$ eV is the photon energy of the 633 nm pump laser. This population of photo-excited electrons is quite low – many orders of magnitude smaller than the gate-doped carrier density $n_0 \sim 10^{12}$ cm^{-2} – which is due to the short effective lifetime τ of the photo-excited electrons. Several fast processes contribute to τ, such as exciton formation and intervalley spin-conserved scattering. These competing decay channels are estimated to be on the timescale of 10 fs to 1 ps [370]. Considering the intervalley spin-conserved scattering rate $\gamma_v \sim (0.1\text{ ps} - 1\text{ ps})^{-1}$ [47] and the intervalley spin relaxation rate $\gamma_{sv} \sim (0.1\text{ µs} - 1\text{ µs})^{-1}$ [96], we can estimate the optically injected spin imbalance $P_s \approx \frac{N_+^u}{N_0}\frac{\gamma_v}{\gamma_{sv}}$. Without including diffusion, the locally injected spin polarization could range from single percent to full polarization within the area of the pump. However, diffusion will act to decrease the local spin polarization at the pump as the spins transport away. Combined, these factors make it challenging to estimate the injected spin polarization. This dynamic and spatially dependent pump-injected polarization is difficult to directly compare to the case where external magnetic fields constantly and uniformly stabilize the magnetic order [135].